Karlsruhe Institute of Technology

Ultrafast sensing of single-particle dynamics with an optofluidic microcavity

Shalom Palkhivala

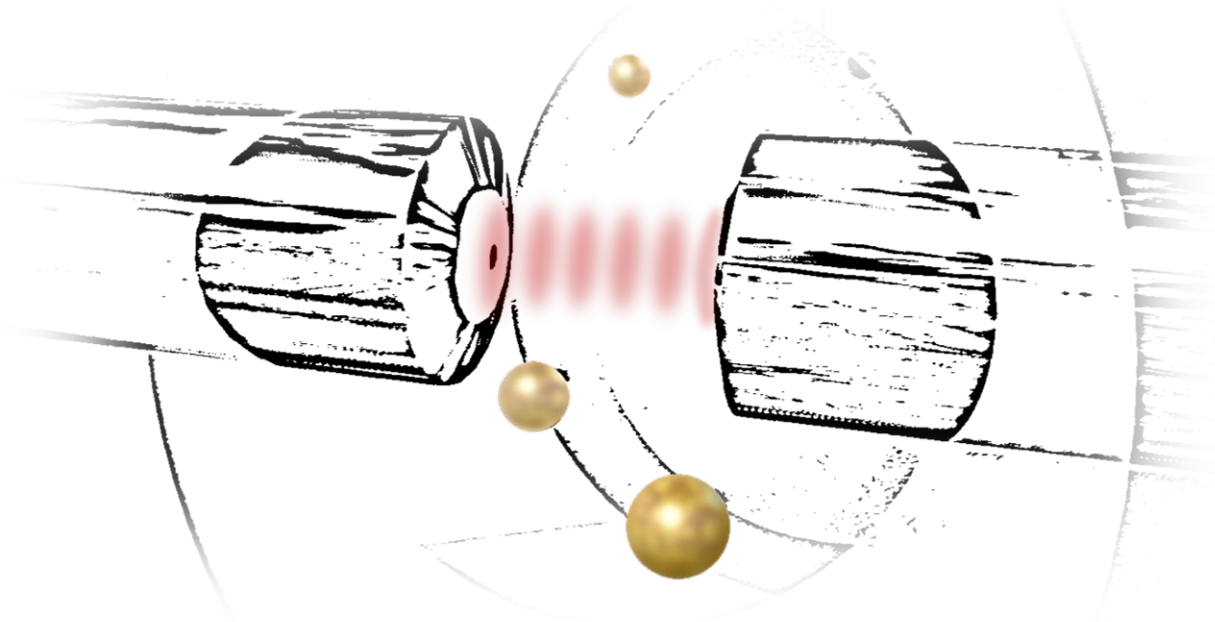

Karlsruhe 2025

Ultrafast sensing of single-particle dynamics with an optofluidic microcavity

Zur Erlangung des akademischen Grades eines

Doktors der Naturwissenschaften (Dr. rer. nat.)

von der KIT-Fakultät für Physik des
Karlsruher Instituts für Technologie

angenommene
Dissertation

von
Shalom Palkhivala, M.Sc.
aus Mumbai (Indien)

Tag der mündlichen Prüfung: 31. Oktober 2025
1. Referent: Prof. Dr. David Hunger
2. Referent: Prof. Dr. Moritz Kreysing

Abstract

Nanoparticles are everywhere, and as they become increasingly relevant in science, medicine and technology, increasingly sophisticated methods are required to investigate them. Since most biochemistry occurs in an aqueous environment, techniques to measure nanoparticles in their natural environment are desired. Many methods for the detection of nanoparticles dispersed in a liquid rely on fluorescently labelling the samples with fluorophores which are not only often costly or toxic, but also may alter the behaviour of the sample itself. As a result, it is of high relevance to study label-free sensing techniques.

A Fabry-Perot microcavity allows the detection of unlabelled particles thanks to the cavity-enhancement of interactions between the optical field and a nanoparticle. In the form presented in this work, the microcavity is integrated into a microfluidic platform, allowing the sample open access to the cavity field. Furthermore, a detection scheme with an actively stabilised cavity is adopted, offering a high sensitivity and high measurement bandwidth. Single gold nanospheres down to 3 nm in diameter could thus be detected. To enable the quantitative analysis of single-particle measurements, an existing theoretical model of diffusion was used to derive an analytical autocorrelation function which allowed the direct determination of the diffusion coefficient and diameter of individual nanospheres, and the results hence obtained were in excellent agreement with measurements using other methods.

The high-bandwidth measurement capability of the stabilised microcavity was then exploited for the measurement of the dynamics of diffusing nanorods, which also exhibit rotational diffusion on the microsecond scale. Simultaneously analysing diffusion and rotation will allow the determination of both the translational and rotational diffusion coefficients, and hence the length and diameter of nanorods. Additionally, a polarisation-split detection scheme was developed to enable the simultaneous measurement of orthogonal polarisation modes in the cavity, allowing the orientation of individual diffusing nanorods to be tracked in two dimensions with a temporal resolution of 20 ns.

The sensitivity of this nanosensor already approaches that of single-molecule sensing techniques, and its relevance to biosensing was demonstrated by sensing ensembles of ~ 10 protein molecules, as well as single DNA nanostructures. This high sensitivity, fast measurement speed and possibility of direct quantitative analysis of particle dynamics make the microcavity a promising technique for the investigation of various nanosystems and biochemical processes on the nanoscale.

Contents

The Blautopf, in Blaubeuren, appears a vibrant shade of blue due to wavelength-dependent Rayleigh scattering at naturally occuring $CaCO_3$ nanoparticles in the water.

1. Introduction

There is not less curiosity in those parts which our single eye cannot reach, than in those which are more obvious.

— Robert Hooke (*Micrographia*, 1665) [1]

Though imperceptibly small, nanoparticles are all around us and play a crucial role in nearly every aspect of our lives: be it in the environment, medicine, semiconductor technology or the biochemistry of life itself, systems at the nanoscale are at work everywhere. Today, they are employed in everyday products from cosmetics (TiO_2 nanoparticles are responsible for effective UV protection in sunscreens) to cars (platinum nanoparticles enhance the efficiency of catalytic converters) [2], and also play a central role in research towards the technologies of tomorrow, for instance in the development of efficient solar cells and quantum processors (single rare-earth ions confined in a nanoparticle show promise as future quantum memories [3]). However, nanotechnology is not new: since the 16th century, gold and silver nanoparticles acting as quantum dots have been used to give stained glass windows their brilliant colours [4], and carbon nanotubes have been discovered in Damascus swords famed for their durability and sharpness [5].

One would be in error to assert that nanoparticles are a human invention, since they are omnipresent in nature as well. Nanoparticulate materials are generated in the atmosphere by volcanic eruptions, erosion, microbial processes, fires and other geographical processes [6]. They exist in metallic, mineral and organic form in the hydrosphere, and their stability and potential toxicity influences underwater ecosystems [7]. But perhaps even more interesting are the biological nanoparticles produced and utilised by life itself. Proteins are nanomaterials (typically 1 nm – 10 nm, but also larger [8]) which occur in billions of varieties, perform a range of functions and are an essential building block of life. Exosomes (30 nm – 150 nm) are nanovesicles present in bodily fluids which induce interactions between cells and can serve as disease markers or tools for immunotherapy or cancer treatment [9–11]. Viruses (typically 20 nm – 200 nm [12]) are also "nanoparticles" of high relevance in global healthcare today, and nanotechnology comes into play in the development of increasingly effective vaccines against them as well [13]. DNA, responsible for encoding genetic information in every organism, naturally forms chromatin fibres (10 nm – 30 nm diameter), and has also entered the field of nanotechnology with "DNA origami", the assembly of DNA nanostructures (~ 100 nm) for applications ranging from drug delivery [14] to nanophotonic devices [15] and plasmonic nanosensors [16, 17].

Clearly, the nanoscopic realm is not only a fascinating subject to study, but also increasingly important as we aim to employ nanoparticles to our advantage and evaluate their effects on us and our environment. In the following section, we shall look at some techniques to gain insights into the world of nanoparticles.

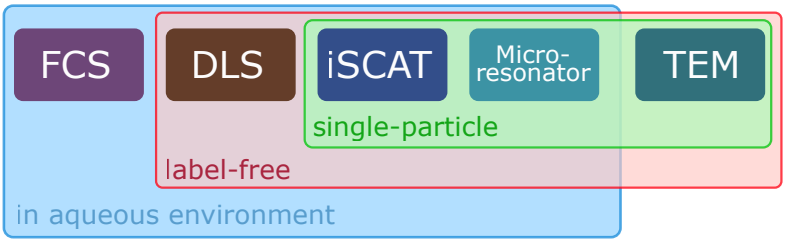

Figure 1.1: An overview of the properties and capabilities of some state-of-the-art techniques for nanoparticle characterisation: transmission electron microscopy (TEM), fluorescence correlation spectroscopy (FCS), dynamic light scattering (DLS), interference scattering microscopy (iSCAT) and microresonators. The microcavity-based sensor presented in this work is suited for the label-free detection of single-particles in an aqueous environment.

1.1. State-of-the-art nanoparticle characterisation

Considering their ubiquity, it is not surprising that nanoparticles and methods to characterise them have been the subject of much research. Due to their small size (< 100 nm), nanoparticles are as such beyond the reach of conventional optical microscopes which, operating with light of wavelength λ, have a resolution on the order of $\lambda/2 \gtrsim 200$ nm. In the 1930s, however, following the publication of Louis de Broglie's theory of matter waves [18], researchers at the (now) Technical University of Berlin exploited the much shorter de Broglie wavelength of electrons to image microscopic specimens using electron beams and magnetic lenses and achieved a higher magnification than was possible with an optical microscope [19]. **Transmission electron microscopy (TEM)** was thus born, and it is now one of the most precise nanoscopy instruments available, capable of sub-nanometre resolution and of providing a clear picture – and hence information about the size and shape – of nanoscaled samples [20]. However, TEM is performed in vacuum, which necessitates elaborate sample preparation and does not offer the possibility to measure nanosystems in their natural environments. Ambiguity could therefore arise when, for example, agglomerates of particles are seen in a TEM image, since it is unknown whether this is their natural state or an artefact of the sample preparation [21]. Given that most biochemistry is water-based, one may now want to find a way to characterise nanoparticles in an aqueous environment.

Sensing in an aqueous environment. The characterisation of nanoparticles suspended in a liquid is possible, for example, by examining their diffusional motion. In **fluorescence correlation spectroscopy (FCS)**, ensembles of fluorophores in suspension diffuse through an observation volume, typically a laser focal spot. Information about their diffusion dynamics can be obtained by analysing their fluorescence signal fluctuations. As we shall see in Section 2.4, the speed of diffusion and hence time scales of these fluctuations are dependent on the particle size. By analysing the correlation of these fluctuations, averaged data about the ensemble, such as the mean particle size and diffusivity, can be quantitatively extracted. Since the theory of FCS will be relevant for this work, it is mentioned in further detail in Section 2.4.2; however, two significant limitations of this method are already apparent: (1) measurement is performed on an ensemble of particles, and details about single particles are lost, and (2) as the name suggests, FCS requires the analyte to fluoresce. Fluorescent labelling of nanoparticles is also common in superresolution microscopy techniques such as those based on **stimulated emission depletion (STED)** microscopy [22, 23]. However, labelling of the sample with fluorophores can be an expensive, complicated process, and the fluorophore also modifies the structure and function

of the sample itself [24]. As a result, we shall now turn towards label-free sensing methods, which enable fast and direct assays of unlabelled particles, such as clinical samples.

Label-free sensing. A well-established method for label-free nanoparticle sizing is **dynamic light scattering (DLS)** [21, 25]. In a similar fashion to FCS, the DLS technique is based on the diffusional motion of particles in an ensemble. When the sample is illuminated by a laser, diffusional motion leads to fluctuations in the light intensity scattered in a particular direction over time. The autocorrelation of the scattered intensity signal is computed, and a size distribution of the sample is determined by evaluating this autocorrelation. While the exact fitting algorithms will not be described here, it should be noted that the choice of algorithm applied (e.g. cumulant analysis or multi-exponential fit) does play a role in the resulting size distribution – intensity-weighted distributions, for example, are highly susceptible being skewed by larger particles (see Appendix A). Nonetheless, DLS remains an efficient way to quickly characterise nanoparticle suspensions in a fluidic environment, and DLS measurements of the samples investigated in this work are discussed in Section 4.3.2.

Results of DLS measurements are still obtained at the cost of averaging over a great number of individual nanoparticles, and at the risk of distortion by a few larger nanoparticles or agglomerates. Therefore, we shall now look at techniques capable of sensing *single* nanoparticles.

Single-particle sensing. The detection of single particles is challenging, since the interactions (scattering, absorption, dispersion) of a nanoparticle with light is extremely small. Although we saw above that even single nanoparticles can be imaged with high resolution using fluorescence microscopes, in this section, we shall concentrate on label-free techniques – which makes the requirements of the detection sensitivity even higher. Optical phenomena which serve to enhance the strength of light-matter interactions must be exploited to achieve the required levels of sensitivity.

One approach to single-nanoparticle detection uses optical interference, by which variations of the phase of an optical wave are measured as a change in intensity. This is used in **interference scattering microscopy (iSCAT)** microscopy, in which the scattering of nanoscopic objects is detected by its interference with a reference beam [26]. The excellent sensitivity of iSCAT has enabled the imaging of single unlabelled biomolecules [27] and more recently the detection of proteins down to 10 kDa using machine learning [28]. Based on the iSCAT system, gold nanoparticles with diameters down to 10 nm have been tracked in three dimensions over several micrometres [29] and sized via their diffusion [30]. Since iSCAT microscopy is an imaging technique, it allows the extraction of rich spatial information of a nanoparticle sample; however, the temporal resolution is then limited by the acquisition speed of the setup, which, even for ultrafast cameras is ~ 100 kHz [29].

Plasmon-based sensors, on the other hand, exploit the enhancement of an optical field by a plasmonic structure, like a metallic nanoparticle, to detect the interaction of an analyte with this so-called optical hotspot. For example, using the hotspot generated by the plasmon resonance of a relatively large sensor gold nanorod, 5 nm nanospheres could be detected with sub-microsecond time resolution [31], and the rotation of diffusing nanorods down to 15 nm in length was measured with a temporal resolution of 50 ns [32]. Additionally, the possibility to detect the influence of low concentrations of polymers in solution on the nanorod diffusivity or plasmonic behaviour suggests applications of plasmonic nanoparticles to label-free biosensing

as well [33]. It should be noted, however, that nanoparticle detection with a plasmon-based sensor is limited to the near-field region of the plasmonic hotspot, and diffusion through the bulk volume is not detected.

Another approach to enhance light-matter interactions is to confine light in an **optical microresonator**, in which constructive interference of light waves sets up a standing-wave field which is extremely sensitive to changes in optical cavity length. The theory of microcavity-based sensing is explained in Section 2.1; however, it is worth looking at some microresonator realisations already. Two leading microresonator geometries for single-particle sensing are whispering-gallery mode resonators and Fabry-Perot resonators.

1. **Whispering-gallery mode resonators.** Explaining the "abnormal loudness with which a whisper is heard" around the dome of St. Paul's cathedral in his book *The Theory of Sound* (1878), Lord Rayleigh (John William Strutt) wrote that "the whisper seems to creep around the gallery horizontally", and thus provided the first description of so-called whispering gallery modes (WGMs) [34]. But the phenomenon of WGMs extends beyond acoustic waves into the realm of microscopic optics as well. In an optical WGM microresonator, light is trapped in an orbit along the surface of the resonator, which could be a microscopic dielectric sphere, ring, disc, or similar circular form, by total internal reflection. When the round-trip path length of this orbit satisfies the condition for resonance, a standing wave is formed along the circumference of the resonator, with an evanescent field extending about 200 nm out of the resonator surface [24, 35]. The introduction of a nanoparticle into this region increases the optical path length of the orbits, spectrally shifting the resonances according to the reactive sensing principle (Section 2.1). The high quality factors of WGM microresonators offer high sensitivity, even to single biomolecules. For instance, the detection of single influenza A viruses (~ 50 nm) with a silica microsphere WGM resonator [36] and quantitative sizing of polystyrene particles with radii down to 30 nm via mode splitting with a microtoroid [37] have been demonstrated over a decade ago.

   Due to the required interaction between the analyte and the evanescent field, WGM-based nanosensors suffer from the same limitation as plasmon-based sensors: the detection volume is very small and limited to the region immediately surrounding the microstructure. Additionally, WGM-based sensing often involves binding of the analyte to the resonator, preventing reuse of the sensor.

2. **Fabry-Perot microcavities.** The idea of optical metrology employing the interference of light between two parallel mirrors has come a long way since the discovery of the Fabry-Perot interferometer by Charles Fabry and Alfred Perot, published in 1901 [38]. Their original device, comprising two partially silvered glass plates, was capable of measuring distances with sub-micrometre precision. While the fundamental idea of the interferometer has remained the same, high-performance devices today have been deployed in experiments ranging from the detection of gravitational waves[1] [39] down to single nanoparticles [40–43].

[1] Each 4-km-long arm of the main Michelson interferometer in LIGO contains a Fabry-Perot resonator which increases the effective arm length by about 300 times, hence enhancing LIGO's sensitivity [39].

Modern Fabry-Perot microcavities typically comprise two planar or concave highly-reflective dielectric mirrors, greatly improving their sensitivity[2] compared to Fabry and Perot's device from 1901. The fibre-based cavity, where at least one cavity mirror is produced directly on the end facet of an optical fibre, allows the formation of ultra-small mode volumes and is a promising architecture for the realisation of a Fabry-Perot microcavity for nanosensing [44]. For example, a "scanning cavity microscope", comprising a mirror-coated fibre scanned over a mirror-coated substrate, was already able to image 40 nm gold nanospheres and 34-nm-long nanorods with a signal enhancement of 1700 times over conventional microscopy [45], and determine the polarisability of individual nanoparticles on the substrate [46].

For underwater nanosensing, Fabry-Perot microcavities can be immersed in the analyte, so that the optical mode field, including the field maximum, is completely accessible to diffusing nanoparticles. In the fibre-fibre design, further described in Chapter 3, both cavity mirrors are fibre-based, and the optical cavity can effectively be integrated into a microfluidic channel for sensing in solution. Furthermore, this design integrates optical in- and out-coupling into the cavity fibres themselves. Such a microcavity has recently been demonstrated in sensing applications and is also implemented in this work. Although the cavity architecture remains similar, researchers have employed different sensing schemes and tricks to achieve different capabilities in their sensors. For example, Larissa Kohler *et al.* pioneered the detection of single nanoparticles with such an optofluidic microcavity via their interaction with the cavity resonance, thereby also laying the foundation for this work. The direct measurement of the position and amplitude of the resonances provided rich quantitative information about the dispersion and extinction of silica nanospheres down to 50 nm in diameter. Additionally, by employing higher-order transverse cavity modes in the cavity, they were able to deduce the spatial position of a nanoparticle, hence enabling its tracking in three dimensions with a measurement bandwidth of up to 14 kHz [41, 47]. More recently, researchers employed the photothermal heating of the liquid in the cavity to enhance dispersive shifts induced by nanoparticles, achieving the capability to sense even single molecules with molecular weights down to 1.2 kDa with a high signal-to-noise ratio (SNR) of over 100. However, the highly non-linear process responsible for this remarkable sensitivity also impedes the extraction of quantitative information about the particles, such as their size. Furthermore, the finite bandwidth of photothermal effects in such a microcavity limits the measurement of nanoparticle dynamics to a narrow velocity window between 5 kHz and 20 kHz [40, 48].

Building on the advantages offered by Fabry-Perot microcavities, such as their tunability, full access of the analyte to their optical modes and flexibility in applications and capabilities, an apparatus to detect single nanoparticles with high sensitivity and measurement bandwidth is developed in this work, along with an analytical technique to directly extract quantitative information about the samples, such as particle size and shape.

[2] We shall see that the cavity developed in this work is sensitive to length changes of under 1 pm, compared to sub-micrometre sensitivity of the 1901 interferometer. This corresponds to an improvement of a million times!

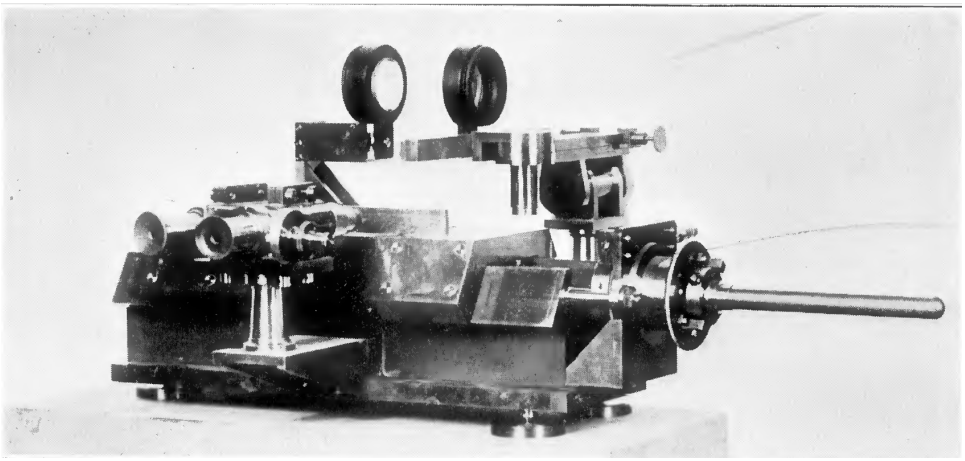

Figure 1.2: The "new form" of interferometer published by Charles Fabry and Alfred Perot in 1901 comprised two partially silvered mirrors and could measure distances with sub-micrometre precision [38].

1.2. Overview of this work

A fibre-based Fabry-Perot microcavity is presented in this work, with which single, unlabelled nanoparticles can be detected and quantitatively characterised. In particular, the sizes of single nanospheres down to 3 nm in diameter have successfully been measured, and the results show excellent agreement with other techniques such as DLS and TEM. To achieve this, a new analytical model to describe the diffusion dynamics of a single nanoparticle in a Fabry-Perot cavity was developed. Additionally, the high measurement bandwidth of the sensor was exploited to investigate the rotational motion of anisotropic nanoparticles, such as gold nanorods, with a detector-limited temporal resolution of down to 20 ns.

In Chapter 2, we shall collect and prepare the tools required to develop a single-particle sensing system. We begin with a review of the **fundamentals of a fibre-based Fabry-Perot microcavity** and then move on to how it reacts to nanoparticles present in its optical mode field. Section 2.4 then describes the theory of **nanoparticle diffusion** and its analysis. We review the autocorrelation function for diffusion in a confocal volume, and then proceed to derive a new model considering **diffusion in a standing wave**. The resulting autocorrelation function was an important result of this work.

Chapter 3 then describes the **setup of the nanoparticle sensor** itself, from the cavity fibres which form the core of the sensor to the optoelectrical control and measurement systems which bring them to life.

A central experimental result of this work is the ability to quantitatively analyse the **size of single particles**, and is presented in Chapter 4. Here, an analysis pathway is developed which addresses the transient nature of single-particle events, and implements the result presented in Chapter 2. This is applied first to simulated data of diffusing nanospheres, and then to real nanoparticle measurements. The results are in excellent agreement with other state-of-the-art measurement techniques.

We then examine the **dynamics of anisotropic particles** in Chapter 5. In addition to translational diffusion, rotational motion opens a window to deduce the shape and dimensions of nonspherical particles such as nanorods. In Section 5.3, a technique for the visualisation of the rotation of nanorods with very high temporal resolution is introduced and the **orientation**

of single particles is tracked. The chapter ends with a brief look at **optical trapping** in five degrees of freedom using a microcavity.

First measurements of **biological samples** are presented in Chapter 6. Here, we look at protein molecules and DNA nanostructures, and use the techniques developed in the previous chapters to estimate their diffusion coefficients. A good agreement with value from theory and the literature demonstrate the suitability of the microcavity for quantitative biosensing, and we shall see that its capability to measure fast dynamics could open up possibilities to detect dynamical processes in addition to diffusion and rotation, such as molecular bending and folding.

Each vibrating string on this acoustic resonator has a fixed length and hence amplifies vibrations at a certain resonance frequency. Its behaviour is therefore very similar to that of an optical cavity – albeit at frequencies 10^9 times smaller.

2. Optical nanosensing in a Fabry-Perot microcavity

Optical nanosensing in a microfluidic environment unites two rather discrete fields of physics: cavity nano-optics and molecular diffusion. In this chapter, we shall outline the theory behind these phenomena, beginning with the Fabry-Perot cavity and continuing with the interactions between the light field and a nanoparticle. We conclude with the diffusive motion of a particle in a fluid, including a model for the analysis of particle dynamics developed in the course of this work.

2.1. Optics of a Fabry-Perot microcavity

In this work, the Fabry-Perot interferometer is implemented as a microresonator with concave fibre-based mirrors, and serves to enhance the interaction between light and matter. The following section briefly outlines the fundamentals of such a resonator.

2.1.1. Resonance in an ideal Fabry-Perot interferometer

Resonators with planar mirrors. An ideal Fabry-Perot resonator comprises two parallel, perfectly reflecting surfaces a distance ℓ apart in the z-direction, which enclose a lossless medium with refractive index n_m between them. A solution for the optical mode between the mirrors is given by the electric field $E(\mathbf{r}) = E_0 \sin(kz)$. When the resonator is excited by light with wavelengths λ_0 and $\lambda_\mathrm{m} = \lambda_0/n_\mathrm{m}$ in vacuum and in the medium respectively, the boundary conditions at the ends of the cavity require that the cavity length and the wavelength be related by

$$\ell = q\frac{\lambda_0}{2n_\mathrm{m}}, \tag{2.1}$$

with $q \in \mathbb{N}$. Equivalently, the optical frequency takes the values $\nu_q = qc_0/(2n_\mathrm{m}\ell)$ at resonance, where c_0 is the vacuum speed of light. The frequency distance between successive resonances is the free spectral range,

$$\mathrm{FSR} = \frac{c_0}{2n_\mathrm{m}\ell}, \tag{2.2}$$

which is an important quantity for the spectroscopic measurement of the cavity length.

Resonators with spherical mirrors. In the form described above, the cavity is marginally stable, and even a minute misalignment between the mirrors will lead to light leaving the cavity and hinder the formation of a stable cavity mode. On the other hand, concave spherical mirrors[1] with radii $R_1, R_2 > 0$ maintain a stable cavity mode as long as the cavity length satisfies the stability condition $0 < g_1 g_2 < 1$, where $g_j = (1 - \ell/R_j)$. This implies a maximum possible cavity length of $\ell_{\max} = R_1 + R_2$; however, an asymmetric cavity (e.g. $R_1 < R_2$) also shows an island of instability for $R_1 < \ell < R_2$. A cavity with spherical mirrors supports a Gaussian mode with electric field

$$E(\mathbf{r}) = E_0 \underbrace{\left(\frac{w_0}{w(z)}\right)}_{\substack{\text{Longitudinal}\\ \text{profile}}} \underbrace{e^{-\frac{x^2+y^2}{w^2(z)}}}_{\substack{\text{Gaussian}\\ \text{profile}}} \underbrace{e^{\frac{ik(x^2+y^2)}{2R(z)}}}_{\substack{\text{Wavefront}\\ \text{curvature}}} \underbrace{e^{-i\xi(z)}}_{\substack{\text{Gouy}\\ \text{phase}}} \underbrace{e^{ikz}}_{\substack{\text{Propa-}\\ \text{-gation}}}, \tag{2.3}$$

where the beam radius at z along the cavity axis varies as $w(z) = w_0\sqrt{(1 + (z/z_0)^2)}$, the wavefront curvature is $R(z) = z[1 + (z_0/z)^2]$, and the Gouy phase is $\xi(z) = \tan^{-1}(z/z_0)$, which arises due to curved wavefronts losing phase compared to their planar counterparts. The beam waist w_0 and Rayleigh length z_0 are related by $z_0 = (\pi w_0^2)/\lambda$. Further details about the Gaussian beam can be found extensively in the literature [49, 50].

Let the positions of the two mirrors be z_1 and $z_2 = z_1 + \ell$. Then, the resonance condition is

$$\nu_q = \left(q + \frac{\Delta\xi}{\pi}\right)\frac{c_0}{2n_{\mathrm{m}}\ell}, \tag{2.4}$$

where $\Delta\xi = \xi(z_2) - \xi(z_1) = \cos^{-1}(\sqrt{g_1 g_2})$ [51], and the FSR remains unchanged. Finally, the beam waist, w_0, of the Gaussian mode can be calculated using [52]

$$w_0^2 = \left(\frac{\lambda_{\mathrm{m}}\ell}{\pi}\right)\sqrt{\frac{g_1 g_2(1 - g_1 g_2)}{g_1 + g_2 - 2g_1 g_2}}. \tag{2.5}$$

Higher-order transverse modes. In additional to the "fundamental" Gaussian mode, a family of Hermite-Gauss modes exists with different spatial field distributions from the fundamental. The Hermite-Gauss mode defined by indices (l, m) has the electric field

$$E_{lm}(\mathbf{r}) = E_0\left(\frac{w_0}{w(z)}\right)e^{-\frac{(x^2+y^2)}{w^2(z)}}\underbrace{\mathbb{H}_l\left(\frac{\sqrt{2}x}{w(z)}\right)\mathbb{H}_m\left(\frac{\sqrt{2}y}{w(z)}\right)}_{\substack{\text{Hermite-Gauss}\\ \text{transverse profile}}}e^{ik\frac{(x^2+y^2)}{R(z)}}e^{-i(1+l+m)\xi(z)}e^{ikz}, \tag{2.6}$$

where $\mathbb{H}_l(x)$ is the Hermite polynomial of order l.

[1] Only concave mirrors are used in this work, and the convention $R > 0$ is chosen for convenience.

Hence, the (l, m) mode is resonant at

$$\nu_{qlm} = q\frac{c_0}{2n_{\mathrm{m}}\ell} + (1 + l + m)\frac{\Delta\xi}{\pi}\frac{c_0}{2n_{\mathrm{m}}\ell} \tag{2.7}$$

and the separation between adjacent transverse modes of the same mode family q can be written as

$$\Delta\nu_{\mathrm{transverse}} = \frac{c_0}{2n_{\mathrm{m}}\ell}\frac{\Delta\xi}{\pi}. \tag{2.8}$$

Analogously to Equation 2.2, this enables the spectroscopic length measurement of a cavity via the transverse mode separation.

While the transverse modes also have applications such as the spatial tracking of nanoparticle diffusion [41] or the rotation of a trapped microscopic specimen [53], they typically dominate in misaligned cavities, so that in the scope of this work, we attempt to minimise them and channel the optical energy into the fundamental mode instead.

2.1.2. Losses in a Fabry-Perot resonator

In contrast to the optical output of a Michelson interferometer, which results from the interference of two beams, the output of a Fabry-Perot interferometer is the result of the interference of a very large number of waves circulating within the resonator, enhancing the sensitivity of the interferometer to small changes in the optical length. The degree of cavity-enhancement depends on the amount of optical loss from the cavity, and hence on the number of trips made by a beamlet within the cavity before it is lost.

Sources of optical losses. Losses arise from absorption and scattering at the mirrors and in the medium, imperfect mode matching between the input, output and cavity modes, and clipping at the mirrors.

1. **Losses at the mirrors.** The reflectivity of real mirrors is $\mathcal{R} < 1$, and a fraction $\mathcal{L}_{\mathrm{mirror}} = 1 - \mathcal{R} > 0$ is lost from the cavity on each reflection. This consists of transmission through the mirror ($\mathcal{T}$) and scattering and absorption at the mirror ($\mathcal{S}$): $\mathcal{L}_{\mathrm{mirror}} = \mathcal{T} + \mathcal{S}$.
2. **Intracavity loss.** An absorbing medium in the cavity attenuates the light travelling through the cavity according to the Beer-Lambert law, so that the round-trip loss due to the medium is $\mathcal{A} = 1 - \exp(-2\alpha\ell)$, where α is the absorption coefficient of the medium.

The losses discussed so far are due to the material properties of the cavity and lead to a round-trip loss of $\mathcal{L}_{\mathrm{mat}} = 2\mathcal{T} + 2\mathcal{S} + \mathcal{A}$, where we assume an identical coating on both mirrors.

3. **Mode matching.** The coupling efficiency between the mode exiting the input fibre and the cavity mode is given by the mode power coupling efficiency [44, 54]

$$\varepsilon = \frac{4}{\left(\frac{w_{\mathrm{f}}}{w_{\mathrm{m}}} + \frac{w_{\mathrm{m}}}{w_{\mathrm{f}}}\right)^2 + \left(\frac{\pi n_{\mathrm{f}} w_{\mathrm{f}} w_{\mathrm{m}}}{\lambda R}\right)^2}, \tag{2.9}$$

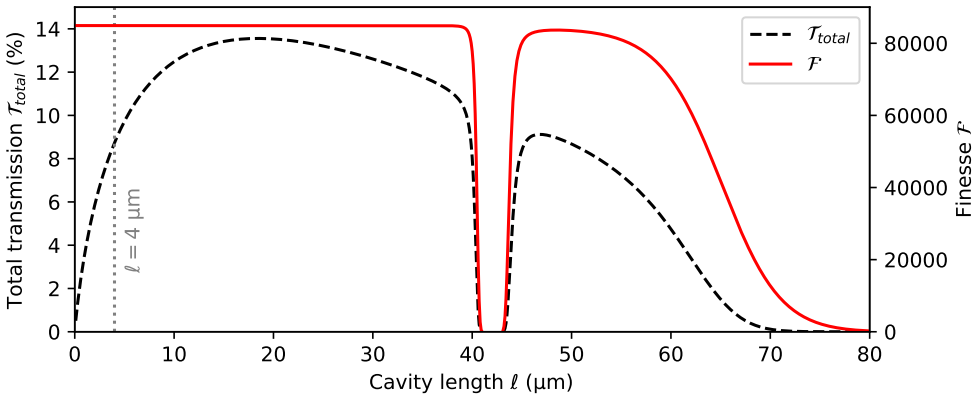

Figure 2.1: Theoretical cavity transmission and finesse considering the losses described in Section 2.1.2. The mirror parameters are taken from Section 3.1.1, the cavity medium is air and misalignments are neglected, giving an expected transmission of 9% and finesse of 85000 for a 4 μm cavity.

with the radii of the fibre mode and the cavity mode at the fibre face given by w_f and w_m respectively, and the refractive index of the fibre by n_f. The first term in the denominator accounts for the beam radius mismatch and is optimal when $w_\mathrm{f} = w_\mathrm{m}$, while the second (less dominant) term arises due to the wavefront curvature and keeps $\varepsilon < 1$ for concave cavity mirrors, even when the beam radii match perfectly. Note that additional mode coupling losses are induced by imperfect alignment or tilt of the cavity fibres [54].

4. **Clipping loss.** The loss due to the cavity mode extending farther than the extent of the cavity mirrors (radius R_m) is given by $\mathcal{L}_\mathrm{clip} = \exp(-2R_\mathrm{m}^2/w_\mathrm{m}^2)$ [44]. For the configurations used in this work, this source of loss is negligible and is included here for completeness.

These losses are geometry-dependent and can be minimised by a suitable choice of the cavity parameters (weak mirror curvature and short cavity length), which, however, may conflict with the requirements for a specific cavity application (e.g. strongly curved mirrors for a small mode volume).

5. **Outcoupling efficiency.** Finally, this represents the probability that light in the cavity leaves the cavity via a particular mirror (transmission $\mathcal{T}$), and is given by $\eta = \mathcal{T}/\mathcal{L}$ with total loss $\mathcal{L}$. While identical mirror coatings were used in this work, η can be optimised for collecting light emitted from within the cavity by using asymmetrical coatings [55].

The cavity linewidth. In the presence of loss, the magnitude of a beamlet circulating in the cavity diminishes with time. If a fraction $\mathcal{L}$ of optical power is lost from the cavity per round trip, it can be shown [49, 56] that the resonances of a real cavity are described by the Airy function

$$I = \frac{I_\mathrm{max}}{1 + \left(\frac{2\mathcal{F}}{\pi}\right)^2 \sin^2\left(\frac{2\pi\nu n_\mathrm{m}\ell}{c_0}\right)} \tag{2.10}$$

and approximated as a Lorentzian line

$$I = \frac{I_{\max}}{1 + 4\mathcal{F}^2 \left(\frac{2n_{\mathrm{m}}\ell\nu}{c_0} - q\right)^2}, \tag{2.11}$$

where $I_{\max} = I_0/(1-(1-\mathcal{L})^{1/2})^2$, and the finesse of the resonator,

$$\mathcal{F} = \frac{\pi(1-\mathcal{L})^{1/4}}{1-(1-\mathcal{L})^{1/2}}, \tag{2.12}$$

is an important figure of merit quantifying the sharpness and visibility of cavity resonances. When the overall losses are small ($\mathcal{L} \ll 1$), the finesse is large ($\mathcal{F} \gg 1$), and it relates the cavity linewidth full-width at half maximum (FWHM) to the FSR by

$$\mathcal{F} = \frac{\mathrm{FSR}}{\mathrm{FWHM}}. \tag{2.13}$$

In this regime, Equation 2.12 takes the form $\mathcal{F} = 2\pi/\mathcal{L}$, $I_{\max} = 4I_0/\mathcal{L}^2$ and the peak cavity transmission is given by $T_{\max} = 4\mathcal{T}^2/\mathcal{L}^2$, assuming both mirrors have transmittivity $\mathcal{T}$. The cavity linewidth is proportional to the total losses, $\mathrm{FWHM} = c_0\mathcal{L}/(4\pi n_{\mathrm{m}}\ell)$, and the resonator lifetime $\tau_{\mathrm{res}} = 1/(2\pi\cdot\mathrm{FWHM}) = n_{\mathrm{m}}\ell\mathcal{F}/(\pi c_0)$ sets a fundamental limit on the temporal resolution of measurements with the cavity.

Power in the cavity. The peak power circulating in the cavity in the steady state is given by

$$P_{\mathrm{cav}} = 4\mathcal{T}\left(\frac{\mathcal{F}}{\pi}\right)^2 P_{\mathrm{in}} \tag{2.14}$$

and can also be determined from the transmitted power, $P_{\mathrm{out}} = \mathcal{T}P_{\mathrm{cav}}/4$ [50]. The time-averaged optical power at an antinode is $\langle P_{\mathrm{cav}}\rangle = P_{\mathrm{cav}}/2$ [57].

2.1.3. Polarisation modes in the cavity

According to Equation 2.4, the resonance frequency of a Gaussian cavity mode is dependent on the effective radii of curvature of the cavity mirrors. When the mirrors are elliptical or tilted, the radius of curvature is not isotropic; instead, different polarisations of light in the cavity see different effective radii of curvature. If mirror j has long and short radii of curvature R_{jx} and R_{jy} respectively, measured in the local basis of the mirror, the asymmetry of the mirror is defined as $\delta_j = |R_{jx}^{-1} - R_{jy}^{-1}|$ and the "geometrical birefringence" of the cavity is $\Delta(\theta) = \sqrt{\delta_1^2 + \delta_2^2 + 2\delta_1\delta_2\cos(2\theta)}$, where θ is the angle between the long axes of the two mirrors [58].

The orientation of the polarisation modes, i.e. the cavity polarisation eigenbasis axes, with respect to the long axis of mirror 1 is given by [58]

$$\Psi(\theta) = \tan^{-1}\left(\frac{1}{\sin(2\theta)}\left(\sqrt{1+\left(\frac{\delta_1}{\delta_2}\right)^2+2\left(\frac{\delta_1}{\delta_2}\right)\cos(2\theta)}-\frac{\delta_1}{\delta_2}-\cos(2\theta)\right)\right). \tag{2.15}$$

The cavity polarisation eigenbasis more strongly aligns itself to the basis of the mirror with larger δ_j.

The dependence of the resonance frequency on radius of curvature means that components of the optical field polarised along the long and short axes of the cavity polarisation eigenbasis described above are resonant at different frequencies, and hence at different cavity lengths for excitation at a fixed wavelength. In other words, orthogonal polarisation modes are spectrally non-degenerate.

The frequency splitting between the polarisation modes due to this effect is

$$\Delta\nu_{\text{pol}} = \frac{c_0\lambda}{8\pi^2 n_{\text{m}}^2 \ell}\Delta(\theta). \tag{2.16}$$

The polarisation splitting is minimum when the long axes of the mirrors are mutually perpendicular, and maximum when they are parallel. Note, however, that this splitting will be further increased by material birefringence of the mirrors and tilt or misalignment between the mirrors.

In fact, the beam waist is also dependent on the curvature of the cavity mirrors, and this can lead to the formation of an elliptical cavity mode. For the simple case of identical mirrors, $w_{0x}/w_{0y} = \left((2R_x-\ell)/(2R_y-\ell)\right)^{1/4}$. However, as long as the cavity length does not approach the mirror radius of curvature, this ratio varies slowly and stays close to unity.

2.2. The cavity mirrors

Distributed Bragg reflectors. Traditional metal mirrors do not meet the performance requirements for the high-finesse cavities used in this work[2]. Instead, we employ high-reflectivity distributed Bragg reflectors (DBRs), which comprise alternating layers of dielectric materials having high and low refractive indices (n_{H} and n_{L} respectively). It can easily be shown [59] that the condition for high reflectance at this layer stack is that each layer is a quarter optical wavelength[3] thick, $n_{\text{H}}d_{\text{H}} = n_{\text{L}}d_{\text{L}} = \lambda_0/4$. The maximum reflectivity of a quarter-wave stack with N layer pairs can be approximated as

$$\mathcal{R} = \left(\frac{1-(n_{\text{f}}/n_{\text{m}})(n_{\text{H}}/n_{\text{L}})^{2N}}{1+(n_{\text{f}}/n_{\text{m}})(n_{\text{H}}/n_{\text{L}})^{2N}}\right)^2 \tag{2.17}$$

at its designed wavelength λ_0, where n_{f} and n_{m} are the refractive indices of the substrate (fibre) and surrounding medium respectively [60]. The wavelength-dependence of the layer

[2] Mirrors with 99.9% reflectivity would enable a finesse of only 625, even neglecting losses!

[3] In order to fine-tune the reflectivity, the thickness of some layers are slightly changed from an optical quarter wavelength.

thickness means that $\mathcal{R}$ falls off away from the designed wavelength. The spectral width of the high-reflectivity stopband is determined by the index contrast between the two layers, and the stopband lies in the wavelength range [60]

$$\lambda \in \left(\frac{\lambda_0}{1 + \frac{2}{\pi} \sin^{-1}\left(\frac{n_\mathrm{H}-n_\mathrm{L}}{n_\mathrm{H}+n_\mathrm{L}}\right)}, \frac{\lambda_0}{1 - \frac{2}{\pi} \sin^{-1}\left(\frac{n_\mathrm{H}-n_\mathrm{L}}{n_\mathrm{H}+n_\mathrm{L}}\right)} \right). \tag{2.18}$$

A further consideration is the phase of the optical wave at the mirror surface, which can be determined by ending the layer stack with a high or low refractive index layer. This choice also influences the penetration depth into the mirror.

Penetration depth. DBRs get their name from the fact that, in contrast to a perfect "optically hard" mirror, the optical field reflected at a DBR extends some distance δ into the dielectric stack. Whereas the associated distance is often loosely called the "penetration depth", the precise definition of this depth is dependent on an associated optical quantity. The following summary aims to remove some of the ambiguity surrounding the penetration depth and derives largely from the treatment by Corné Koks and Martin van Exter [61, 62].

1. **Intensity penetration depth** (δ_I). This is the distance into the DBR at which the optical intensity has decayed to its 1/e level. It is given by[4]

$$\delta_I = \frac{\lambda_0}{8} \frac{n_H^{-1} + n_L^{-1}}{\ln(n_H/n_L)} \approx \frac{\lambda_0}{4(n_H - n_L)} \tag{2.19}$$

   for relatively small index contrast and at the centre of the stopband of the DBR.

2. **Phase penetration depth** (δ_ϕ). DBRs ending with a high-refractive-index layer are designed to produce a phase shift of π on reflection at the designed wavelength λ_0, i.e. a node forms at the mirror surface. Light which is detuned from λ_0 forms a node at a distance δ_ϕ from the surface, which determines the effective resonance condition of the cavity. In this work, the cavity is operated close enough to the designed wavelength that δ_ϕ may be neglected.

3. **Frequency penetration depth** (δ_τ). The depth $\delta_\tau = c_0\tau/2n_\mathrm{m}$ is associated with the group delay τ experienced by light reflected at the mirror. This depth describes the frequency properties of the cavity and should be used for the determination of cavity length via the FSR. For a DBR ending with a high-refractive-index layer, the group delay suffered by light inside the mirror is

$$\tau = \frac{n_\mathrm{m}}{n_H - n_L} \frac{\lambda_0}{2c_0} \tag{2.20}$$

   and the frequency penetration depth in this case is identical to Equation 2.19.

[4] Koks and van Exter miss the division by $\ln(n_H/n_L)$ in their Equation 2 [61].

4. **Modal penetration depth** (δ_D). Finally, this quantity describes the imaging properties of the mirrors, i.e. the angular dependence of light reflected at the mirror. The position of the equivalent optically hard mirror is at $\delta_D = \beta\delta_\tau$, where $\beta = n_\mathrm{m}^2(n_\mathrm{L}^{-2} + n_\mathrm{H}^{-2})/2$. According to Koks and van Exter, this penetration depth defines the frequency position of higher order transverse modes and should be taken into account when using Equations 2.7 and 2.8.

Therefore, we must take the total optical cavity length ($n_\mathrm{m}\ell + 2\delta$) into account when performing spectroscopic measurements. Equations 2.2 and 2.8 become

$$\mathrm{FSR} = \frac{c_0}{2\,(n_\mathrm{m}\ell + 2\delta_\tau)} \tag{2.21}$$

and

$$\Delta\nu_\mathrm{transverse} = \frac{c_0}{2\,(n_\mathrm{m}\ell + 2\delta_D)}\frac{\Delta\xi}{\pi}. \tag{2.22}$$

2.3. Interactions between light and nanoparticles

We would now like to add functionality to the empty cavity discussed so far: in the context of building a nanosensor, this involves adding nanoparticles to the cavity. In the following, we shall look at the microcavity's optical response to a nanoparticle in the optical field, and then examine the motion of freely diffusing nanoparticles, which finally leads us to a means to measure particles via their diffusion dynamics in Section 2.4.2.

2.3.1. Optical properties of nanoparticles

Most of this work was done using gold nanoparticles of varying shapes and sizes, since they can be accurately manufactured and hence provide known samples for the development and characterisation of the nanosensor described herein. In this section, we shall briefly look at the optical properties and peculiarities of these particles, before examining their effect on a resonant optical field in the next section.

Dielectric function of metal nanoparticles. The complex electric permittivity $\varepsilon(\omega) = \varepsilon_1(\omega) + i\varepsilon_2(\omega)$ and hence the complex refractive index $\tilde{n}(\omega) = n(\omega) + i\kappa(\omega)$ of a metal such as gold is described using the Drude-Lorentz model,

$$\varepsilon(\omega) = \underbrace{1 - \frac{\omega_\mathrm{P}^2}{\omega^2 + i\gamma\omega}}_{\text{free electron}} + \underbrace{\sum_j \frac{f_j\omega_\mathrm{P}^2}{\omega_j^2 - \omega^2 - i\omega\Gamma_j}}_{\text{bound electron}}, \tag{2.23}$$

where the first part (the Drude model for ideal metals) arises from free electron effects, and the second (Lorentz model for dielectrics) from bound electron effects. Here, ω_P is the plasma frequency of the metal and γ the associated bulk damping constant, and the summation runs

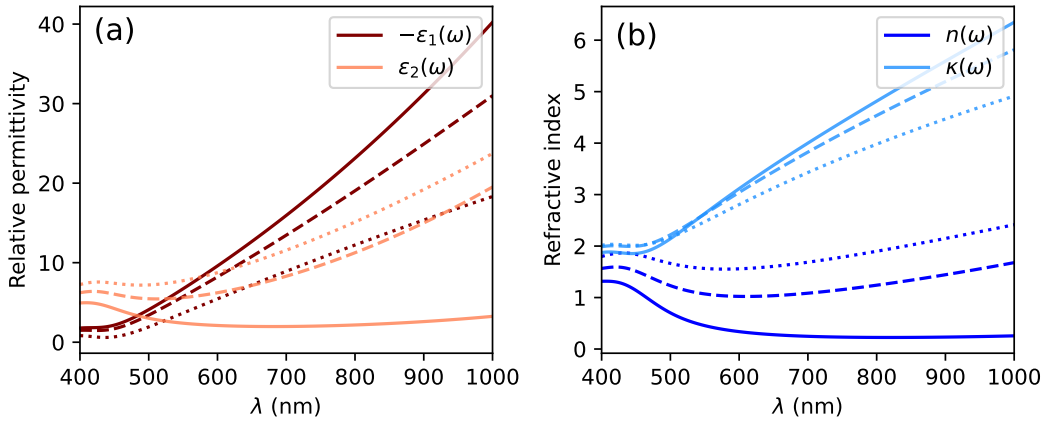

Figure 2.2: (a) Real (ε_1) and imaginary (ε_2) parts of the dielectric function, and (b) the real (n) and imaginary (κ) parts of the refractive index of gold. The solid lines represent the bulk material, and the dashed and dotted lines show size corrections for spherical nanoparticles with radii $R_{\mathrm{NP}} = 10$ nm and 5 nm respectively. Material parameters are taken from Rakić *et al.* [63] and Granqvist and Hunderi [64].

over oscillators with resonant frequencies ω_j, strengths f_j and damping constants Γ_j. This model has been parametrised, e.g. by Rakić *et al.* [63], and is shown in Figure 2.2.

When the particle size approaches the mean free path of conduction electrons in the metal (roughly 30 nm in gold), **intrinsic size corrections** must be included in the Drude model of the dielectric function itself [65]. In this case, the damping constant for confined electrons in a nanoparticle with radius R_{NP} becomes $\gamma(R_{\mathrm{NP}}) = \gamma + g v_{\mathrm{F}}/R_{\mathrm{NP}}$ where v_{F} is the Fermi velocity [64] and the factor $g \sim 1$ [66].

The size-dependent dielectric function then becomes

$$\varepsilon(\omega, R_{\mathrm{NP}}) = 1 - \frac{\omega_{\mathrm{P}}^2}{\omega^2 + i\gamma(R_{\mathrm{NP}})\omega} + \sum_j \frac{f_j \omega_{\mathrm{P}}^2}{\omega_j^2 - \omega^2 - i\omega\Gamma_j}, \tag{2.24}$$

and is compared to its bulk counterpart in Figure 2.2.

Optical response of nanoparticles. The study of the scattering of light by small particles dates back to 1869, when John Tyndall, while attempting to explain the colour and polarisation of skylight, performed light scattering experiments on a vapour of particles "probably far beyond the reach of our highest microscopic powers" [67]. This drew the interest of Lord Rayleigh, who, in a series of publications between 1871 and 1881, also studied the theory of light scattering in the sky [68] and developed a general electromagnetic theory describing the scattering of light on small particles [69].

In the framework of Rayleigh's theory, particles are considered which are small compared to the wavelength of light, so that the electric field is nearly constant over the extent of the particle's volume. If a spherical particle is suspended in a medium with relative permittivity ε_{m}, the optical response of the particle is described by its (in general complex) excess polarisability α, given by the Clausius-Mossotti equation,

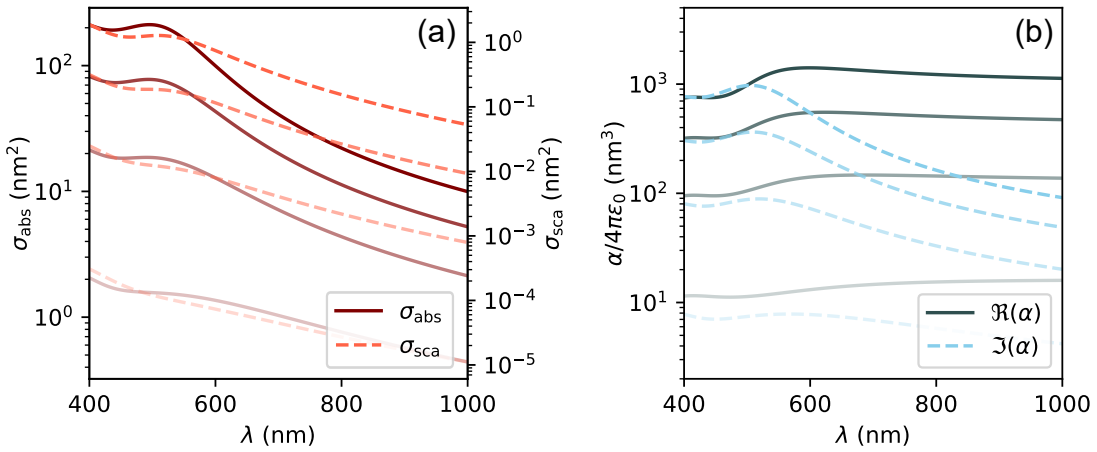

Figure 2.3: (a) The absorption and scattering cross sections of gold nanospheres with diameters 5 nm, 10 nm, 15 nm and 20 nm shown in increasing darkness, as a function of optical wavelength. (b) The real (solid curves) and imaginary (dashed) parts of the polarisability of gold nanospheres with the same sizes as in (a).

$$\alpha(\omega) = 4\pi\varepsilon_0 R_{\mathrm{NP}}^3 \frac{\varepsilon(\omega) - \varepsilon_{\mathrm{m}}}{\varepsilon(\omega) + 2\varepsilon_{\mathrm{m}}}, \tag{2.25}$$

where $\varepsilon_{\mathrm{m}} = n_{\mathrm{m}}^2$ is the relative permittivity of the surrounding medium, and the possible size-dependence of $\varepsilon(\omega)$ is not explicitly shown. The Fröhlich condition for the plasmon resonance of the particle, $\Re\{\varepsilon(\omega)\} = -2\varepsilon_{\mathrm{m}}$, follows directly from this, and corresponds to plasmon resonance wavelengths around 500 nm for the nanospheres used in this work.

The loss of optical energy due to interaction with a nanoparticle is given by the extinction cross-section $\sigma_{\mathrm{ext}} = \sigma_{\mathrm{abs}} + \sigma_{\mathrm{sca}}$ with the absorption (σ_{abs}) and scattering (σ_{sca}) cross-sections [42, 70–72][5]

$$\sigma_{\mathrm{abs}} = \frac{2\pi n_{\mathrm{m}}}{\varepsilon_0 \lambda_0} \Im\{\alpha\} \quad \text{and} \quad \sigma_{\mathrm{sca}} = \frac{8 n_{\mathrm{m}}^4}{3\varepsilon_0^2 \lambda_0^4} |\alpha|^2 . \tag{2.26}$$

When the particle size is *comparable* to the wavelength, the electric field over the particle is not uniform, and multipolar plasmon oscillations occur [73]. The scattering and absorption of such particles are described by the scattering theory of Gustav Mie. In his paper published in 1908, Mie discussed the colour of metal colloids with various particle sizes, and developed solutions to Maxwell's equations for scattering by a sphere of arbitrary size [74]. Mie's theory remains an essential tool for the investigation of light scattering in various fields of science today[6]; however, the Rayleigh approximation suffices to describe optical interactions with the nanoparticles used in this work.

For **anisotropic particles** such as nanorods, the polarisability is also direction-dependent and, in the Rayleigh regime, it is given by

[5] The reader should exercise caution when comparing expressions from different sources, since conventions for normalising α often differ among authors (e.g. by $4\pi\varepsilon_0$ [72] or ε_0 [43, 70, 71]).

[6] As of 2025, Mie's original paper has been cited almost 10,000 times!

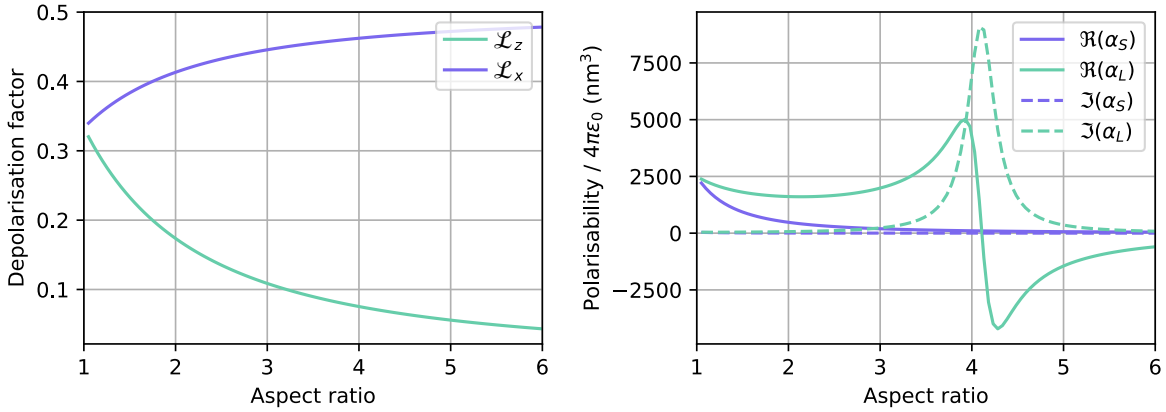

Figure 2.4: (a) Geometric depolarisability factors for the long ($\mathscr{L}_z$) and short ($\mathscr{L}_x$) nanorod axes with varying aspect ratios (p). In the limit of a sphere, $p = 1$ and $\mathscr{L}_x = \mathscr{L}_y = \mathscr{L}_z = 1/3$. In the limit of a very long rod ($p \to \infty$), $\mathscr{L}_z \to 0$ and $\mathscr{L}_{x,y} \to 1/2$. (b) Components of the polarisability of a gold nanorod with $L = 25$ nm along the long (α_L) and short (α_S) nanorod axes with varying aspect ratio and $\lambda_0 = 780$ nm.

$$\alpha_i(\omega) = \varepsilon_0 V_{\mathrm{NP}} \frac{\varepsilon(\omega) - \varepsilon_{\mathrm{m}}}{\varepsilon_{\mathrm{m}} + \mathscr{L}_i \left[\varepsilon(\omega) - \varepsilon_{\mathrm{m}}\right]} \tag{2.27}$$

along the i^{th} axis ($i \in \{x, y, z\}$) of the nanoparticle, where V_{NP} is the nanoparticle volume and $\mathscr{L}_i$ are called the depolarisation factors, which satisfy $\sum_i \mathscr{L}_i = 1$. For the symmetric case of a sphere, $\mathscr{L}_i = 1/3$ along all directions and Equation 2.27 reduces to Equation 2.25. For a rod-like particle with length $L = 2b$ along the z-axis and diameter $d = 2a$, we have [47, 70]

$$\mathscr{L}_z = \frac{a^2}{b^2 - a^2}\left[\frac{b}{2\sqrt{b^2 - a^2}} \ln\left(\frac{b + \sqrt{b^2 - a^2}}{b - \sqrt{b^2 - a^2}}\right)\right] \tag{2.28}$$

and $\mathscr{L}_x = \mathscr{L}_y = (1 - \mathscr{L}_z)/2$.

In metallic nanorods, Equation 2.27 tells us that the plasmon resonances corresponding to the i^{th} nanoparticle axis occur when $\Re\{\varepsilon(\omega)\} = -\varepsilon_{\mathrm{m}}(1 - \mathscr{L}_i)/\mathscr{L}_i$, and the resonance wavelengths are highly sensitive to size and aspect ratio of the particle. At the wavelength $\lambda_0 = 780$ nm used in this work, a plasmon resonance occurs for small nanorods with aspect ratio around 4. At larger sizes (> 50 nm), actual length and diameter begin to play a larger role [75].

2.3.2. Nanoparticles in a resonator

The primary motivation to use an optical resonator as a sensing device lies in the cavity-enhancement of interactions between light and a nanoscopic sample. When a polarisable particle with excess polarisability α interacts with the optical mode of a cavity, two main effects are observed: a **dispersive shift** of the cavity resonance and optical loss from the cavity due to **extinction by the particle**. It should be noted that when an *anisotropic* particle like a nanorod, which has a direction-dependent polarisability as described in Section 2.3.1, enters a linearly polarised optical field, one must consider the component of the polarisability along the polarisation direction. This will be particularly relevant in Chapter 5.

Resonance shift. When a particle enters the optical field of the cavity, it produces a resonance shift of [47]

$$\Delta\nu = -\Re(\alpha)\frac{c_0}{2\lambda_0\varepsilon_0 V_\mathrm{m}}\left|\frac{E(\mathbf{r_0})}{E_\mathrm{max}}\right|^2, \tag{2.29}$$

where $E(\mathbf{r_0})$ is the electric field at the position $\mathbf{r_0}$ of the nanoparticle, E_max is the maximum electric field strength in the cavity mode and V_m is the cavity mode volume. This is the **reactive sensing principle** and forms the basis for much work in the field of cavity-enhanced nanoparticle sensing. Note that from Equation 2.29, decreasing the mode volume increases the size of the resonance shift produced by a given nanoparticle.

Nanoparticle-induced losses. In Section 2.3.1, we introduced the optical extinction caused by a nanoparticle as the extinction cross-section. This describes the size of an imaginary disc which would extinguish light impinging on its surface. For a nanoparticle in a cavity, the extinction cross-section leads to an expression for the maximum loss produced by the particle,

$$\mathcal{L}_\mathrm{NP} = \frac{4\sigma_\mathrm{ext}}{\pi w_0^2}, \tag{2.30}$$

which essentially compares the extinction cross-section to the cross section of the cavity mode [42]. To determine the effect of the particle on the resonance amplitude, $\mathcal{L}_\mathrm{NP}$ is added to the total (particle-free) cavity loss $\mathcal{L}$ in Equation 2.12, so that the new finesse is reduced to $\mathcal{F}_\mathrm{NP} = 2\pi/(\mathcal{L} + \mathcal{L}_\mathrm{NP})$. As a result, a **decrease in transmitted power** follows from Equation 2.14. Via Equation 2.13, the reduction in finesse also leads to **broadening** of the resonance line.

2.4. Particle diffusion in a fluid

The reactive sensing principle (Equation 2.29) tells us that the magnitude of the interaction of the cavity mode with a nanoparticle depends on the location $\mathbf{r_0}$ of the particle. Reactive sensing therefore provides us with a tool to study the motion, for example diffusion, of a nanoparticle in the cavity.

2.4.1. A theoretical description of diffusion

While investigating the microscopic structure of pollen grains from *Clarkia pulchella* flowers in 1828, botanist Robert Brown was struck by the random, "rapid oscillatory" motion of the pollen when immersed in water, which seemingly "belonged to the particle itself". Having observed motion of the pollen of several living plants and assuming it to be a property of living objects, he was surprised to see it even in specimens which had been dried for over a hundred years – and subsequently even in mineral powders, "a fragment of the Sphinx being one of the specimens examined". [76]

In contrast to this random-walk phenomenon which Brown observed, Adolf Fick, demonstrator of anatomy in Zurich, encountered another aspect of diffusion in 1855. Whereas studies had already reported measurements of the diffusivity of various salts in water, Fick sought a more fundamental law describing the phenomenon of diffusion. He found it "quite natural to

suppose" that diffusion in fluids followed the same laws as the conduction of heat and electricity, proposed by Fourier and Ohm respectively, and published his result, $\partial y/\partial t = -k\ \partial^2 y/\partial x^2$, where y is the concentration of substance and k is a "constant dependent upon the nature of the substances" [77]. This result is Fick's second law[7], or the diffusion equation, and shall be used here in the following form:

$$\frac{\partial C(\mathbf{r},t)}{\partial t} = D_T \frac{\partial^2 C(\mathbf{r},t)}{\partial x^2}, \tag{2.31}$$

where the position- and time-dependent concentration is denoted by $C(\mathbf{r},t)$ and the proportionality constant D_T will be discussed presently.

It was then only in the early 1900s that the theory of diffusion was advanced by Albert Einstein and Marian Smoluchowski independently. In one of his four famous 1905 publications, Einstein showed that the coefficient of translational diffusion (D_T) for a small spherical particle suspended in a liquid depends only on the viscosity of the liquid (η) and the size of the particle (radius R),

$$D_T = \frac{k_B T}{6\pi\eta R} \tag{2.32}$$

at absolute temperature T, forming the basis for particle size measurement via the analysis of diffusion dynamics.

Now, we shall look at some of the mathematics of the random-walk problem, and initially consider diffusion in a one-dimensional system. Brownian motion of a particle with mass m is an Ornstein-Uhlenbeck process, [8] and can be described by the Langevin equation for particle speed v,

$$m\frac{dv}{dt} = -\gamma v + \xi(t). \tag{2.33}$$

This is a combination of a frictional force with coefficient $\gamma = 6\pi\eta R$ given by Stokes' law, and a stochastic force given by $\xi(t)$ which is random and uncorrelated:

$$\langle \xi(t) \rangle = 0 \qquad \langle \xi(t_1)\xi(t_2) \rangle = \Gamma \cdot \delta(t_1 - t_2). \tag{2.34}$$

This can be solved for the velocity of the particle, and subsequently for the particle displacement, $\Delta x(t) = x(t) - x(0)$. The mean displacement is $\langle \Delta x(t) \rangle = 0$. However, the mean squared displacement (MSD) in equilibrium in one dimension is given by [78]

$$\langle \Delta x^2(t) \rangle = \frac{\Gamma}{\gamma^2}\left(t - \tau_B\left(1 - e^{\frac{-t}{\tau_B}}\right)\right) \tag{2.35}$$

[7] Fick's first law, $J = -D_T \frac{\partial C}{\partial x}$, relates the diffusion flux J to the concentration gradient $\frac{\partial C}{\partial x}$.

[8] The state variables in Ornstein-Uhlenbeck process follow a normal distribution (Gaussian process), and the probability of each state depends only on the state of the previous event (Markov process).

where $\tau_B = \frac{m}{\gamma}$ is the particle velocity relaxation time due to the drag force and m is the particle's mass. In the limits of short and long times, we obtain

$$\langle \Delta x^2(t) \rangle = \begin{cases} \frac{k_B T}{m} t^2 & \text{for } t \ll \tau_B \\ \frac{2k_B T}{\gamma} t & \text{for } t \gg \tau_B \end{cases} \tag{2.36}$$

where the linear time-dependence of the MSD at longer time scales is a characteristic of free diffusion, and is related to the diffusion coefficient by

$$\langle \Delta x^2(t) \rangle = 2D_T t. \tag{2.37}$$

We now wish to develop a mathematical tool with which to model the propagation of diffusing particles. Using the approach of Berg [79], the number of steps taken by the particle in the $+x$ direction (k) and $-x$ direction ($n-k$) are given by a binomial distribution, $P(n;k) = \frac{n!}{k!(n-k)!}(\frac{1}{2})^k(\frac{1}{2})^{n-k}$ having equal probabilities of both outcomes. Since the collision rate with particles in the environment is very high, n is very large, and the distribution can be modelled by the Gaussian distribution $P(k) = 1/\sqrt{2\pi\sigma_x^2}\exp(-(k-\mu)^2/2\sigma_x^2)$ with mean $\mu = n/2$ and variance $\sigma_x^2 = n/4$. Now, it only remains to express this in terms of the properties of the diffusing system. By inserting $x = (2k-n)\Delta x$ and using the MSD derived above, we get the one-dimensional probability evolution

$$P(x) = \frac{1}{\sqrt{4\pi D_T t}} e^{-\frac{x^2}{4D_T t}}, \tag{2.38}$$

which is a solution to the diffusion equation.

In a higher dimensional system, the derivation is identical for each dimension. In three dimensions, for example, the MSD becomes $\langle |\Delta \mathbf{r}(t)|^2 \rangle = 3\langle \Delta x^2(t) \rangle = 6D_T t$, where $\mathbf{r}$ is an three-dimensional position vector, and

$$P(\mathbf{r}) = \frac{1}{(4\pi D_T t)^{\frac{3}{2}}} e^{-\frac{|\mathbf{r}|^2}{4D_T t}}. \tag{2.39}$$

Diffusion of anisotropic particles. Though the treatment of diffusion shown above applies to arbitrary particles, the diffusion coefficient defined in Equation 2.32 is for a spherical particle. In 1960, S. J. Broersma proposed a diffusion model for long cylindrical particles (length L and diameter d) with aspect ratios $p = L/d \gtrsim 4$ [80, 81], but this model does not apply to shorter rods due to more pronounced end effects [82]. Maria Mercedes Tirado and Jose Garcia de la Torre proposed an improved model in 1979, in which a rodlike particle is modelled as an assembly of beads, and which is valid down to $p \gtrsim 2$ [83, 84]. It may be further noted that this model has proven robust in measurements with even shorter particles with $p \approx 1.4$ [82].

In the Tirado–de la Torre model, the sideways and lengthwise motions of the nanorod are described by their respective diffusion coefficients [84]

$$\begin{aligned} D_T^{\perp} &= \frac{k_B T}{4\pi\eta L}\left(\ln(p) + \nu_{\perp}(p)\right) \\ \text{and} \quad D_T^{\parallel} &= \frac{k_B T}{2\pi\eta L}\left(\ln(p) + \nu_{\parallel}(p)\right), \end{aligned} \tag{2.40}$$

and the macroscopic diffusion coefficient due to random motion is then their average,

$$D_T = \frac{k_B T}{3\pi\eta L}\left(\ln(p) + \nu(p)\right). \tag{2.41}$$

The polynomial functions $\nu_{\perp}(p)$, $\nu_{\parallel}(p)$ and $\nu(p)$ are given by Tirado and de la Torre [83], and the expression to be used in Equation 2.41 is $\nu(p) = 0.312 + 0.565/p - 0.100/p^2$.

2.4.2. The autocorrelation function for diffusion

The diffusion of particles described by the previous section can be quantified from experimental measurements via an analysis of the autocorrelation of a signal produced by the diffusing particle. The autocorrelation of a signal, most commonly measured as the *fluctuation* correlation, measures the similarity of the signal with itself at varying lag times τ, and identifies trends, oscillations and characteristic relaxation times in the signal. We shall use autocorrelation to determine the characteristic decay times of nanoparticle diffusion. For the accurate determination of these time constants, it is imperative to first determine the theoretical autocorrelation function (ACF) for the experimental system being used.

In the first part of this section, we shall review a derivation of the autocorrelation function as holds for conventional FCS based on the approach of Wohland *et al.* [85] In the second part, a new autocorrelation function for diffusion in the standing wave field of a Fabry-Perot resonator, which is a key result of this work, is developed and presented.

Diffusion in a single focal spot. In regular FCS, the observation volume corresponds to a laser focus with depth z_0 and beam waist w_0 and is given by a three-dimensional Gaussian,

$$W_{\mathrm{FCS}}(x, y, z) = e^{\frac{-2x^2}{w_0^2}}\, e^{\frac{-2y^2}{w_0^2}}\, e^{\frac{-2z^2}{z_0^2}} \tag{2.42}$$

(normalised here to unity). Further, while the particle concentration in the sample fluctuates locally in space due to Brownian motion, it is assumed that the average concentration of the sample is constant in space and time, so that [85–87]

$$\langle C(\mathbf{r}, t)\rangle = \langle C(\mathbf{r}, t+\tau)\rangle \tag{2.43}$$

The signal measured from a fluorescing sample is given by the product of the concentration of emitters, $C(\mathbf{r}, t)$, and the intensity of the excitation field $W(\mathbf{r})$:

$$F(t) = \int_V C(\mathbf{r}, t) W(\mathbf{r}) d\mathbf{r}. \tag{2.44}$$

Due to the stationarity in Equation 2.43, the constant average signal can be subtracted, yielding the fluctuation signal $\delta F(t) = F(t) - \langle F(t)\rangle$, and the fluctuation autocorrelation is then given by

$$\begin{aligned} G(\tau) &= \frac{\langle \delta F(t)\delta F(t+\tau)\rangle}{\langle F(t)\rangle^2} \\ &= \frac{\iint W(\mathbf{r})W(\mathbf{r}')\langle \delta C(\mathbf{r},t)\delta C(\mathbf{r}',t+\tau)\rangle d\mathbf{r}d\mathbf{r}'}{\langle \int W(\mathbf{r})C(\mathbf{r},t)d\mathbf{r}\rangle^2}. \end{aligned} \tag{2.45}$$

We construct a "diffusion propagator" using the probability evolution in Equation 2.39 [88],

$$\langle \delta C(\mathbf{r},t)\delta C(\mathbf{r}',t+\tau)\rangle = \frac{\langle C\rangle}{(4\pi D_T\tau)^{3/2}} e^{\frac{-|\mathbf{r}-\mathbf{r}'|^2}{4D_T\tau}}, \tag{2.46}$$

and thus integrate Equation 2.45 to get the ACF for diffusion through a laser focal volume with a geometry given by Equation 2.42:

$$G_{\mathrm{FCS}}(\tau) = \underbrace{\left(1+\frac{4D_T\tau}{w_0^2}\right)^{-1}}_{\substack{\text{Transverse } (xy)\\ \text{contribution}}} \underbrace{\left(1+\frac{4D_T\tau}{z_0^2}\right)^{\frac{1}{2}}}_{\substack{\text{Longitudinal } (z)\\ \text{contribution}}}. \tag{2.47}$$

Fitting experimental data to such a function allows the determination of the translational diffusion coefficient D_T, and thus the average hydrodynamic size of the particles.

Diffusion in a standing wave. We shall now adapt the framework presented above to derive a new ACF for particle diffusion in a Fabry-Perot cavity. In this setup, the field intensity has a distribution given (up to the slowly varying beam radius) by a standing wave,

$$W_{\mathrm{SW}}(x,y,z) = e^{\frac{-2x^2}{w_0^2}} e^{\frac{-2y^2}{w_0^2}} \cos^2(kz), \tag{2.48}$$

with wavenumber $k = 2\pi n_{\mathrm{m}}/\lambda_0$ in a medium with refractive index n_{m}, and Equation 2.45 does not have an analytical solution. A numerical ACF for a standing wave field can be computed [47]; however, in the following, an approximation of the standing wave field equation is proposed, which enables an analytical ACF to be calculated. This analytical expression for the ACF makes it possible to fit the ACF to experimental data and hence directly extract key information, such as the diffusion coefficients, from experimental measurements.

The sinusoidally varying term along the z-direction in Equation 2.48 is approximated by a series of $(2q+1)$ Gaussians, $\mathcal{G}_q(z)$, separated by the period $\lambda_0/2n_{\mathrm{m}}$ of the standing wave nodes:

$$\cos^2(kz) \to \underbrace{\sum_{m=-q}^{q} e^{-s(kz-\frac{mk\lambda}{2})^2}}_{=\mathcal{G}_q(z)} \qquad q\to\infty. \tag{2.49}$$

A scaling factor $s = 2(\cos^{-1}(1/e))^{-2} \approx 1.40272$ is introduced to match the $1/e^2$ levels of the two functions. We use the z-component of the diffusion propagator

$\langle \delta C(z,t)\delta C(z',t+\tau)\rangle = \langle C\rangle/(4\pi D_T\tau)^{3/2}\exp(-(z-z')^2/(4D_T\tau))$ in the autocorrelation integral (Equation 2.45) to get the z-component of the autocorrelation function

$$G_z(\tau) \propto \frac{\iint \mathcal{G}_q(z)\mathcal{G}_q(z')e^{\frac{-(z-z')^2}{4D_T\tau}}dzdz'}{(4\pi D_T\tau)^{1/2}}. \tag{2.50}$$

Using a finite number of nodes, $q < \infty$, Equation 2.50 was integrated and simplified with Wolfram Mathematica, giving a closed-form analytical autocorrelation function. The transverse component can be evaluated as before, and the three-dimensional ACF for diffusion in a standing wave (SW) is then

$$G_{\mathrm{SW}}(\tau) = \underbrace{\left(1+\frac{4D_T\tau}{w_0^2}\right)^{-1}}_{\substack{\text{Transverse } (xy)\\ \text{contribution}}} \underbrace{\frac{\sqrt{2k^2s}}{b_0\sqrt{\pi x}}e^{-\frac{a_0}{x}}\left(1+\sum_{m=1}^{2q} b_m e^{\frac{a_m}{x}}\right)}_{\substack{\text{Longitudinal } (z)\\ \text{contribution}}}, \tag{2.51}$$

where $x = 1 + 2D_Tk^2s\tau$, and a_m, b_m are analytically determined constants. When $q = 1$, Equation 2.51 is identical to $G_{\mathrm{FCS}}(\tau)$.

Note that the contribution due to the transverse field profile is identical to Equation 2.47. A comparison of the ACFs obtained from this model with varying q suggests that the second decay time constant (see Figure 2.5 (b)) is due to diffusion through multiple antinodes, i.e. due to the periodicity of the field seen by the nanoparticle. The ACFs converge with increasing q, and in the rest of the work[9], we use the ACF evaluated with eleven antinodes. As shown in Figure 2.5 (c), both decays in the autocorrelation curve shift to longer times with increasing particle size; however, their relative amplitudes remain unchanged. The beam waist in the cavity has a minor effect on the ACF at longer timescales, and leaves the first (short) diffusion decay practically unchanged.

It should be noted here that the ACFs given in Equations 2.47 and 2.51 are based on the assumption of stationarity, i.e. that every possible path is sampled by a diffusing nanoparticle. Differing statistical behaviour will lead to a deviation of the autocorrelation from these ACFs especially at longer lag times, as we shall see in Chapter 4.

2.4.3. The autocorrelation function for rotation

Rotational diffusion. In addition to the diffusional motion described in Section 2.4.1, particles also suffer random changes in their orientation, which we call rotational diffusion. This is particularly apparent in experiments with linearly polarised excitation light, in which the orientation-dependent emission or scattering behaviour of anisotropic particles is noticeable, and was considered by Francis Perrin as early as 1926 [90].

We shall now derive the mathematical framework for rotational diffusion similarly to Section 2.4.1, following the approach of Jain and Sebastian [91]. When first considering rotational diffusion around a single axis, the particle orientation is defined by a single angle ϕ which

[9] A typical microcavity accomodates about 15 antinodes.

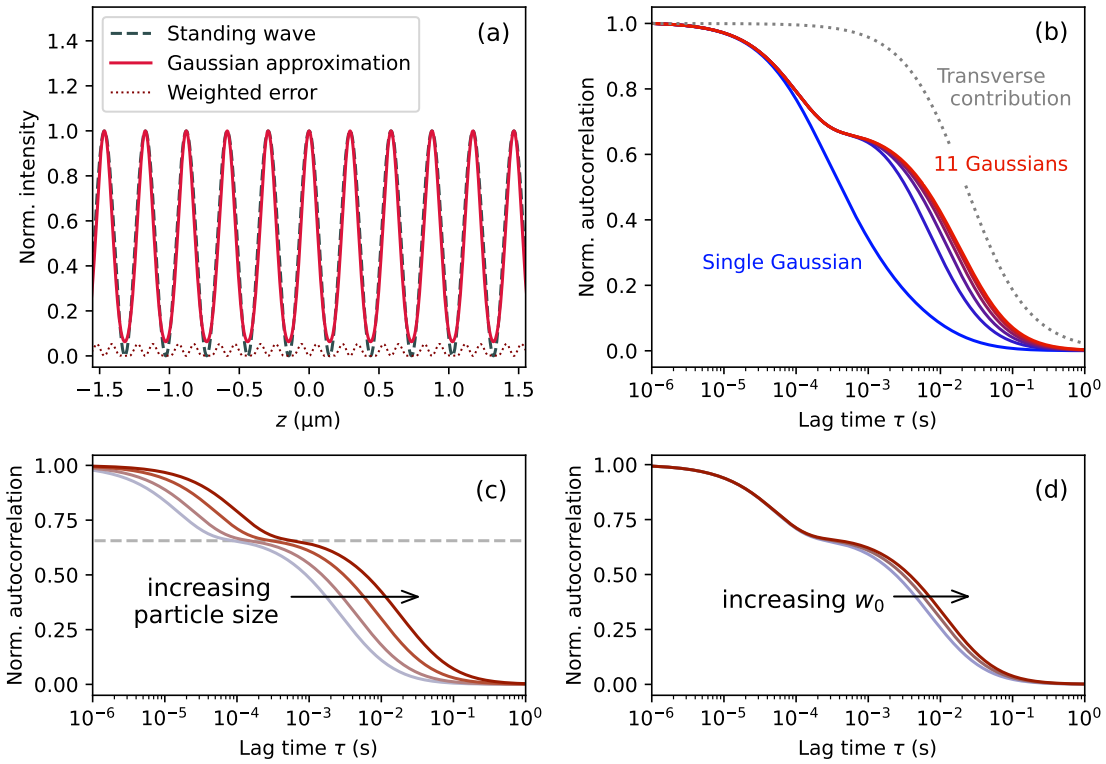

Figure 2.5: (a) The approximation of a standing wave intensity profile by a series of Gaussians with spacing $\lambda/2$. (b) The ACF with a varying number of Gaussians. The curve with a single Gaussian is identical to the case of FCS. The contribution of the transverse Gaussian profile also remains unchanged. (c) $G_{\mathrm{SW}}(\tau)$ plotted for particle diameters of 3 nm, 5 nm, 10 nm and 20 nm, showing the decay times increasing with particle size. The height of the minimum slope point between the two decay remains unchanged. (d) The slight dependence of $G_{\mathrm{SW}}(\tau)$ on cavity geometry (beam waist w_0 = 1.2 µm, 1.4 µm, 1.6 µm) arises from the transverse contribution "cutting off" the longitudinal component. [89].

defines the orientation of a two-dimensional unit vector $\hat{\mathbf{u}}$ moving randomly around a circle. This gives an expression analogous to Fick's Law:

$$\frac{\partial P(\phi,t)}{\partial t} = D_R \frac{\partial^2 P(\phi,t)}{\partial \phi^2} \tag{2.52}$$

where $P(\phi,t)$ is the probability density of the particle being found in orientation ϕ and D_R is the rotational diffusion coefficient. While the problem resembles that in Section 2.4.1, it must be noted that now $P(\phi) = P(2\pi+\phi)$. The probability evolution for the two-dimensional orientation of a nanoparticle starting at $\phi = 0$ is then

$$\begin{aligned} P(\phi,t) &= \frac{1}{2\pi}\sum_{m=-\infty}^{\infty} e^{-m^2 D_R t} e^{im\phi} \\ &\approx \frac{1}{\sqrt{4\pi D_R t}} e^{-\frac{\phi^2}{4D_R t}} \end{aligned} \tag{2.53}$$

where the approximation holds for small time steps t. This is equivalent to one-dimensional translation (Equation 2.38), i.e. diffusion along a line, since at small time delays, $\hat{\mathbf{u}}$ does not

see the curvature of the circle on which it moves. The mean squared angular displacement (MSAD) is $\langle \Delta\phi^2 \rangle = 2(1 - \exp(-D_R t))$ which, for small t, becomes $\langle \Delta\phi^2 \rangle \approx 2D_R t$, analogous to Equation 2.37.

On the other hand, at large t, the behaviour of rotational diffusion defers from translational diffusion. The orientation vector then experiences the curvature and periodicity of the unit circle on which is diffuses, the probability distribution becomes uniform, $P(\phi, t \to \infty) = 1/2\pi$, and the MSAD has an upper bound.

This approach is now extended into three dimensions so that $\hat{\mathbf{u}}$ is defined by azimuthal angle ϕ and polar angle θ, and moves around on the surface of a unit sphere, giving an analogy to Equation 2.52 in three dimensions: $\partial P(\hat{\mathbf{u}}, t)/\partial t = D_R \nabla^2 P(\hat{\mathbf{u}}, t)$ [92]. Then, the solution for the time evolution of $P(\hat{\mathbf{u}})$ under the initial condition $\hat{\mathbf{u}}(t = 0) = \hat{\mathbf{u}}_0$ is given by a series of spherical harmonic functions [93, 94]

$$P(\hat{\mathbf{u}}, t) = \sum_{l=0}^{\infty} \sum_{m=-l}^{l} Y_{lm}(\hat{\mathbf{u}}_0) Y_{lm}^*(\hat{\mathbf{u}}) e^{-l(l+1)D_R t} \tag{2.54}$$

where $\hat{\mathbf{u}}_0$ represents the initial orientation. If we assume, without loss of generality, that $\hat{\mathbf{u}}_0 = \hat{\mathbf{z}}$, i.e. $\theta(t = 0) = 0$, then the probability distribution is a function of the polar angular displacement and independent of ϕ: $P(\hat{\mathbf{u}}, t) \to P(\theta, t)$.

When obtaining a result for $P(\theta, t)$, we can once again distinguish between short and long time scales. At short times, we get

$$P(\theta, t) = \frac{1}{\sqrt{4\pi D_R t}} e^{-\frac{\theta^2}{4D_R t}} \tag{2.55}$$

where the small angle approximation was used [91], and the MSAD in *three dimensions*, $\langle \Delta\Phi^2 \rangle = 2(1 - \exp(-2D_R t)) \approx 4D_R t$, resembles translation on a plane in two dimensions. This again arises from negligible curvature over the small region on the sphere accessed at short times. At longer times, the probability distribution becomes uniform and the probability of a given orientation becomes $P(\hat{\mathbf{u}}, t \to \infty) = 1/4\pi$.

The rotational autocorrelation function. According to Peet Kask [93], the rotational ACF can be separated from the translational ACF, since their characteristic decays typically occur at very different time scales. The orientation-dependent components of the ACF are separated from the isotropic part to yield a rotational factor which depends on the geometry of the experiment. This factor is determined from Equation 2.54 and is given by [93, 94] $\mathsf{r}(\tau) = \sum_l B_l \exp(-l(l+1)D_R\tau)$, where B_l are geometry-dependent constants. Now, due to the symmetry of the problem, only terms with $l = 0, 2, 4$ survive [93, 95]. Furthermore, the $l = 4$ term is negligible compared to the other two, so that the rotational factor can be reduced to the form $\mathsf{r}(\tau) = 1 + r\exp(-6D_R\tau)$, where r is a factor describing the prominence of the rotational decay. The normalised ACF for rotation is now

$$G_{\text{rot}}(\tau) = \frac{1 + re^{-6D_R\tau}}{1 + r} \tag{2.56}$$

and the total ACF for the translational and rotational diffusion of a nanoparticle is given by $G(\tau) = G_{\text{trans}}(\tau) \cdot G_{\text{rot}}(\tau)$, where $G_{\text{trans}}(\tau)$ takes the form of Equation 2.47 or Equation 2.51.

Theories for the rotational diffusion of a rodlike particle have also been proposed by Broersma as well as Tirado and de la Torre. Once again, we take advantage of the Tirado–de la Torre model's applicability to short rods, and use the diffusion coefficient

$$D_R = \frac{3k_BT}{\pi\eta L^3} \left(\ln(p) + \delta(p)\right). \tag{2.57}$$

for reorientation of the rod's axis, with $\delta(p) = 0.662 + 0.917/p - 0.050/p^2$ [83], in Equation 2.56 to analyse the rotational dynamics of nanorods.

Laser-machined and high-reflectivity-coated optical fibres such as this one form the heart of a fibre-based Fabry-Perot microcavity.

3. Implementation of a microcavity-based nanoparticle sensor

3.1. The optofluidic microcavity

The core of the nanoparticle sensor is the intersection of an optical beam and a microfluidic channel: this is the optofluidic cavity itself. The cavity is housed in a quartz fibre-optic ferrule[1] with a Ø 131 µm bore along its length, which was chosen to just accommodate the diameter of the cavity fibres (see Section 3.1.1) with minimal play, while also reducing friction between the fibre and the ferrule walls. A microfluidic connection is created by laser-drilling conical holes into the ferrule perpendicular to the bore, and is further explained in Section 3.1.4. The fibres are inserted into the ferrule bore from either side, such that the cavity formed between their tips lies within the microfluidic channel (see Figure 3.1), and the cavity length and fibre alignment is adjusted with a 3-axis micropositioning stage[2] and rotation mount[3]. The microcavity stage, designed by Larissa Kohler [47], is made of Macor, a low-expansion ceramic which offers excellent thermal stability, and is mounted on a vibration-reducing rubber slab for improved mechanical stability as well. Additionally, a foam-lined acrylic cover provides protection to the setup from acoustic disturbances.

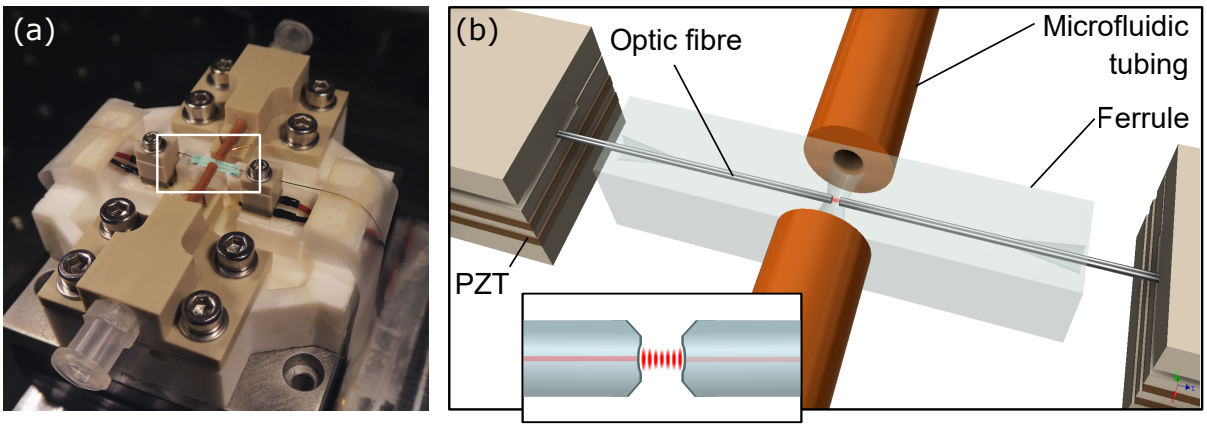

Figure 3.1: (a)) Photograph of the optofluidic platform. Two fibres are inserted into the ferrule (highlighted in blue) from the left and right, and the sample in aqueous dispersion is injected through the orange tubes. (b) Zoomed illustration of the central part of (a), with the cavity mode between the fibres shown inset.

[1] OZ Optics, FER-1.225-1.225-131-GL
[2] Thorlabs Nanomax 3-axis stage with differential drives
[3] Thorlabs Fibre Rotator HFR007

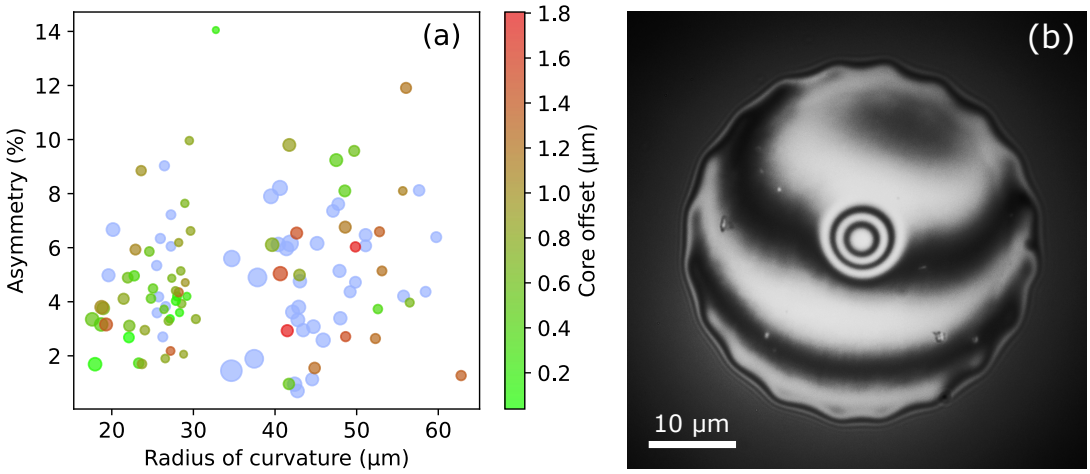

Figure 3.2: (a) Properties of the mirror profiles produced in this work. The size of each point represents its profile depth, ranging from 0.5 µm to 2.3 µm. The green-red colour scale corresponds to the misalignment from the core, and applies to single-mode fibres only. The two distinct clusters of fibres visible in the plot were shot with focussing lenses having focal lengths of 0.5" and 1" respectively. (b) Interferometric image of a single-mode fibre with radius of curvature 28.5 µm, taken with 455 nm illumination[7].

3.1.1. The cavity fibres

The cavity fibres are the *central* part of the microcavity, since they form the mirrors of the optical resonator. The mirror profiles are machined into the end-facets of single-mode[4] and multimode[5] fibres using ablation by a pulsed CO_2 laser[6]. By varying the laser shot parameters, profiles with radii of curvature between 15 µm and 60 µm were produced. Fibre machining was done according to the procedure developed by David Hunger *et al.* [44]

For larger radii of curvature, however, the profiles tend to become elliptical. To keep the asymmetry low (~ 5%), a double-shot procedure was developed and optimised to compensate for the ellipticity of single shots, in which two shots were fired at a small distance $\Delta x \approx 7$ µm from each other. This is particularly important to keep the polarization splitting of fundamental cavity modes low.

Subsequently, the fibres are commercially coated with a Bragg mirror stack by ion-beam sputtering. The coating used for the fibres in this work (35 alternating layers of Ta_2O_5 ($n_H \approx 2.1$) and SiO_2 ($n_L \approx 1.4$))[8] is designed for a transmission of $\mathcal{T} = 20$ ppm in air at $\lambda_0 = 780$ nm. The final high refractive index layer forms a node at the mirror surface, which reduces the effect of scattering loss at the surface since the electric field vanishes at this point. The scattering and absorption losses of these mirrors have been estimated to be $\mathcal{S} = 17$ ppm [47].

Most of the experiments shown in the following chapters were done with fibres having average radii of curvature 41 µm and 43 µm respectively.

[4] IVG Fiber, Cu800
[5] Artphotonics MMG50-125-170AL
[6] Synrad Firestar V30
[7] Thorlabs M455F1 fibre-coupled LED
[8] Laseroptik GmbH, coating B-12559-01 HR780nm/0°: Substrate | 1.648H 0.615L (H L)^{16} H, where H and L stand for high and low refractive index quarter optical wavelength layers

3.1.2. Cavity scanning and active stabilisation

A precise mechanism for the control of cavity length is essential for the fully tuneable cavities implemented in this work. Whereas the original resonator of Fabry and Perot was tuned using small rubber bags filled with water to vary the pressure exerted on metal flexure parts [38], in this work, the cavity length was modulated with piezo-electric transducers (PZTs)[9] driven by an arbitrary function generator (AFG)[10] or FPGA board, enabling precise control of the cavity length on the sub-nanometre scale. In all cases, light transmitted through the cavity was detected with an avalanche photodiode (APD)[11] having a 3 dB bandwidth of 50 MHz.

The cavity can be operated in one of two modes: scanning mode or locked mode. In **scanning mode**, a triangular wave is generated by the AFG and fed to the PZTs after amplification by voltage amplifiers[12]. The cavity length can be scanned over a maximum range of about 1 µm with a driving voltage of ± 175 V. The cavity is scanned over a resonance for linewidth measurement (see Section 3.1.3), and the cavity has also been used in scanning mode with multi-wavelength excitation for the tracking of single nanoparticles [41].

The motivation to move to a cavity-locked detection scheme arises from the bandwidth limitation of the scanning cavity. While measurements of nanoparticles with diameters of 120 nm have been reported with a cavity scanned at 14 kHz [47], the detection of particles smaller than 10 nm and of faster dynamics such as rotation and folding necessitate measurement speeds many orders of magnitude faster (> 10 MHz), which is not possible with a scanning mechanism.

To implement a **locked cavity**, an FPGA board[13] which functions as an oscilloscope, PID controller and signal generator on a single platform was implemented. Active stabilisation of a fibre-fibre microcavity has already been demonstrated [40, 42, 96, 97], albeit with different hardware and various locking schemes. The cavity in this work was stabilised using the side-of-fringe lock. Here, a locking point is chosen on the flank of the resonance peak, so that any change in optical length of the cavity ("horizontal" movement of the resonance) is immediately translated into a measureable change in cavity transmission. As we shall see in Chapter 4 (see Figure 4.2 (a)), this is a sensitive approach to detect disturbances due to nanoparticles interacting with the cavity mode.

In this locking scheme, the cavity transmission is the error signal fed to the PID controller. The controller produces a feedback signal $\xi(t)$ which is amplified and supplied to one PZT. Since the maximum output of the FPGA board is ± 1 V (after amplification: ± 20 V), one PZT was manually controlled with a DC signal from the AFG. Since the AFG has a higher output range of ± 10 V (amplified up to ± 175 V), it was thus possible to correct for slow drifts over a larger range than with only the FPGA board.

The lock was controlled using the PyRPL software [98], in which lock stages and parameters can be set up. For the application of nanosensing, it is important that fast fluctuations caused by nanoparticle interactions are not corrected by the lock. Furthermore, despite the most sensitive set point lying at 75% of the resonance peak height [57], where the slope is steepest, the set

[9] Noliac NAC2402-H2.3
[10] Rigol DG1022
[11] Thorlabs APD110A/M
[12] Falco Systems WMA-02
[13] Red Pitaya STEMLab 125-14

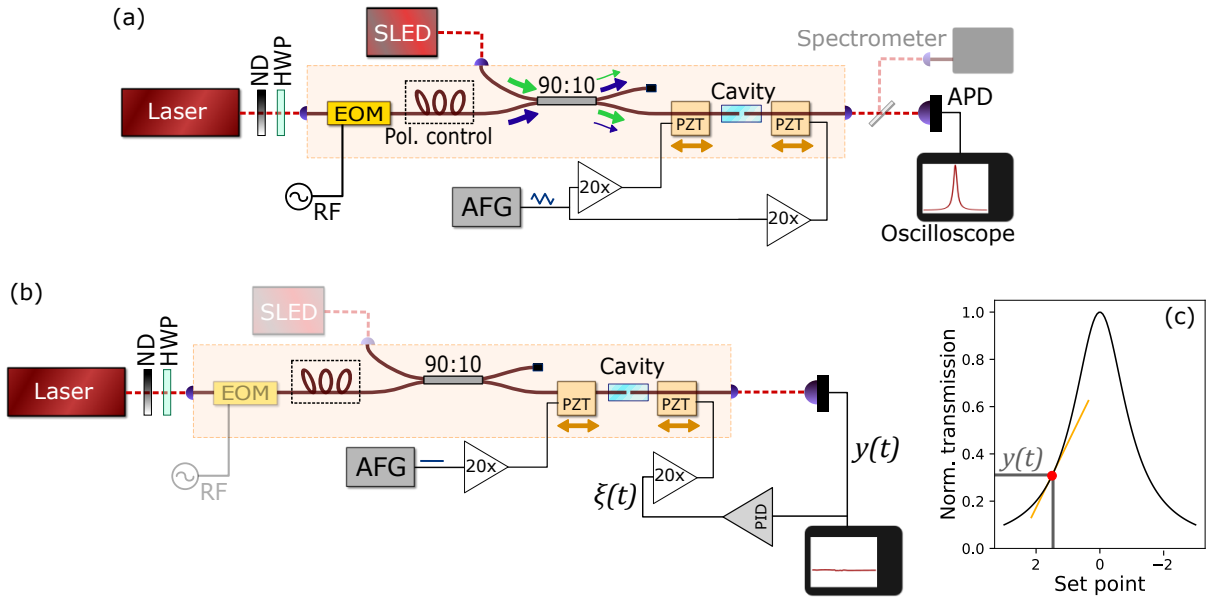

Figure 3.3: (a) Optoelectronic setup for cavity characterisation. The shaded section is entirely fibre-based. For cavity length measurement, the spectrum from the superluminiscent light emitting diode (SLED) is recorded by a grating spectrometer via a magnetically mounted mirror. (b) The setup in cavity-locked mode, in which the cavity output is used as the error signal for side-of-fringe locking with a PID controller. (c) Schematic of the side-of-fringe lock with the set point at 1.5 linewidths shown as a red dot. The transmission signal, $y(t)$, is sensitive to cavity length fluctuations and is used by the PID controller to generate a feedback signal to keep the cavity at the set point.

Step no.	⓪	①	②	③
Set point	2.0	2.0	2.0	1.5
Gain	(1)	80	60	20
Function	Reset	Lock		

Table 3.1: Lock parameters for nanoparticle sensing. Steps ⓪ – ② initialise the lock and find the flank of the resonance, and step ③ is the final lock state, giving a stability of about 300 fm. The lock bandwidth given by its unity-gain frequency is 80 Hz. The "set point" is defined as the cavity detuning from the resonance peak in linewidths.

point in this work is chosen further down at about 30% of the peak amplitude, defined by the "set point" 1.5 linewidths away from the peak, which provides a larger useable measurement region for dispersive shifts by nanoparticles. Typical lock parameters used are given in Table 3.1. These are a compromise between good cavity stability and unattenuated nanoparticle event detection, as is further discussed in Section 4.1.2.

It may be noted here that we often consider cavity properties in different units, depending on the measurement method and purpose. A scanned cavity is modulated in **length** by the PZT, but the resulting cavity transmission trace measured on the oscilloscope is in the **time** domain (e.g. Figure 3.4 (a) and (b)). For a linear scan (e.g. the PZTs are driven with a triangular waveform), the length and time domains are roughly proportional (up to the nonlinearity of the PZT) and are used interchangeably.

Meanwhile, the cavity also acts as a spectrometer, so that changes in cavity length correspond to changes in resonance **frequency**, and hence in resonance **wavelength**. Since resonances with a fixed excitation wavelength occur at cavity length intervals of $\lambda_0/2n_m$, we compare this quantity to the frequency-domain FSR,

$$\underbrace{\frac{\lambda_0}{2n_\mathrm{m}}}_{\text{Length domain}} \quad \bullet\!\!-\!\!\circ \quad \underbrace{\frac{c_0}{2n_\mathrm{m}\ell}}_{\text{Frequency domain}}, \tag{3.1}$$

which yields the conversion

$$\delta\nu = b \cdot \delta\ell \quad \text{where } b = \frac{c_0}{\lambda_0 \ell} \tag{3.2}$$

for transforming changes in the length domain to frequency units.

Converting changes in resonant wavelength to frequency is simply done using calculus, with $\delta\nu = -\delta\lambda(c_0/\lambda_0^2)$.

3.1.3. Characterisation of the microcavity

Finesse. The optical figure of merit of the microcavity, the finesse, is determined via measurements of the cavity linewidth and of the cavity length [47], and a new, custom-written graphical user interface. The **cavity linewidth** is determined by operating the cavity in scanned mode and imposing frequency sidebands with a known separation, $\Delta\nu_\mathrm{EOM}$, on the resonance with an electro-optic modulator (EOM)[14] driven by a radio frequency (RF) generator[15] (see Figure 3.4 (b)). The linewidth in frequency units, FWHM_ν, is then calculated from the oscilloscope trace using $\mathrm{FWHM}_\nu = \mathrm{FWHM}_t \cdot (\Delta\nu_\mathrm{EOM}/\Delta t_\mathrm{EOM})$, where FWHM_t and Δt_EOM are the linewidth and sideband separation in terms of scan position, respectively.

The **cavity length** is measured spectroscopically. The cavity is excited by a broadband superluminiscent light emitting diode (SLED)[16] emitting at 750 nm – 770 nm, resulting in resonances in the wavelength domain, from which the free spectral range and hence the optical cavity length can be determined. With these two quantities known, the finesse is calculated using Equation 2.13. As the cavity length decreases below about 5 µm, the FSR is so large that only one resonance mode family can be illuminated within the bandwidth of the SLED. In this case, the cavity length is estimated using the separation between higher-order transverse modes and Equation 2.22 (Figure 3.4 (c)).

Stability. For cavity-locked detection, the stability of the cavity is very important. The root-mean-square (RMS) jitter in cavity length, $\delta\ell$, was estimated by linearising the Lorentzian resonance curve around the set point to a line with slope K. The fluctuations δT in cavity transmission (Figure 3.4 (d)) were measured as voltage fluctuations δV in the cavity transmission signal, and converted into length jitter using the slope K [57]:

$$\delta\ell = K \cdot \delta V \qquad \text{with} \quad K = \frac{8\mathcal{F}V_\mathrm{set}^2}{\lambda V_\mathrm{peak}}\sqrt{\frac{V_\mathrm{peak}}{V_\mathrm{set}} - 1} \tag{3.3}$$

[14] Photline NIR-MPX800
[15] DS Instruments SG4400L
[16] Exalos EXS75005-B001 G1-0067-1 194E

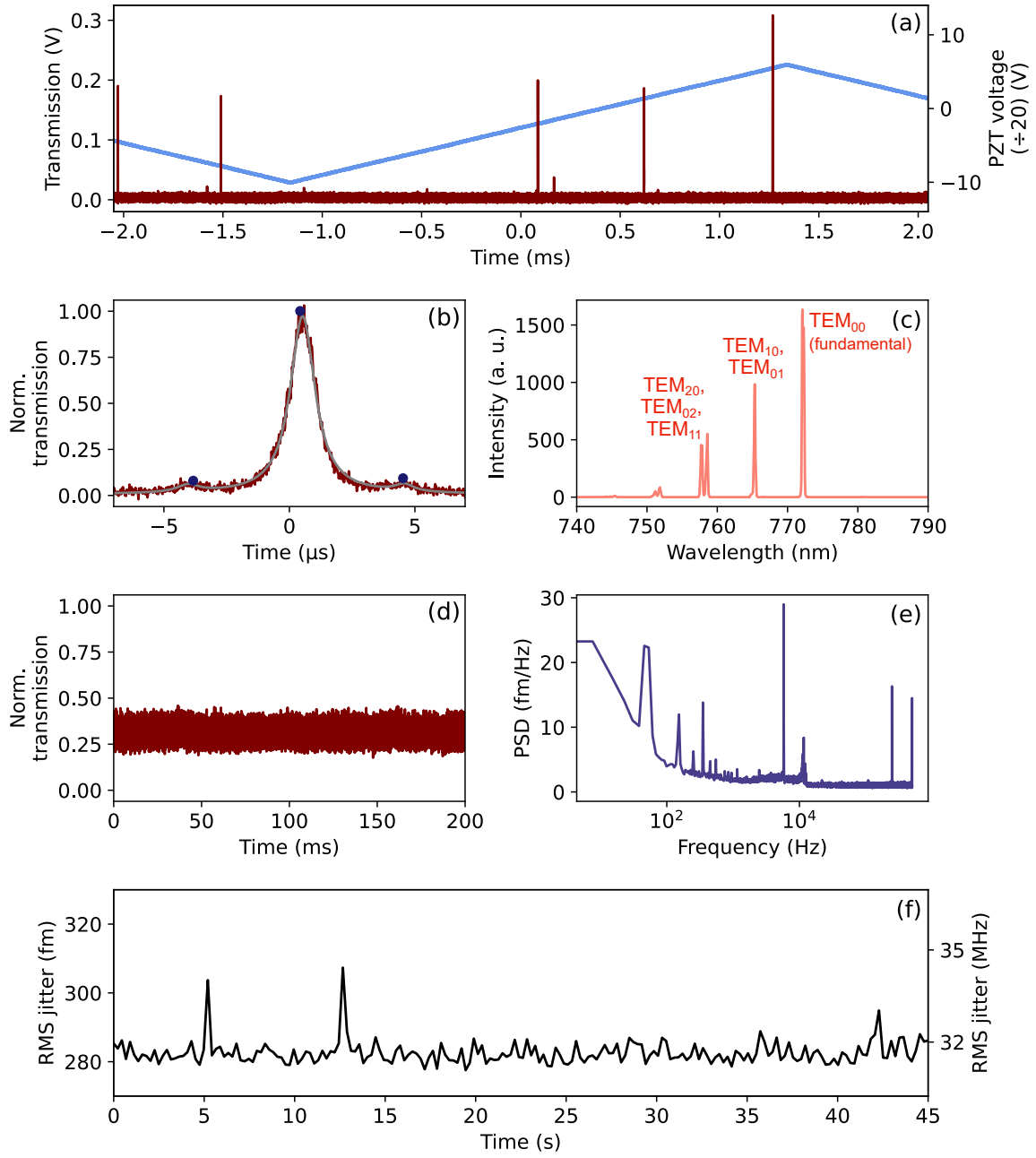

Figure 3.4: (a) A cavity length scan (indicated by the PZT voltage in blue) showing over three resonance families in cavity transmission (maroon). The scan amplitude corresponds to about 900 nm. (b) A cavity resonance with frequency sidebands at $\Delta\nu_{\mathrm{EOM}}$ used for calibrating the linewidth. The carrier and sideband peaks are highlighted with circles. The extent of the scan shown here corresponds to a length modulation of about 50 pm. (c) The broadband transmission spectrum of a short cavity showing higher order transverse modes. The corresponding frequency difference $\Delta\nu_{\mathrm{transverse}}$ is used for length measurement via Equation 2.22. (d) Transmission of a locked cavity, and (e) its noise spectrum as a power spectral density (PSD) plot scaled to length jitter. (f) The effective root-mean-square (RMS) length jitter of the cavity over a time span of 45 seconds, showing an average instability of around 280 fm (32 MHz).

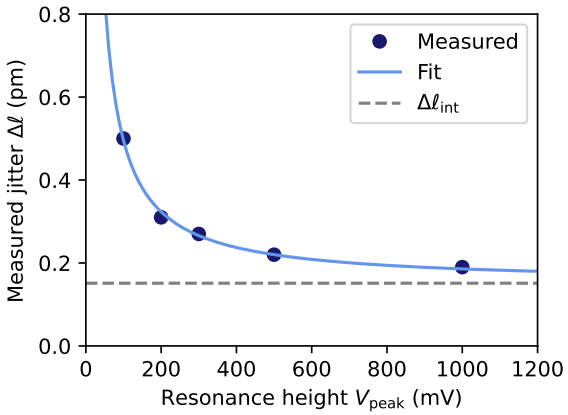

Figure 3.5: Effective cavity instability measured with various peak amplitudes. With resonance peaks having lower V_{peak}, the effect of dark electronic noise dominates. Taller resonances show a high SNR, so that the intrinsic cavity length jitter dominates, and extrapolating to infinite SNR gives an estimate of the intrinsic cavity length jitter, here 150 fm.

where V_{set} and V_{peak} are the values of the transmission signal (voltage) at the set point and the resonance peak respectively. Using Equation 3.2, this can be expressed as a frequency jitter, $\delta\nu = b \cdot \delta\ell$. The measured cavity instability was typically 300 fm, corresponding to a frequency jitter of 32 MHz. A calculation of the power spectrum of the locked cavity signal (Figure 3.4 (e)) gives an insight into the sources of noise: Up to a few 100 Hz, $1/f$ noise is dominant, which is attributed to electronic noise and frequency and power fluctuations from the lasers. An unavoidable peak at 50 Hz arises from the mains power supply. The peaks at higher frequencies, extending into hundreds of kHz, are thought to arise from the electronic systems in operation, but it has also been shown that vibration modes of the fibre tips can have mechanical resonances in this frequency range [99].

One should note that the value of $\delta\ell$ measured in this manner represents an effective signal instability arising from cavity length jitter and (dark) electronic noise. The electronic noise from the APD and oscilloscope δV_{dark} corresponds to a fictitious cavity jitter of $\delta\ell_{\text{dark}} = \delta V_{\text{dark}}/K$. Since $K \propto V_{\text{peak}}$, it follows that $\delta\ell_{\text{dark}} \propto 1/V_{\text{peak}}$, i.e. the measured cavity instability increases for resonance peaks with lower amplitude due to the decreased SNR. The intrinsic cavity instability due to actual length fluctuations was estimated by measuring $\delta\ell$ over a series of resonance peak voltages. The results could be fit to the function $\delta\ell = \delta\ell_{\text{int}} + A/V_{\text{peak}}$, where $A = \delta V_{\text{dark}}\lambda/(8\mathcal{F}\sqrt{V_{\text{set}}/V_{\text{peak}} - V_{\text{set}}^2/V_{\text{peak}}^2})$ is independent of peak amplitude. In Figure 3.5, the measured jitter decreases asymptotically towards 150 fm, which is the intrinsic cavity instability extrapolated from an infinite SNR. The effective instability is then the sum of this value and of the aforementioned dark electronic noise, whose effect increases with decreasing signal SNR.

The optical properties and stabilities of some cavity configurations used for the measurements shown in Chapter 4 are listed in Table 3.2.

The resonance peak amplitude was set to 200 mV in most measurements, for which 10 µW – 20 µW of laser power was typically required. This was low enough to avoid photothermal effects such as resonance broadening or distortion of the resonances. This corresponds to an average intracavity power of 30 mW – 60 mW circulating at the lock set point (≈ 30% of the resonance peak height).

Number	Cavity length (µm)	Linewidth (MHz)	Finesse	RMS jitter (fm)
1	4.39 ± 0.04	531 ± 2	42000 ± 300	344 ± 4
2	4.6 ± 1.8	476 ± 4	45000 ± 16000	338 ± 5
3	3.7 ± 0.7	446 ± 3	58000 ± 9000	300 ± 26
4	3.4 ± 0.2	574 ± 8	48000 ± 2000	282 ± 3

Table 3.2: Optical and mechanical properties of the cavities used for nanoparticle experiments, measured over the course of several months. The uncertainty in jitter is determined by the standard deviation over about one minute.

3.1.4. The microfluidic system

In this section, we shall look at the "microplumbing" which turns the optical microcavity introduced thus far into an optofluidic platform.

A tapered microchannel was laser-drilled[17] into both sides of the fibre ferrule, perpendicular to the fibre bore, with an opening diameter of 400 µm and a diameter of about 150 µm at the middle of the ferrule. The fibre tips are therefore completely contained in the fluidic channel, and the entire cavity mode lies within the sample.

PEEK tubes[18] were glued at the opening of the tapered channel on the ferrule using a procedure demonstrated previously [97]: silicone adhesive[19] was spread on the cut end of the tube and allowed to partially dry, forming an o-ring *in situ*, and fully cured with UV light after being positioned in place. These tubes were connected to female Luer fittings via a custom-made adapter, providing a standardised port for connections with various components via the framework of the Luer system.

To flush the cavity with copious amounts of clean water, alcohol or air, a homebuilt system driven by pressurised air adapted from previous work [47] was employed, and equipped with Luer connectors for easy connection to the cavity platform. To purge the cavity with air, a compressed air supply can be directly connected to the cavity via the Luer connector (see Figure 3.6 (a)).

When dealing with nanoparticle samples to be measured, it is desirable to minimise the volume required, and the approach used in previous work lead to a substantial unused volume in the tubing before the sample reaches the cavity. To avoid this, samples can now be introduced into the cavity via the Luer connector by direct injection with a 1 mL syringe (Figure 3.6 (b)). In this form, only 600 µL of liquid are required to completely fill the cavity. Further optimising the microfluidic setup, for example by shortening the PEEK tubes and eliminating bulky adapters, could possibly even reduce this to < 100 µL.

Additionally, if filtering of the sample is desired, syringe filters[20] can be inserted between the syringe and the connector to the cavity (Figure 3.6 (c)). The implementation of the Luer connector system in the setup therefore enhances the efficiency and flexibility of the fluidic system.

[17] LPKF Protolaser; the channels were machined by Georg Gramlich at the Institute of High-frequency technology and Electronics (IHE) at KIT
[18] Cytiva PEEK tube, inner diameter = 0.5 mm, outer diameter 1/16" = 1.58 mm from Fisher Scientific
[19] Loctite Si 5091 LC
[20] e.g. Millex 0.1 µm PVDF syringe filters

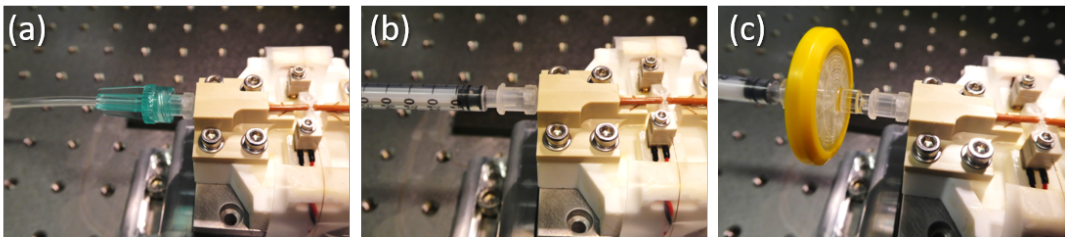

Figure 3.6: The fluidic input to the cavity connected to (a) a pressurised air supply, (b) 1 mL syringe, and (c) syringe-driven filter via Luer connectors.

Figure 3.7: From left to right: gold nanospheres with diameters 3 nm, 5 nm, 10 nm, 15 nm and 20 nm; gold nanorods with plasmon resonances at 700 nm, 650 nm and 600 nm; bovine serum albumin.

3.2. Samples

Gold nanoparticles. Gold nanospheres and nanorods were used as experimental models with which to characterise and test the nanoparticle sensor:

- **Gold nanospheres**[21] with diameters d from 3 nm to 20 nm were measured in this work. Nanospheres with d = 20 nm are shown in Figure 3.9 (a). TEM images provided by the manufacturer of all nanosphere sizes are shown in Figure A.3 in Appendix A.
- Three sizes of **gold nanorods**[22] were used: (1) L = 25 nm × d = 10 nm (surface plasmon resonance at 650 nm), (2) 20 nm × 10 nm (600 nm) and (3) 15 nm × 5 nm (700 nm). These were the smallest sizes available from the manufacturer.
  Nanorods with L = 20 nm and d = 10 nm are shown in Figure 3.9 (b). TEM images provided by the manufacturer of all three nanorod samples are shown in Figure A.4 in Appendix A.

The particles were supplied in aqueous suspension with cetyltrimethylammonium bromide ($(C_{16}H_{33})N(CH_3)_3Br$, CTAB) or citrate ($C_3H_5O(COO)_3^{3-}$, CIT) as stabilisers. **Citric acid** plays an important role in the manufacture of gold nanospheres. After the formation of gold particles

[21] Nanopartz Inc., product numbers A11-XX-CIT-DIH-1 in citrate and A11-XX-CTAB-DIH-1 in CTAB, where XX is the nominal size in nanometres (3, 5, 10, 15, 20).

[22] Nanopartz Inc., product numbers A12-10-600-CIT-DIH-1 (10 nm × 20 nm), A12-10-650-CIT-DIH-1 (10 nm × 25 nm), A12-5-700-CIT-DIH-1 (5 nm × 15 nm) in citrate buffer, and the corresponding product in CTAB.

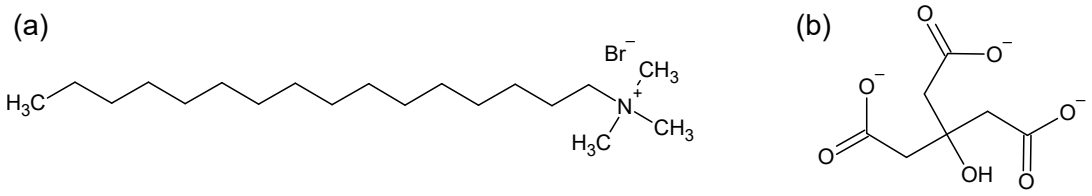

Figure 3.8: Chemical structures of (a) CTAB and (b) CIT.

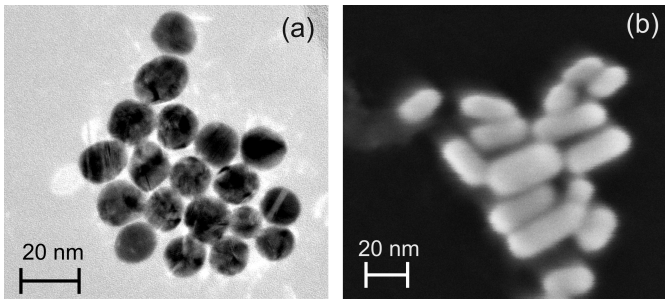

Figure 3.9: (a) TEM image of 20 nm gold nanospheres. (b) SEM image of 20 nm × 10 nm gold nanorods.

from a gold solution, citrate ligands adsorb onto the nanoparticle surface, imparting a negative charge to the particles, hence acting as a stabiliser and hindering agglomeration [100]. **CTAB**, on the other hand, is a positively charged surfactant which binds to gold nanoparticles as a bilayer, and enables the formation of rodlike particles anisotropically restricting crystal growth of gold particles. The CTAB bilayer has been reported to be several nanometres thick, e.g. a thickness of 3.2 nm reported by Gomez *et al.* [101] or ≈ 6 nm by the manufacturer [100]. At the concentrations used in our samples (in general at > 1 mM), CTAB forms micelles which also improve particle stability. Due to its high toxicity, however, it is not suitable for experiments where biocompatibility would be desired [100, 102].

It is worth mentioning here that the size and shape of nanoparticles changes with time by the Ostwald ripening process. Gold atoms from particle regions with tight curvature leave the particle and are deposited elsewhere, leading to smaller particles getting smaller and larger particles increasing in size [102]. This means that the polydispersity of a nanoparticle sample naturally worsens over time.

Biomolecules. In order to demonstrate the application of this nanoparticle sensor to biosensing, two biological samples were studied:

- **Bovine serum albumin (BSA)**[23], a protein from bovine plasma, was used for surface treatment of the microfluidic setup and was also sensed independently.
  BSA has a molecular weight of 66.5 kDa and is widely used in biotechnology, for example as a carrier protein or a standard for protein assays. Though the molecule has a complex, roughly triangular shape (see Figure 3.10), it has been approximated to behave hydrodynamically like an ellipsoid with $L \approx 14$ nm and $d \approx 4$ nm [103].

[23] Bovine serum albumin, fraction V, 7.5% solution from ThermoFischer Scientific

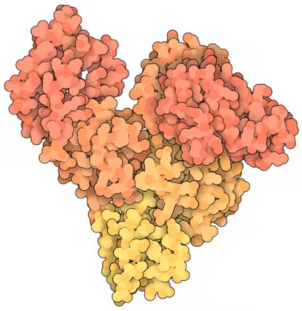

Figure 3.10: Molecular artwork of the BSA protein molecule. Image from Sigma-Aldrich Co., courtesy of Dr. David Goodsell (2013) [104].

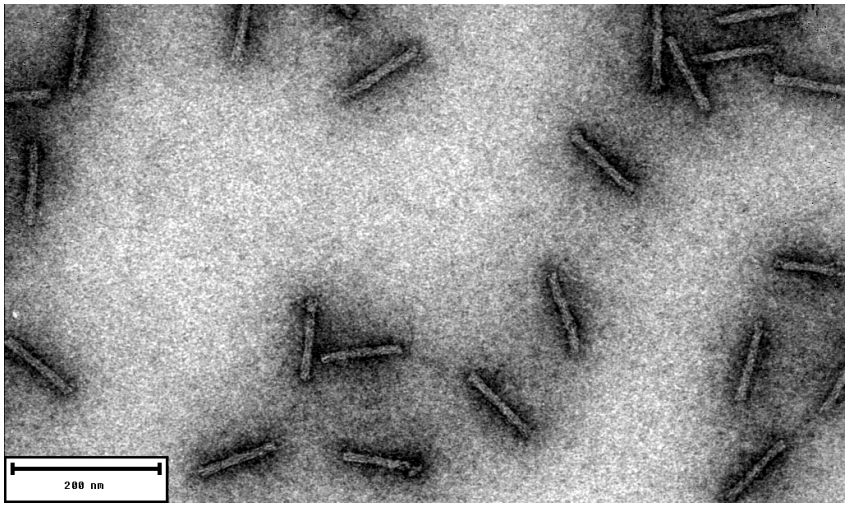

Figure 3.11: Electron microscope image of DNA "origami" nanostructures from Prof. Tim Liedl's group. Image provided by Chris Pauer, LMU Munich.

- Single **DNA "origami" nanostructures**[24] approximately 120 nm long and 10 nm in diameter (see Figure 3.11) were detected and characterised.

The samples in each case were diluted to a concentration at which less than one nanoparticle is expected to reside in the cavity mode at any time. This corresponds to a concentration of < 0.1 nM, assuming a mode volume of 10 μm^3. To reduce agglomeration of gold nanoparticles, it was recommended to maintain the concentration of surfactant when diluting the nanoparticle concentration. In the course of this work, problems due to the agglomeration of nanoparticles were not encountered.

After a nanoparticle measurement, the cavity was flushed with several millilitres of distilled and filtered water to prevent cross-contamination between samples.

[24] DNA 24HB from Prof. Tim Liedl's group at LMU Munich

Diffusion theory finds applications far beyond the nanoscopic realm; it also forms a basis for the analysis of the movement of animals. Pictured here are golden trout swimming with the current in the Eyach valley.

4. Single-nanoparticle sizing

As evidenced by the variety of techniques available today, measuring the size of nanoparticles is of much interest in many fields of research and industry. In contrast to ensemble-oriented techniques such as DLS and FCS, the approach outlined in this chapter demonstrates the capability to measure the size of single unlabelled nanoparticles in aqueous suspension.

We shall start with a description of data acquisition for single particle sensing. Since the analysis scheme presented herein is tested with simulations and applied to real measurements, simulated data generation and and experimental data acquisition are described, before we look at the actual evaluation pathway developed for particle size determination. Finally, the results of measurements with several nanosphere samples having diameters down to 3 nm are presented.

Parts of the results presented in this chapter have been published in ACS Nano [89].

4.1. Data acquisition for single particle sizing

Nanoparticles diffusing through the optical mode of the cavity induce a dispersive shift of the cavity resonance (Equation 2.29), which is recorded as a time-varying fluctuation $y(t)$ in the transmission of the locked cavity. Since the models and processes used to analyse data are newly developed in this work, it is worth verifying their accuracy independent of experiments. This was done by generating and analysing simulated data.

4.1.1. Diffusion simulations

To simulate nanoparticles diffusing in a microcavity, Monte-Carlo simulations were performed by modelling nanoparticles as punctiform diffusers with diffusivity D_T undergoing a random walk. From Section 2.4.1, we know that each step $\delta\mathbf{r}$ of Brownian motion is random and uncorrelated (Equation 2.34) and governed by the probability distribution given in Equation 2.39. Each component of a three-dimensional diffusion step is therefore generated by a random number generator drawing samples from a normal distribution $P(x) = 1/\sqrt{2\pi\sigma^2}\exp((x-\mu)^2/2\sigma^2)$ with $\mu = 0$ and variance $\sigma^2 = 2D_T\delta t$, where δt is the simulation time step. This yields a distribution identical to Equation 2.38. Additionally, reflecting boundary conditions were added to constrain the propagation in the z-direction to the length of the cavity. The position of the particle after the j^{th} step is then $\mathbf{r}_j = \mathbf{r}_{j-1} + \delta\mathbf{r}$.

Next, a standing wave intensity field (Equation 2.48) is constructed in the simulation volume and its value evaluated at every point on the simulated particle's path. Since we assume the measured signal to be proportional to the dispersive interaction of the particle with the optical field, and hence to the relative local intensity $|E(\mathbf{r_0})|^2$ at the particle's location via

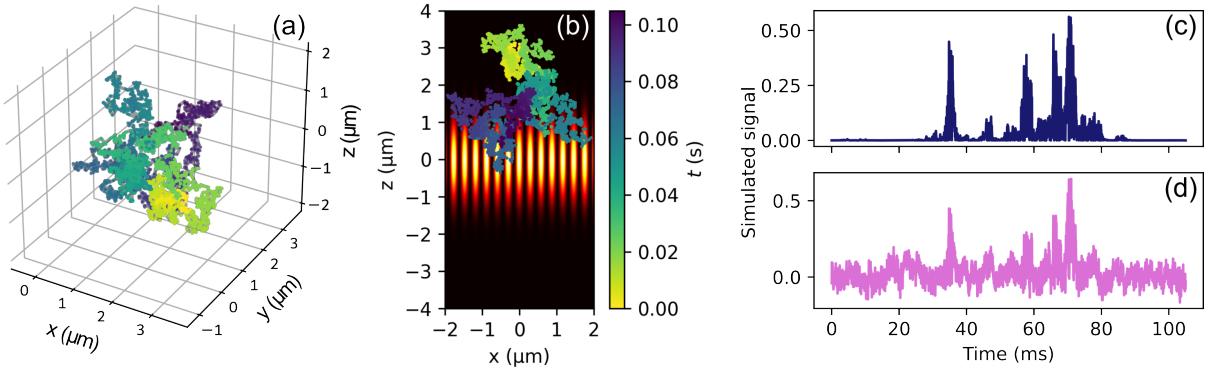

Figure 4.1: (a) Simulated three-dimensional Brownian diffusion of a particle with diameter 10 nm over 100 ms. (b) The particle path is shown superimposed over the optical field of a microcavity with length 4 µm. (c) The simulated particle signal generated by evaluating the field intensity at every point along the particle's path. (d) The same signal as in (c), with broken pink noise with $\sigma = 0.05$ added.

Equation 2.29, the value of (normalised) optical intensity along the particle's path is considered as the normalised nanoparticle signal. The generation of such a signal is illustrated in Figure 4.1. Simulated nanoparticle traces were thus computed for particle sizes of 3 nm, 5 nm, 10 nm, 15 nm and 20 nm, which correspond to the particle sizes available for measurement (Section 4.1.2).

Additionally, the effect of noise on the results of simulations was examined, in which "broken" pink noise, i.e. a combination of white noise (at low frequencies) and pink ($1/f$) noise (at high frequencies), with a relative RMS-amplitude of $\sigma = 0.05$ (peak amplitude $\approx 15\%$ of the maximum nanoparticle signal) was added to the clean simulated data before evaluation, see Figure 4.1 (d).

4.1.2. Experimental single-particle detection

Sample preparation. In order to measure nanoparticles, the cavity was filled with an isotonic buffer solution depending on the sample being measured, such as citrate or CTAB. The sample for investigation was prepared by diluting the stock nanoparticle suspension to a concentration of around 0.1 nM, which corresponds to one nanoparticle per mode volume ($\approx 10\ \mu m^3$). This was then injected into the cavity for single-particle detection. Gold nanospheres with nominal diameters of 3 nm, 5 nm, 10 nm, 15 nm and 20 nm were measured with the microcavity.

Nanoparticle detection. The cavity was operated in slowly locked mode as described in Section 3.1.2, and the cavity transmission trace of particle events were recorded and saved on a digital oscilloscope[1]. Particle traces were saved with sampling rates of 1 MS/s – 20 MS/s, and downsampled to 500 kS/s or 1 MS/s for processing, which is a sufficient rate to resolve the time scales of interest (milliseconds). Processing was done subsequently with a Python script on a computer. It may be mentioned here that integrating the evaluation scripts with data acquisition in the future will enable a faster, more streamlined and user-friendly approach to single nanoparticle sizing. For example, in a supervised Bachelors thesis, Hendrik Kööp

[1] Teledyne LeCroy WaveRunner HRO-64Zi

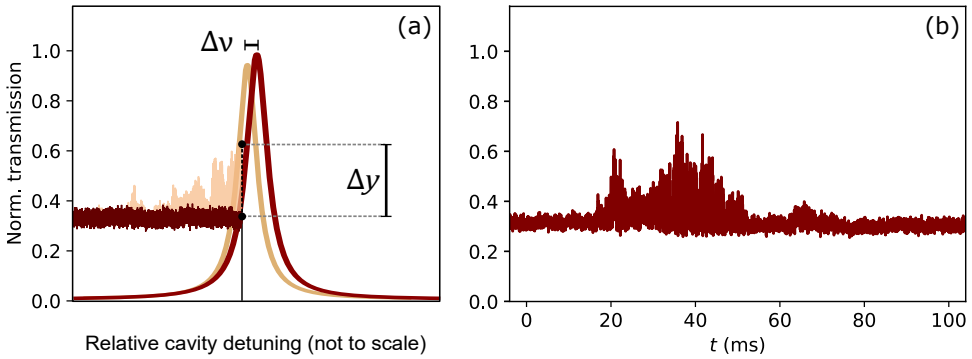

Figure 4.2: (a) The principle of cavity-locked detection: a small frequency shift $\Delta\nu$ of the cavity resonance leads to a large change in cavity transmission Δy. Note that the resonance curves are plotted as functions of cavity detuning from resonance, while the signals on the left show time-domain cavity transmission on a different temporal scale. (b) The transmission trace of a nanoparticle "event" featuring a single 20 nm gold nanosphere. [89].

developed such a system with an FPGA board for data acquisition and demonstrated the real-time measurement of nanosphere sizes [105].

The physical mechanism of cavity-locked nanoparticle detection is illustrated in Figure 4.2 (a): a small frequency shift $\Delta\nu$ of the cavity resonance leads to a large change in cavity transmission Δy at fixed cavity length. Figure 4.2 (b) shows an example of the resulting transmission trace during a nanoparticle event with a 20 nm nanosphere. Events with other particle sizes can be seen in the top panels of Figure 4.5 (a) – (e).

Verification of the "slow locking" regime. It was stated earlier that in cavity-locked mode, a "slow" lock is employed to stabilise the cavity. This means that the locking mechanism passes fast fluctuations, such as those due to nanoparticle diffusion, without attenuation, while correcting for slower perturbations and drifts in cavity length arising from acoustic, mechanical or thermal disturbances. Since the analysis of nanoparticle events presented here is dynamics-based, it is essential that the frequency regimes of cavity locking and particle diffusion are indeed separated.

This was experimentally verified using what we shall call "virtual particles".[2] The aim of this experiment was to compare the transmission fluctuation signal due to a particle-like perturbation ("virtual particle") in the cavity to the perturbation signal itself. For this purpose, the cavity was operated in locked mode as shown in Figure 3.3 (b), where one PZT is used for locking and the other for manual drift compensation with the AFG. Now, however, the DC output of the AFG is replaced by a simulated particle signal obtained as in Section 4.3.1. The cavity transmission $y(t)$ was measured with various lock parameters.

A central parameter affecting the bandwidth of the lock is the unity-gain frequency (UGF), and its influence is shown in Figure 4.3. At UGF = 80 Hz as used in this work, the virtual particle perturbation passes completely through to the cavity transmission (panel (a)), and the lock signal (e) remains unaffected. Also, the spectrum of the transmission signal (panel (i)) closely matches that of the original virtual particle, showing that full spectrum of nanoparticle dynamics is captured in $y(t)$. When the lock bandwidth is increased, the lock begins to

[2] The reader may be relieved to know that this term derives from the perturbation experienced by the cavity, and not from perturbations in quantum field theory.

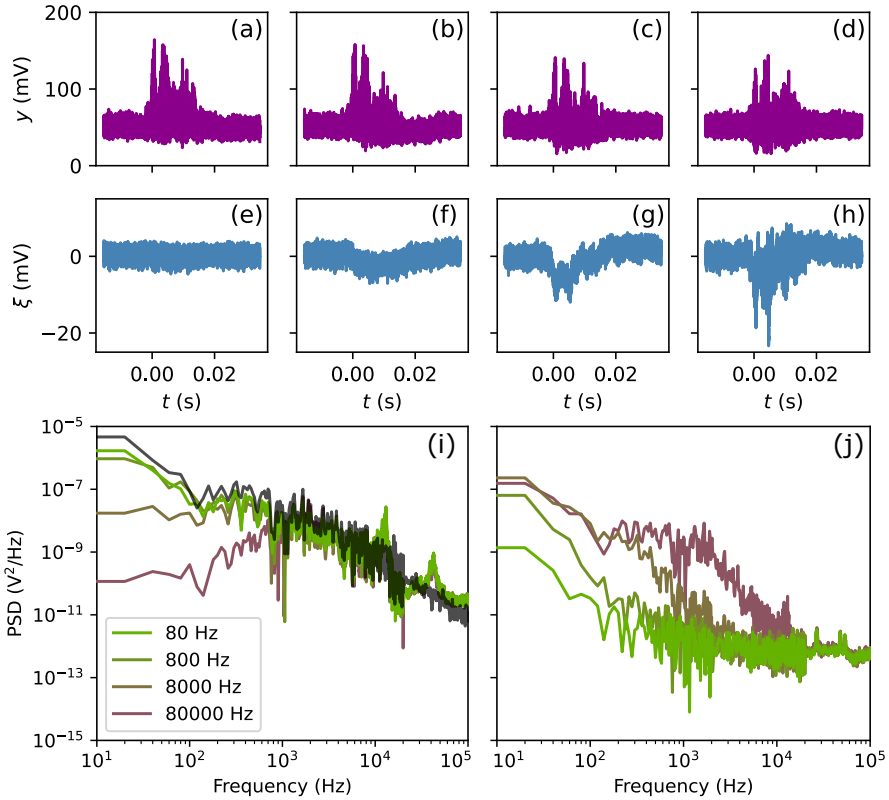

Figure 4.3: (a) – (d) Cavity transmission fluctuations $y(t)$ due to "virtual particle" disturbances in the cavity, measured with locking bandwidths (UGFs) of 80 Hz, 800 Hz, 8 kHz and 80 kHz respectively. (e) – (h) The lock feedback signal $\xi(t)$ under the corresponding lock conditions. (i) Power spectral density of $y(t)$, and of the original perturbation signal in black. (j) Power spectral density of $\xi(t)$ under the same lock conditions.

compensate for the virtual particle disturbance to varying degrees. In panels (d) and (h), for example, the transmission signal is significantly attenuated, and much of the dynamical information is transferred to the lock signal. In the frequency domain, we see that lower frequency components are missing in the spectrum of $y(t)$ (panel (i)), whereas the lock is much more active even over 10 kHz (j).

In conclusion, we can be confident that in the regime of a slow lock (UGF ~ 80 Hz), all nanoparticle dynamics are captured by the transmission signal and unattenuated by the lock.

4.2. Analysing single-particle events in a cavity

The size of a single nanoparticle is determined from its cavity transmission trace via its diffusion dynamics using autocorrelation-based analysis. While the autocorrelation is a well-established pathway for determining the size of diffusing nanoparticles (e.g. in DLS and FCS), the theories and models employed there cannot be directly applied to the Fabry-Perot single-particle sensor introduced in this work. For the development of a method to analyse single-particle measurements, we must first examine existing models and their differences from our microcavity setup. In Section 2.4.2, we saw that the framework of correlation analysis from

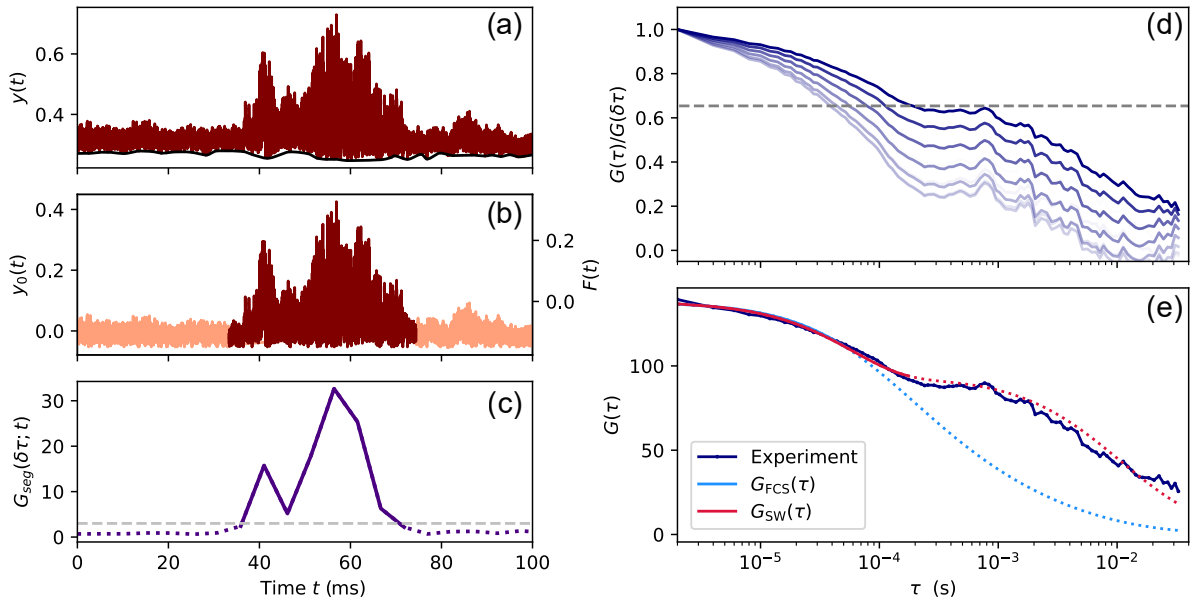

Figure 4.4: (a) Raw transmission trace of a nanosphere event with its lower envelope shown in black. (b) The de-enveloped trace $y_0(t)$ is plotted on the left axis, and becomes $F(t) = y_0(t) - Y_0$ after offset correction, plotted on the right axis. (c) The autocorrelation amplitude of trace segments $G_{\text{seg}}(\delta\tau; t)$ is used to separate the nanoparticle event from the background (shown dark and light respectively in (b)) based on a threshold value (dashed grey). (d) The normalised autocorrelation of $y_0(t) - Y$ is plotted with different values of Y. At offset Y_0 (plotted darkest), the plateau of the autocorrelation matches 0.653 times the correlation amplitude . (e) Fitting the autocorrelation: the fit to $G_{\text{FCS}}(\tau)$ is shown in blue and the fit to $G_{\text{SW}}(\tau)$ is shown in crimson. Only the solid parts are used for fitting.

FCS could be adapted to describe cavity-based detection, once certain differences are taken into account.

The first main difference between FCS and the microcavity sensor is the **field geometry**. Whereas FCS is performed in a confocal laser spot, the mode field in a Fabry-Perot optofluidic microcavity is a standing wave. Therefore, the new autocorrelation model derived in Section 2.4.2 and the resulting analytical ACF given in Equation 2.51 must be employed. Secondly, we must take the limited statistics and **transient nature** of a single nanoparticle event into account. In conventional FCS, measurements take place in a steady state, in which the average concentration of particles in the optical mode is assumed to be constant (Equation 2.43). This is clearly not the case in a single-particle experiment, where the cavity is mostly particle-free and the average particle concentration $\langle C \rangle$ even during a particle event varies between 0 and 1. This not only affects how we can define the "average" particle concentration, but also weakens the statistics at longer time scales, since the residence time of the particle in the cavity (about 40 ms from Figure 4.2 (b)) is not much longer than the time scales of interest for diffusion analysis.

With these considerations in mind, we are in a position to process the cavity transmission traces of single-nanoparticle events. The processing steps are outlined in the following, and shown graphically in Figure 4.4.

1. **Background removal.** In the first step, a slowly varying lower envelope (see Figure 4.4 (a)) is subtracted from the signal to remove (1) unwanted effects and offset of the slow cavity lock, (2) drifts and undulations in the signal. Additionally, frequency-domain filters are applied to eliminate frequency peaks (visible in Figure 3.4 (e)) due to electronic or mechanical noise. These are otherwise strongly manifested as oscillations in the

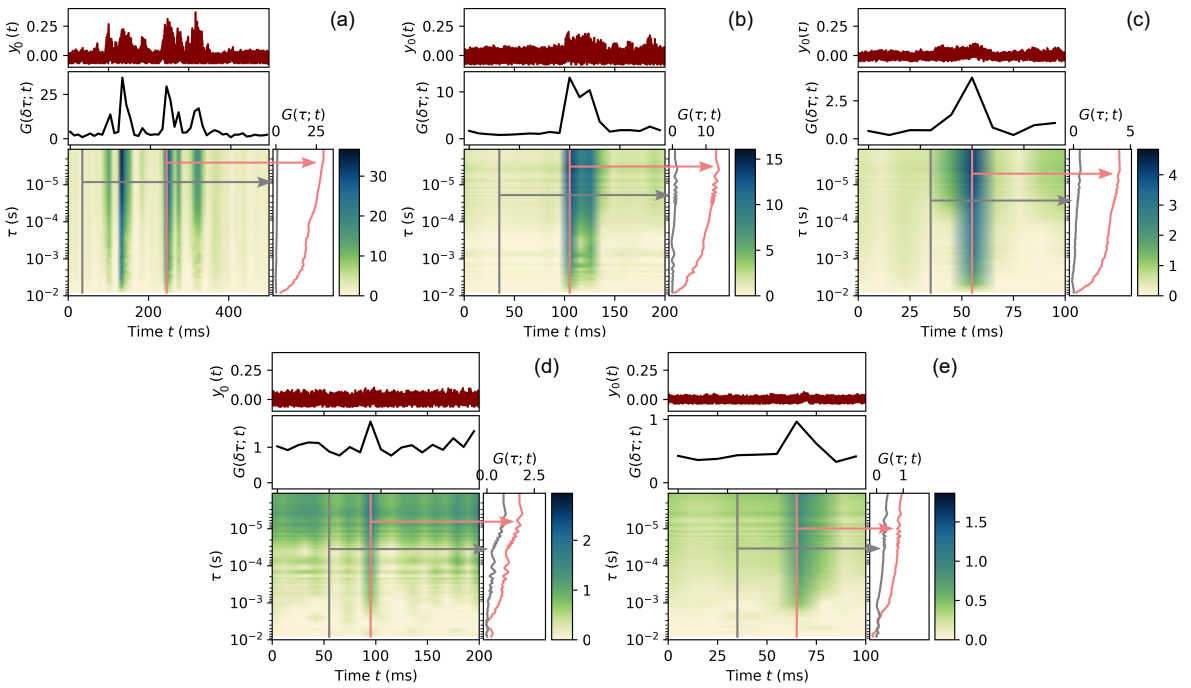

Figure 4.5: (a) – (e) Autocorrelograms of single particle events with particles having nominal diameters 20 nm, 15 nm, 10 nm, 5 nm and 3 nm. Note the shortening of the time axis for smaller particles.

autocorrelation. Finally, subtracting the mean "empty" cavity transmission results in a signal $y_0(t)$ which straddles zero (Figure 4.4 (b)).

2. **Event recognition.** This step is designed to automatically recognise regions including a particle event in a measured signal, and hence increase the level of automation of the single particle sensor. Particle events appear as fluctuations in the signal, as shown in Figure 4.2. Instead of thresholding the signal based on amplitude, which cannot distinguish a nanoparticle from a bump against the optical table, for example, the signal is segmented based on **autocorrelation-amplitude thresholding**. Here, the signal is sliced into segments with duration $T_{\text{seg}} \sim 10$ ms, and the autocorrelation of each segment is computed. This results in a two-dimensional **autocorrelogram** $G(\tau, t)$ where τ is the lag time and $t = j \cdot T_{\text{seg}}$ represents the temporal position of the j^{th} segment [32]. Autocorrelograms for several particle sizes are shown in Figure 4.5 (a) – (e). Correlated regions such as nanoparticle events are visible as vertical stripes, and the autocorrelations of segments displaying high and low correlations are compared in the panels on the right of each autocorrelogram.

   The autocorrelation amplitude $G(\delta\tau;\ t)$, i.e. the autocorrelation computed at the first time-lag step $\tau = \delta\tau$, was used to quantitatively identify correlated segments. This minimises the contribution of background white noise[3], which has a delta-distribution-like autocorrelation function, to our analysis. The temporal variation of $G(\delta\tau;\ t)$ is shown in the middle panels of Figure 4.5 (a) – (e) and in Figure 4.4

[3] The background (BG) is a mixture of white and pink ($1/f$) noise. It has a large value of $G(\tau = 0)|_{\text{BG}}$, but the magnitude of $G(\tau > 0)|_{\text{BG}}$ is much smaller and further decreases with τ.

(c), and can be thresholded above the value of the background correlation to identify nanoparticle events in a measurement.

This approach is particularly useful when dealing with the signals of small particles (diameter < 10 nm), which display a low SNR and cannot otherwise be readily distinguished from the background. Even for the smallest particles measured (3 nm), where $y_0(t)$ barely shows any variation from the background, one can identify a particle event around $t = 60$ ms in Figure 4.5 (e) via the autocorrelation amplitude with a SNR of about 2.

3. **Offset correction.** Now that the relevant sections of the trace have been identified, we wish to determine the diffusion time constants by fitting the autocorrelation to a known model. However, as stated above, the statistics of a single particle event differ unpredictably from the assumption of a stationary process used to derive $G_{\mathrm{SW}}(\tau)$ (Equation 2.51). In a stationary process, the autocorrelation of particle-driven fluctuations is calculated after subtracting the mean signal, corresponding to the mean particle concentration $\langle C \rangle$. On the other hand, in a single-particle event, the mean concentration is not well determined; instead $\langle C \rangle \in (0, 1)$. A key step in the analysis developed in this work is therefore compensating for this transient character, which makes the autocorrelation of $y_0(t)$ deviate from the ACF of a stationary event.

   In particular, we saw in Figure 2.5 (b) that $G_{\mathrm{SW}}(\tau)$ shows two decays separated by a point of minimum slope ("plateau"). Importantly, the value of $G_{\mathrm{SW}}(\tau)$ at this point is a function of cavity geometry only[4], and not of particle diffusivity (see Figure 2.5 (c) and (d)). Adding a global, constant offset (equivalent to a rectangular function) to a signal adds a linear decay to its autocorrelation (a decreasing ramp function with peak at $\tau = 0$). Therefore, the relative amplitude at the plateau in the autocorrelation of a nanoparticle event is sensitive to the global offset of the signal (see Figure 4.4 (d)), and it can be used as a reference level to determine the offset corresponding to the mean particle concentration $\langle C \rangle$. The value of the offset, Y_0, is numerically calculated such that the resulting autocorrelation has a plateau level coinciding with that of the analytical ACF (dashed line in see Figure 4.4 (d)). The resulting offset-corrected signal is $F(t) = y_0(t) - Y_0$, shown on the right axis of Figure 4.4 (b). It should be noted that since this level is not particle-dependent, it does not bias the value of particle size extracted in the next step.

4. **Autocorrelation and fitting.** $F(t)$ is autocorrelated using a multiple-tau algorithm [106] to yield the final experimental autocorrelation, $G(\tau)$, which was fit to the analytical functions $G_{\mathrm{FCS}}(\tau)$ or $G_{\mathrm{SW}}(\tau)$. The fit to $G_{\mathrm{FCS}}(\tau)$ is only valid for small lag times within the first decay, since it does not consider the standing wave geometry. The fit of the experimental autocorrelations to $G_{\mathrm{SW}}(\tau)$, on the other hand, is acceptable over the entire first decay, but at even longer lag times, the statistics worsen and the experimental autocorrelation may deviate from $G_{\mathrm{SW}}(\tau)$. This is due to the uniqueness of every nanoparticle transit, and features in the autocorrelation at long lag times can yield qualitative information about the individual nanoparticle event. Some examples of this are presented in Appendix B. The limit on data points to fit to the FCS model is (somewhat arbitrarily) determined by the point where its deviation from the standing-wave model exceeds 2%, which occurs at about 80% of $G(\delta\tau)$, and for the standing-wave model at the plateau separating the

[4] The relative plateau level is 0.653 for $w_0 = 1.3$ µm and varies by ≈ 0.002 per 0.1 µm change in the waist. It is assumed in this discussion that the probe wavelength, $\lambda_0 = 780$ nm, is fixed.

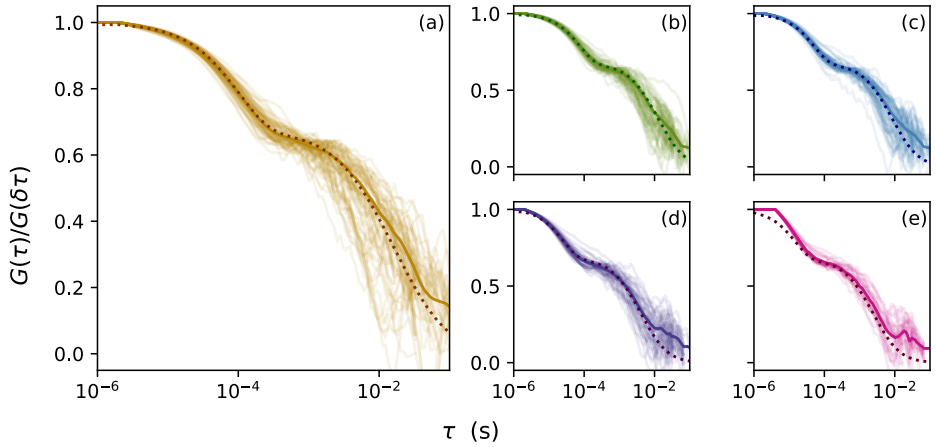

Figure 4.6: Autocorrelations of 100 simulated nanoparticle events with nanospheres of varying diameters: (a) 20 nm, (b) 15 nm, (c) 10 nm, (d) 5 nm, (e) 3 nm. In each panel, the averaged autocorrelation is plotted darker, and the analytical ACF using the nominal particle size is dotted.

two decays, which is 65% of the autocorrelation amplitude. In Figure 4.4 (e), the fit is performed over regions with solid curves as mentioned above, and the dotted curves are continuations of the respective ACFs.

4.3. Results of single nanoparticle sizing

Nanoparticle events simulated and measured as described in Sections 4.1.1 and 4.1.2 were evaluated via their autocorrelations according to Section 4.2. The results are presented in the following sections.

4.3.1. Particle sizing from simulations

The autocorrelations of all the simulated particles are shown in Figure 4.6, and the resulting size distributions extracted are shown in Figure 4.7. The histograms in panels (a) – (e) were generated from simulations with added broken pink noise (see Section 4.1.1) with relative root-mean-square amplitude $\sigma = 0.05$, and compare the two fitting models, $G_{\mathrm{FCS}}(\tau)$ and $G_{\mathrm{SW}}(\tau)$. The FCS model consistently overestimates particle size, most likely because it quickly deviates from the actual autocorrelation after a few tens of microseconds. The influence of noise on the analysis method can be seen by comparing panels (f) and (g) of Figure 4.7, which show the results without and with added noise, respectively. The difference here is minimal, and this robustness against noise is an important strength of autocorrelation analysis, even for weak signals buried in background noise.

While the results are accurate, they are not precise, as seen in the large spread of the histograms. Since the simulated data used for analysis are generated with "ideal" particles, this spread must be due to the statistical nature of this measurement method: individual particles interact with the optical field to varying degrees, and the corresponding events then also vary in their statistical strength.

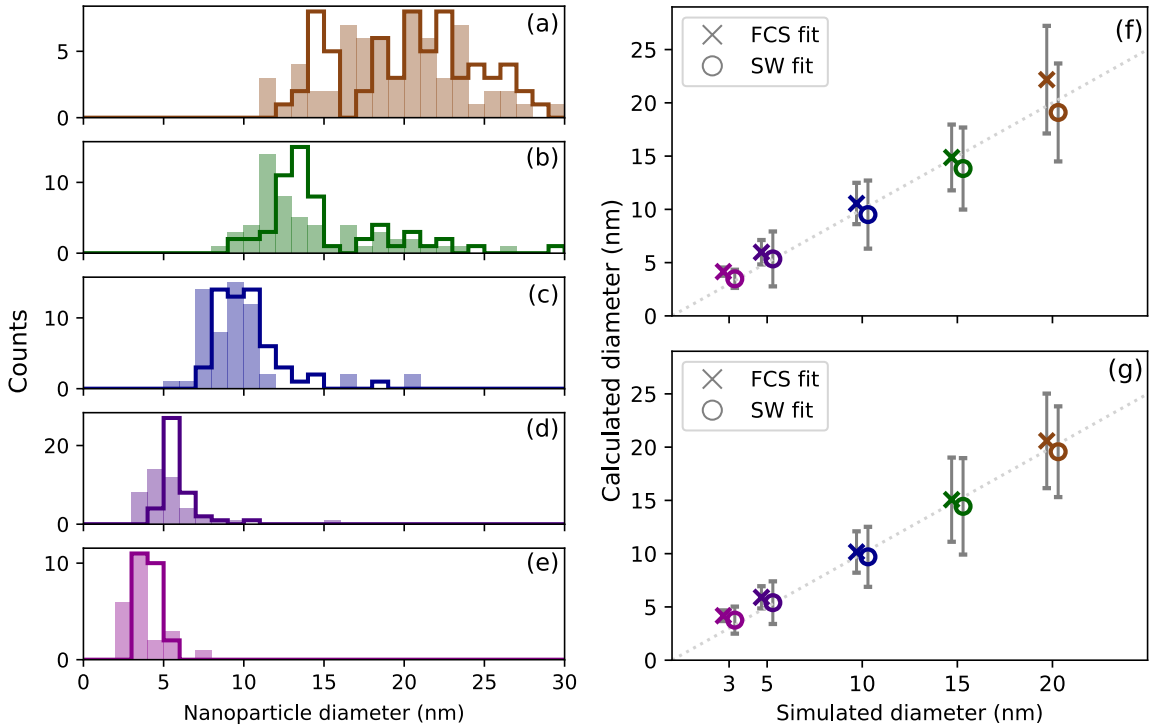

Figure 4.7: (a)–(e) Histograms of diameters calculated from simulations of nanoparticles with diameters 20 nm, 15 nm, 10 nm, 5 nm and 3 nm respectively. The unfilled histograms are generated with a fit to the FCS autocorrelation model, and the solid histograms with the standing wave model. (f), (g) A comparison of sizes calculated from "clean" simulated data and with added noise with $\sigma = 0.05$ respectively. Note that the data points of each sample are slightly horizontally shifted for visual clarity.

4.3.2. Experimental particle sizing

Several tens of single citrate-stabilised gold nanospheres were detected and measured, and their autocorrelations are shown in Figure 4.8. The resulting size distributions are shown in Figure 4.9 and summarised in Table 4.1. Our measurements yield sizes consistently smaller than specified for most samples investigated. This is confirmed by both the DLS and TEM measurements (see below), showing that the measurement technique presented here is already able to detect size deviations of a few nanometres from a specified size. The width of the size distributions is in part due to the actual polydispersity of the gold nanoparticles, which is also reflected in the size distribution curves from DLS and TEM measurements, and in part due to the transient and stochastic nature of each event as seen in the simulated results in Section 4.3.1 [32].

Peculiarly, the spread of the results from experimental data are *smaller* than of those from the simulations shown in Section 4.3.1. A possible reason for this could be selection bias when recording particle events in experiments, which tends to favour particles with better statistics (e.g. long event durations and high signal amplitude).

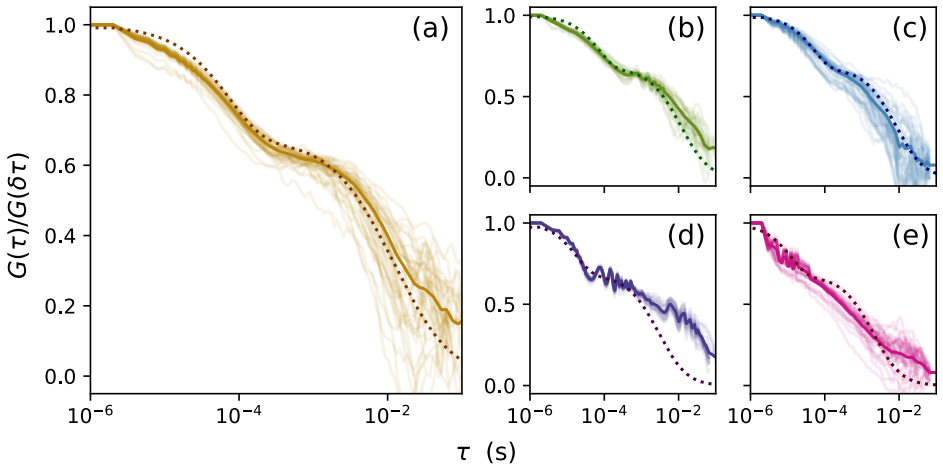

Figure 4.8: Autocorrelations of several individual nanoparticle events with nanospheres of varying diameters: (a) 20 nm, (b) 15 nm, (c) 10 nm, (d) 5 nm, (e) 3 nm. In each panel, the averaged autocorrelation is plotted darker, and the analytical ACF using measured parameters from Table 4.1 is dotted.

Comparison measurements. To verify the accuracy of these measurements, the nanospheres were also measured using established methods, namely DLS[5] and TEM[6] (10 nm and 20 nm only, see Appendix A), at the Institute of Inorganic Chemistry (AOC) at KIT by Christian Ritschel and Jens Treptow.

The size distributions from DLS are shown as dashed curves in Figure 4.7 (a)–(e). One should note an intrinsic ambiguity which arises in DLS measurements, due to the scattered intensity of a particle being proportional to R^6. This means that the intensity-weighted distributions directly measured from a nanoparticle ensemble are vulnerable to distortion by larger particles or agglomerates existing in the sample. Therefore, **number-weighted** distributions are shown here, which offer a more meaning comparison in the context of this work, but are indirectly obtained from the intensity-weighted data by inversion calculations using Mie theory [21]. They are therefore dependent on provided data about the nanoparticles and vulnerable to errors in calculation.

We may also note that in contrast to DLS measurements, measurement with the microcavity required only microscopic sample volumes of a few hundred microlitres with ultra-low concentrations up to 10^4 times lower than that required for DLS [107], making it an attractive technique when characterisation of a small sample is desired.

Further details about DLS and TEM measurements are given in Appendix A.

The effect of adsorbed ligands. Citrate-stabilised particles have been investigated so far, and due to the small size of the citrate molecule, the measured hydrodynamic diameter is close to the specified and measured "dry" diameter from TEM images [108]. In general, however, it is expected that different surfactants interact with the surrounding medium differently, and may lead to a hydrodynamic diameter differing from the "dry" diameter by many tens of nanometres.

[5] Malvern Instruments ZetaSizer Nano ZS
[6] FEI Osiris

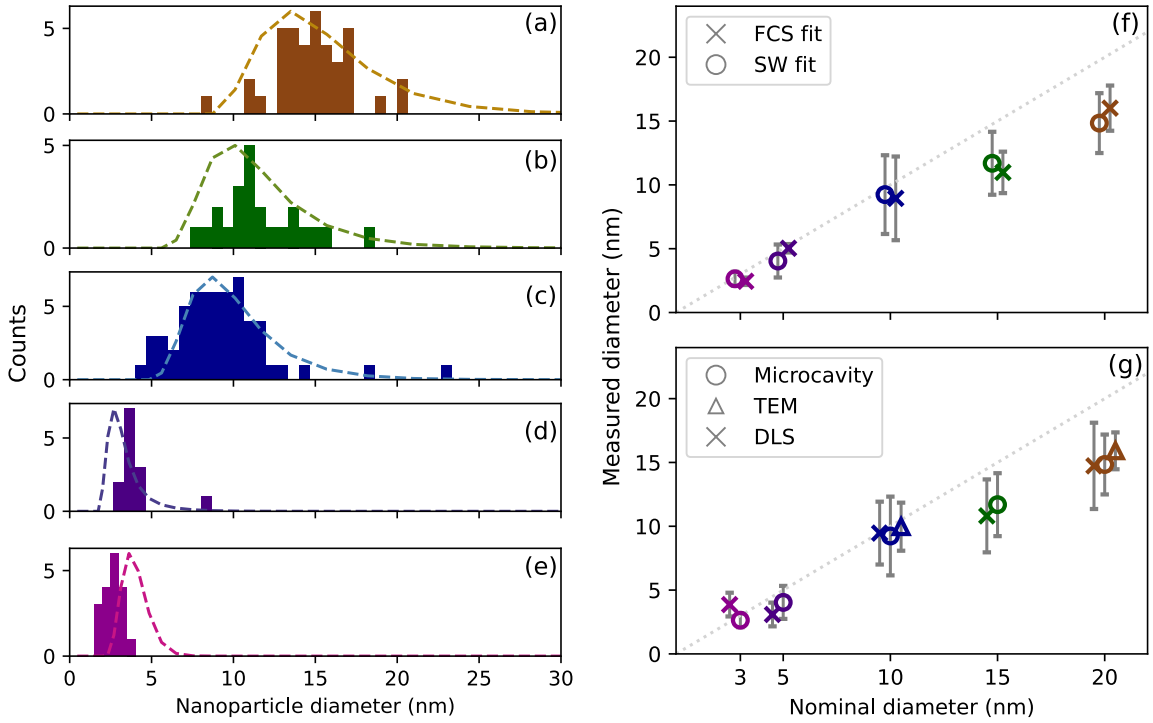

Figure 4.9: (a)–(e) Histograms of nanoparticle diameters individually measured with the microcavity from samples with nominal diameters 3 nm, 5 nm, 10 nm, 15 nm and 20 nm respectively. The dashed curves show DLS measurements. (f) A comparison of sizes calculated from the two autocorrelation models used. (g) A comparison of sizes measured with the microcavity (SW model), DLS and TEM. The measured sizes would lie on the grey dotted line if they were equal to the specified diameters. Note that the data points of each sample are slightly horizontally shifted for visual clarity. [89].

Sample no.	Specified diameter (nm)	Measured diameter (nm) with microcavity	by DLS	by TEM
1	3	2.6 ± 0.5	3.8 ± 0.8	-
2	5	4.0 ± 1.3	3.1 ± 0.9	-
3	10	9 ± 3	9.5 ± 2.5	10 ± 2
4	15	12 ± 2	11 ± 3	-
5	20	15 ± 2	15 ± 3	15.9 ± 1.4

Table 4.1: A comparison of nanosphere diameters measured using our microcavity, with a commercial DLS system and TEM microscopy. The DLS results are number-normalised. The microcavity results represent statistics from N = 15, 18, 53, 22 and 37 single particle measurements for sample numbers 1, 2, 3, 4 and 5 respectively. The TEM measurements were done from images containing N = 34 and 20 particles respectively.

As a comparative study, 20 nm nanospheres in CTAB were measured as well. The diameter measured with the microcavity in this case was (87 ± 34) nm, and via DLS (73 ± 30) nm, clearly showing that the adsorbed ligand can drastically affect hydrodynamic size. Interestingly, this size difference is much larger than the extent of the expected CTAB bilayer, suggesting either the formation of a larger ligand structure around the nanoparticles, or a strong interaction with the surrounding medium, leading to the formation of a larger hydrate shell [47]. CTAB is known to form micelles[7] at the concentrations present in our samples, which could further interact

[7] At low temperatures, e.g. during refrigeration, CTAB has even been observed to form crystals, which disappear at room temperature.

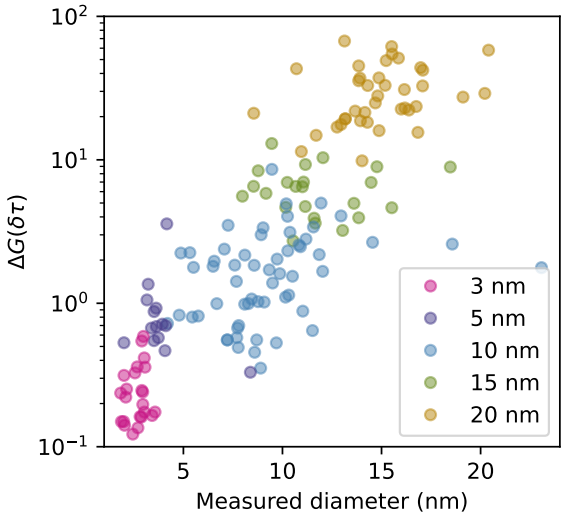

Figure 4.10: A scatter plot of individual particle measurements showing the dependence of autocorrelation contrast $\Delta G(\delta t) = G(\delta\tau)|_{\mathrm{NP}} - G(\delta\tau)|_{\mathrm{BG}}$ between the event and the background on the particle size.

with the gold nanoparticles and influence their dynamical behaviour. Finally, it may be noted that the gold nanospheres were synthesized in citrate solution [100], and the subsequent ligand substitution with CTAB may have altered the hydrodynamic behaviour of nanoparticles.

4.3.3. Detection limits

In the preceding sections, the detection of nanoparticles down to 3 nm in diameter was demonstrated. This already corresponds to a sphere about 20 gold atoms in diameter, and to a molecular weight of 160 kDa, putting our detection capabilities on the single molecule level. An interesting question, now, is how much more sensitive we can get.

One major advantage of autocorrelation as an analysis tool is its ability to extract weak correlated signals buried in background noise, as seen in the comparison between Figures 4.7 (f) and (g). This was leveraged for particle events with a low SNR ~ 1 in the transmission trace using the autocorrelation amplitude to filter out nanoparticle events and their dynamics from background noise, effectively doubling the SNR in autocorrelation amplitude. To estimate a lower limit of the correlation which can be extracted from signals with a given background noise, one can investigate how the **autocorrelation amplitude contrast** between the correlation of a nanoparticle event and the background, $\Delta G(\delta t) = G(\delta\tau)|_{\mathrm{NP}} - G(\delta\tau)|_{\mathrm{BG}}$, varies with measured particle size. (Comparing the *contrast* instead of the absolute value of $G(\delta t)|_{\mathrm{NP}}$ during an event compensates for different background correlation levels among different measurements, which ranged between 0.5 and 1.0 for 10 ms segments.) Figure 4.10 shows that the autocorrelation amplitude of some 3 nm particle events already comes close to the background level, and has a correlation-SNR of about 2.

To reduce this detection limit, one would need to further improve the stability to reduce the background correlation level. However, we eventually face fundamental limits imposed by unavoidable shot noise and electronic noise. For instance, the typical detector noise from an APD already contributes ~ 100 fm to the cavity instability [57].

4.3.4. Conclusion

In this chapter, a technique for the sizing of individual nanospheres in aqueous suspension was introduced which uses a microcavity, a new autocorrelation model describing particle diffusion in a microcavity, and an analysis pathway designed to take into account the transient nature of single particle events. The precision of this method is fundamentally limited by its stochastic nature, but multiple measurements of single nanoparticles yield statistics which agree excellently with other state-of-the-art methods.

Furthermore, the influence of the stabilising ligand on hydrodynamic particle size was briefly investigated by comparing measurements with citrate- and CTAB-stabilised nanoparticles.

The microcavity sensor enabled the detection and measurement of single particles down to 3 nm in diameter, which already approaches the regime of single-molecule measurements. The sensitivity of our sensor in its current form is limited by the background correlation level, which limits the analysis of the dynamics of smaller nanoparticles even by autocorrelation, a signal processing method capable of strong noise rejection.

Robert Brown observed the diffusive motion of pollen grains of several species, such as the *Oenothera*, pictured here, in 1827. He noticed variations in the shapes of the particles: some were spherical, whereas others were rod-like and exhibited rotational motion as well.

5. The rotation of anisotropic particles

The measurement and analysis techniques presented in Chapter 4 enabled us to measure the size of individual nanospheres via their diffusive motion in an optical cavity. This analysis, however, limits us to the measurement of spherical particles. In reality, nanosystems of interest are seldom spherical, and it would be a significant development to be able to measure the dimensions of non-spherical (anisotropic) particles as well. An anisotropic nanoparticle geometry which has been studied in various fields and by various methods is the **nanorod**, which well approximates a number of species of interest, from rod-like bacteria and viruses to proteins and nanotubes [33, 109]. Nanorods are characterised by their length (L) and diameter (d), and the determination of these two quantities requires the measurement of an additional degree of freedom: rotation. And since nanoparticle rotation occurs on the microsecond scale, orders of magnitude faster than diffusion, the high-bandwidth measurement capabilities of the locked microcavity sensor are used to their full advantage here.

The rotation dynamics of nanorods can be seen in the cavity transmission signal, $y(t)$, measured as described in Chapter 4. We shall examine the dynamics of nanorods in Sections 5.1 and 5.2, and then discuss an approach to observe rotation not only temporally, but also spatially, in Section 5.3.

5.1. Capturing the rotation dynamics of nanorods

Gold nanorods of three sizes were detected with the microcavity. The nanorod samples studied are hereinafter referred to by their plasmon resonance wavelengths: 600 nm (20 nm × 10 nm), 650 nm (25 nm × 10 nm) and 700 nm (15 nm × 5 nm). As in Chapter 4, we would like to compare experimental measurements and their analysis to simulations, and so we shall begin by discussing the simulation of rotational motion of anisotropic particles.

5.1.1. Simulation of rotating particles

Monte-Carlo simulations were performed to simulate the rotational diffusion of an anisotropic nanoparticle. As explained in Section 2.4.3, the orientation vector $\hat{\mathbf{u}}$ of the nanorod undergoes a quasi-two-dimensional random walk on a unit sphere. The direction of $\hat{\mathbf{u}}$ is defined by the polar and azimuthal angles θ and ϕ.

Each component of a three-dimensional rotational diffusion step is therefore generated by a random number generator drawing two samples ($\delta\theta$, $\delta\phi$), corresponding to angular shifts in the

polar and azimuthal directions[1], from a normal distribution $P(x) = 1/\sqrt{2\pi\sigma^2}\exp((x-\mu)^2/2\sigma^2)$ with $\mu = 0$ and variance $\sigma^2 = 2D_R\delta t$. This is equivalent to Equation 2.55. The position of the orientation vector on the unit sphere after the j^{th} step is then given by the new angles $\theta_j = \theta_{j-1} + \delta\theta$ and $\phi_j = \phi_{j-1} + \delta\phi$. An exemplary three-dimensional trajectory of $\hat{\mathbf{u}}$ is shown in Figure 5.1 (a).

We saw in Section 2.3.2 that nanorods possess an anisotropic polarisability. Equation 2.27 gives the polarisation of a general anisotropic particle along each axis, which for a nanorod is reduced to two quantities, α_L and α_S, along the long and short axes respectively. When a nanorod is placed in a linearly polarised optical field, the magnitude of its interactions with the field (e.g. dispersion, given by Equation 2.29) are then dependent on the nanorod orientation relative to the field polarisation. Since $\alpha_L \gg \alpha_S$ for the nanorods used here, interactions due to the polarisability along the long nanorod axis dominate and the short axis is neglected henceforth[2] [33, 109].

Then, assuming (without any loss of generality) the cavity field to be polarised along the x-axis, the magnitude of the resonance shift due to dispersion by a nanorod, and hence the cavity transmission signal, is proportional to the projection of α_L onto the x-axis,

$$s_{\text{rot}}(t) \propto \cos^2(\phi)\sin^2(\theta), \tag{5.1}$$

where θ and ϕ define the orientation of the long nanorod axis as before.

Since rotational and translational diffusion are considered independent of each other, the diffusional motion of the nanoparticle is independently simulated as described in Section 4.1.1. The total simulated signal is then the product of fast rotation fluctuations and a translational diffusion envelope, and is shown in Figure 5.1 (b) and (c).

5.1.2. Detection of rotational diffusion

Experiments with nanorods were performed in an identical fashion to those presented in Chapter 4, but data were recorded at a higher bandwidth (20 MHz – 100 MHz) to allow the fast rotational dynamics to be temporally well resolved. In addition, to ensure the detection of the projection of the nanorod's orientation onto a single axis, polarisation filtering was done at the output of the cavity, involving two waveplates and a polarising beam-splitter (PBS). This is described in more detail in the context of rotational tracking in Section 5.3.1 and shown in Figure 5.7 (c)[3].

Examples of nanorod traces are presented in Figure 5.2. For the nanorod events shown in panels (a), (c) and (e), fast signal fluctuations due to rotational diffusion can be seen in the zoomed traces in panels (b), (d) and (f) respectively. Interestingly, the signal amplitude of nanorods in

[1] To avoid ambiguity in the azimuthal angle near the poles of the unit sphere, one can assume each step to start in a local frame of reference where $\hat{\mathbf{u}}$ lies on the equator. Then small changes in θ and ϕ are orthogonal and linear and lie on a nearly planar surface.

[2] Aspect ratios around 2.5 give $\alpha_L \approx 5 \cdot \alpha_S$ for gold nanorods. This ratio increases towards aspect ratio 4, where small gold nanorods have a plasmon resonance at $\lambda_0 = 780$ nm. The large contrast between α_L and α_S is due to the metallic nature of the nanorods, namely $\varepsilon(\omega) < 0$ in Equation 2.27.

[3] At this stage, we only investigate one polarisation eigenmode, and APD_V shown in Figure 5.7 (c) is unused.

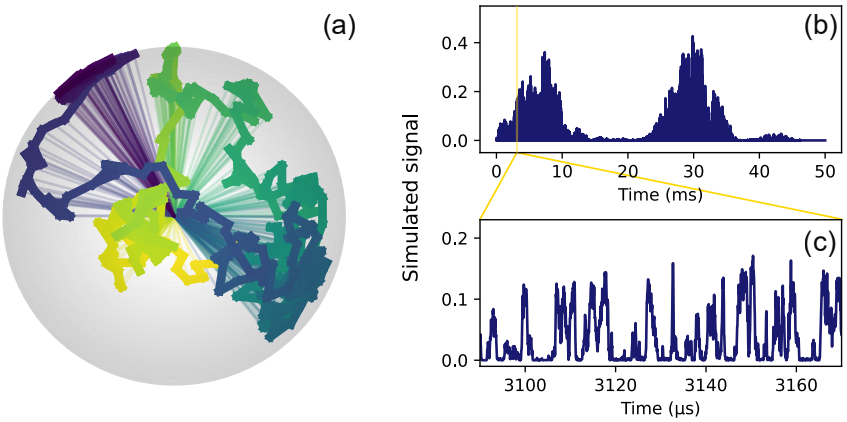

Figure 5.1: (a) Simulated three-dimensional orientation of a rotationally diffusing nanoparticle with $D_R = 1.52 \times 10^5$ rad^2 s^{-1}, corresponding to a 25 nm × 10 nm nanorod, shown as a random walk of $\hat{\mathbf{u}}$ on a unit sphere. The simulation time resolution was 20 ns. For clarity, only 10 µs of the simulation are shown. (b) The simulated trace of a diffusing nanorod is a combination of its rotational and translational motion. (c) On short timescales (here: about 70 µs), pure rotation is visible under the relatively slow diffusion envelope.

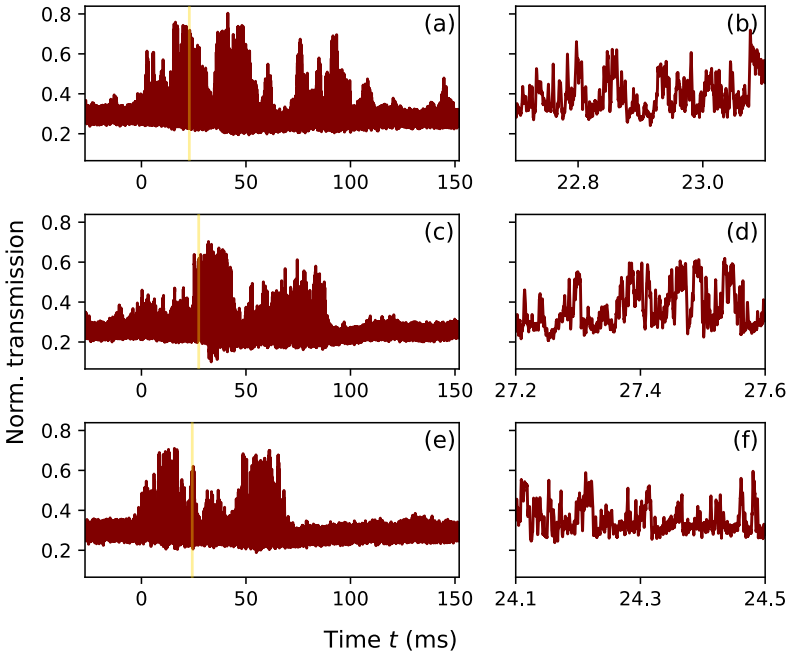

Figure 5.2: (a), (c), (e) Traces from nanorod events with nanorod samples "650", "600" and "700" respectively, in citrate buffer. (b), (d), (f) Zoomed views of (a), (c) and (e) respectively, showing fast fluctuations due to rotation over a duration of 400 µs.

sample "700" were comparable in size to those of sample "650", despite a seven-fold smaller particle volume of the former. This may be caused by an enhancement of the interaction of the nanorod with the cavity mode due to the proximity of its plasmon resonance (≈ 700 nm)[4] to the probe laser (780 nm).

[4] While the nominal plasmon resonance is at 700 nm, the manufacturer specifies a tolerance of up to 725 nm, which approaches the probe wavelength used here. Further heterogeneity in the nanorod shape could bring the actual resonance wavelength even closer to the probe laser, see Section 5.2.2 and Appendix A.

5.2. Sizing of single nanorods

It would be useful and interesting indeed to extend the approach developed in Chapter 4 to measure the size of single nanorods as well. Here, we shall once again use autocorrelation to quantitatively analyse the cavity transmission signal of single nanorods using the ACFs given in Equation 2.56 and Equation 2.51. Since in most cases, the rotational and translational time constants are separated by several orders of magnitude ($\sim 10^{-6}$ s and $\sim 10^{-4}$ s respectively), the rotation and diffusion decays can be fit separately with their respective ACFs. The autocorrelation must therefore be divided at the point between the first (rotational diffusion) decay and the first translational diffusion decay, and both parts analysed separately.

The evaluation steps to determine D_T are similar to those outlined in Section 4.2. Here, only the section of the autocorrelation corresponding to diffusion (i.e. after the first decay, shown in red in Figure 5.5 (b)) is analysed. In particular, only the amplitude of the translational diffusion component of the autocorrelation must be considered when computing the offset Y_0. Then $G_{\mathrm{SW}}(\tau)$ can be fit to the diffusion part, yielding the diffusion coefficient D_T.

The rotational diffusion coefficient D_R was determined from the rotation decay using Equation 2.56. The additional parameter r in Equation 2.56 describes the amplitude of the rotation decay, and was constrained to ensure continuity of the rotational part with the translational ACF already fit as described above. An explicit connection of r with the cavity or nanoparticle geometry has not been determined. Thanks to the high measurement bandwidth of the sensor, the rotational dynamics can be temporally well resolved, and detector-limited[5] measurement speeds of up to 100 MHz (= time resolution of 10 ns) have been demonstrated in this work.

We now have two known coefficients, D_T and D_R, and wish to determine the length and diameter of the nanorod. This was done using the approach of Tirado and de la Torre [84] as follows. Using their expressions for the translational and rotational diffusion coefficients, the equation

$$\left(\frac{9\pi\eta}{k_B T}\right)^{2/3} \frac{D_T}{D_R^{1/3}} = \frac{\ln(p) + \nu(p)}{(\ln(p) + \delta(p))^{1/3}} \tag{5.2}$$

is solved for the nanorod aspect ratio $p = L/d$. Inserting this into Equation 2.41 yields the length of the nanorod, and the diameter is then simply $d = L/p$. An example of the autocorrelation of a measured single nanorod event is given in Figure 5.5 and of simulated nanorods in Figure 5.3, and the aforementioned three distinct decays are apparent. Fitting the first one to $G_{\mathrm{rot}}(\tau)$ and the second one to $G_{\mathrm{SW}}(\tau)$ allow the determination of D_R and D_T, and thus L and d. The translational diffusion coefficient can be used to calculate an effective hydrodynamic diameter of the nanorod, d_{hydr}, corresponding to the size of a sphere with the same translational diffusion behaviour as the nanorod.

[5] The APDs used had a 3 dB bandwidth of 50 MHz.

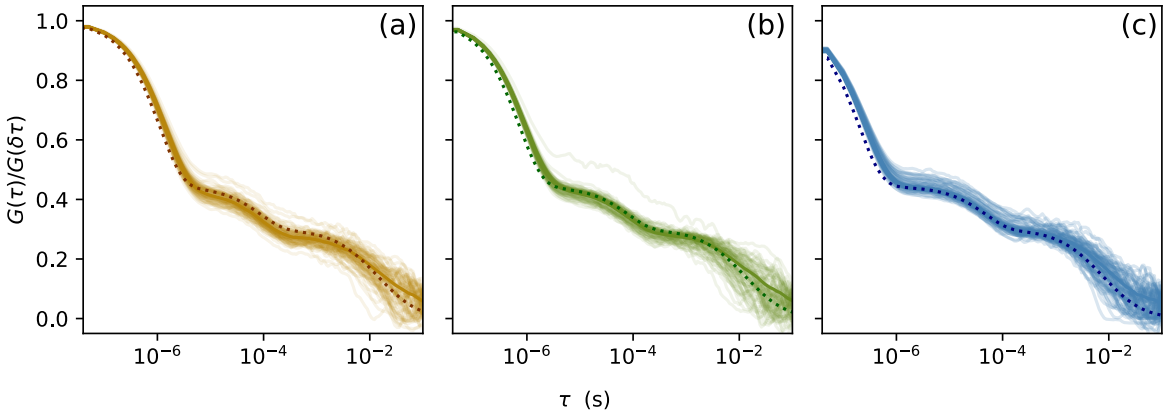

Figure 5.3: Normalised autocorrelations of 100 simulated nanoparticle events with nanorods with sizes corresponding to samples "650" (a), "600" (b) and "700' (c). In each panel, the averaged autocorrelation is plotted darker, and the analytical ACF using the nominal particle size is dotted. The sample size is $N = 100$ for each nanorod size.

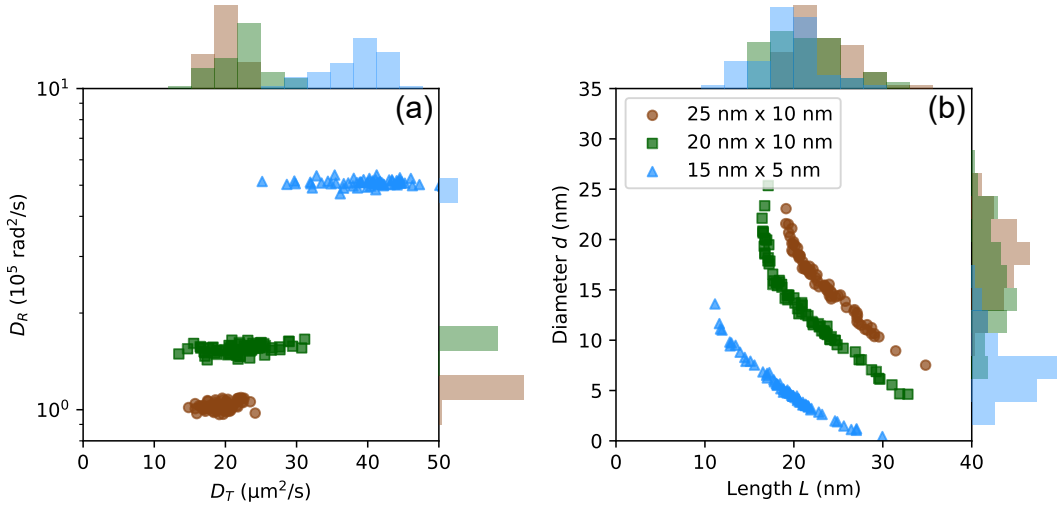

Figure 5.4: (a) The distribution of diffusion and rotational diffusion coefficients of simulated nanorods with sizes corresponding to samples "650" (brown circles), "600" (olive squares) and "700" (blue triangles). (b) The lengths and diameters of the nanorods, determined from the coefficients in (a). The histograms show the distributions of the quantity on the respective axis.

5.2.1. Nanorod sizing results from simulations

Simulated nanorod events were evaluated as described above. The autocorrelations of several simulations with different nanorod dimensions corresponding to the samples available are shown in Figure 5.3, and fitting these to $G_{\mathrm{rot}}(\tau)$ and $G_{\mathrm{SW}}(\tau)$ yielded their diffusion coefficients, D_R and D_T, shown in Figure 5.4 (a) and in Table 5.1.

Surprisingly, while the resulting rotational diffusion coefficients were precise, they showed a systematic error, tending to be 30% lower than expected for all nanorod sizes simulated. This lies beyond the uncertainty limits imposed by the statistical nature of the evaluation, and suggests that the evaluation model employed may not fully account for the actual simulation

Sample		D_R (10^5 rad^{2}s^{-1})	D_T (μm^{2}s^{-1})	L (nm)	d (nm)	d_{hydr} (nm)
650	Simulation	(1.03 ± 0.03)	(19.3 ± 1.9)	(24 ± 3)	(15 ± 3)	(22.4 ± 2.4)
	Theory	1.51	24.7	25	10	17.4
600	Simulation	(1.55 ± 0.05)	(22 ± 3)	(21 ± 4)	(14 ± 4)	(19.9 ± 3.6)
	Theory	2.30	27.1	20	10	15.8
700	Simulation	(5.09 ± 0.11)	(41 ± 7)	(19 ± 4)	(5.2 ± 2.6)	(10.7 ± 1.8)
	Theory	8.43	45.4	15	5	9.4

Table 5.1: A comparison of calculated and theoretically expected results from simulations with single nanorods. The sample size is $N = 100$ for each nanorod size.

setting. Whereas the autocorrelation function used here considers tumbling in all directions, we may note that the linearly polarised cavity field is insensitive to rotation components around the polarisation axis, which could lead to an underestimation of D_R. In other studies, the exponent $6D_R\tau$ in $G_{\text{rot}}(\tau)$ has been modified to account for such an effect [109, 110], and, while a theoretical derivation has not yet been undertaken here, such a correction could allow a more accurate determination of the rotational diffusion coefficient here as well.

Due to the non-linear cross-dependences of L and d on D_T and D_R from Equations 2.41 and 2.57, in particular the strong $1/L^3$ dependence of D_R on nanorod length, the relatively compact and well-separated distributions in Figure 5.4 (a) translate into diagonal bands in (L, d) space (panel (b)). As a result, the determination of the diffusion coefficients of a nanorod by the method shown here is a more precise and well-defined statement than the estimation of its length and diameter. The hydrodynamic diameters calculated from D_T have a relative uncertainty of up to 18%, which is comparable to that seen for spheres in Chapter 4.

5.2.2. Experimental nanorod sizing results

Now we shall turn to measurements with real nanorods. The quantitative results from several nanorod measurements are shown in Figure 5.6 and summarised in Table 5.2.

Sample		D_R (10^5 rad^{2}s^{-1})	D_T (μm^{2}s^{-1})	L (nm)	d (nm)	d_{hydr} (nm)
650	Expt.	(0.63 ± 0.13)	(19 ± 5)	(36 ± 11)	(13 ± 9)	(24 ± 8)
	Theory	1.51	24.7	25	10	17.4
600	Expt.	(0.26 ± 0.03)	(10 ± 2)	(34 ± 6)	(30 ± 8)	(40 ± 7)
	Theory	2.30	27.1	20	10	15.8
700	Expt.	(0.9 ± 0.3)	(21 ± 7)	(31 ± 9)	(13 ± 7)	(22 ± 6)
	Theory	8.43	45.4	15	5	9.4

Table 5.2: A comparison of measured and theoretically expected results from experiments with single nanorods. The sample sizes are $N = 30, 9$ and 15 for samples "650", "600" and "700" respectively.

Discussion of results. We see two types of unexpected behaviour from the measurements shown in Figure 5.6. One is a systematically smaller rotational diffusion coefficient than theoretically expected for all three samples. The second arises when comparing the diffusive behaviour between the samples: the order of specified sizes of the nanorods is not reflected in the measured results.

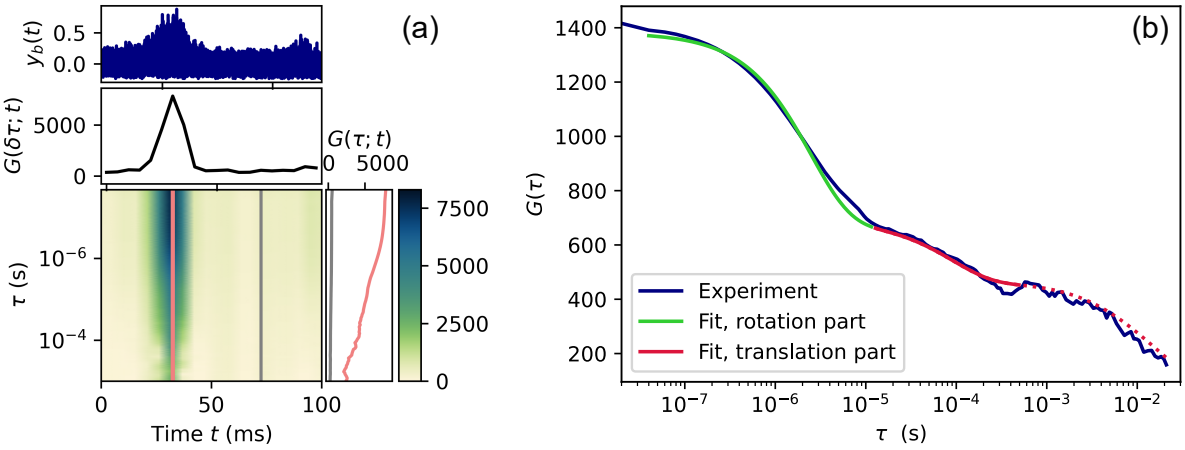

Figure 5.5: (a) The autocorrelogram of a 25 nm × 10 nm nanorod event. Due to the high correlation of rotation dynamics, the SNR in autocorrelation amplitude is about 15, whereas that in the actual signal is only about 2. (b) The autocorrelation of a 25 nm × 10 nm nanorod event. The parts of the fit function, $G(\tau) = G_{\mathrm{rot}}(\tau) \cdot G_{\mathrm{SW}}(\tau)$, corresponding to rotational and translational diffusion are shown in green and crimson repsectively. Fitting is done over the solid sections of the curves.

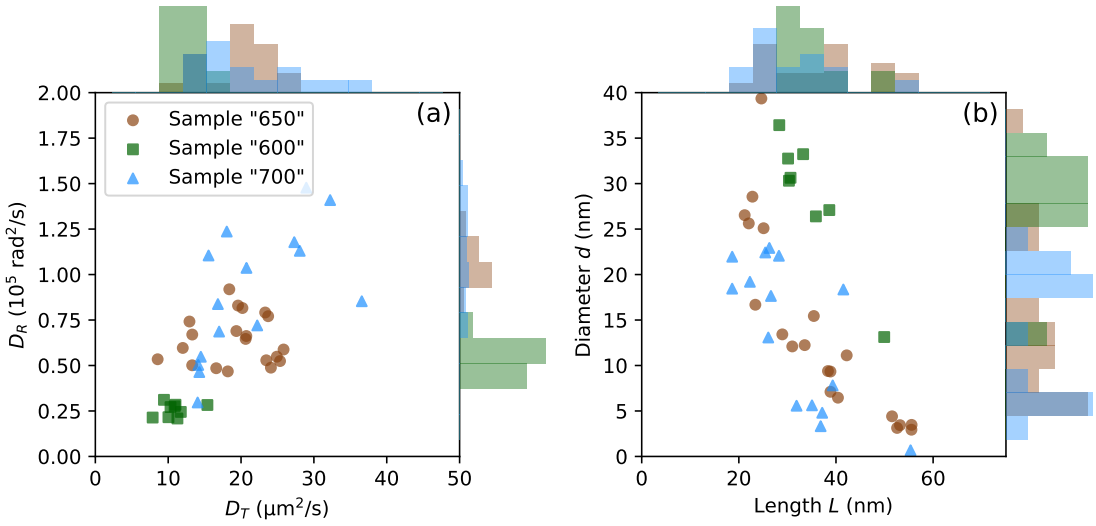

Figure 5.6: (a) The distribution of diffusion and rotational diffusion coefficients of CTAB-stabilised nanorods with nominal size 25 nm × 10 nm (brown circles) and 20 nm × 10 nm (olive squares). (b) The lengths and diameters of the nanorods, determined from the coefficients in (a). The histograms show the distributions of the quantity on the respective axis.

The first effect suggests experimental effects in our measurements or theoretical effects in the analysis which have not been taken into account in the evaluation model. We observed an underestimation of D_R from simulated data in Section 5.2.1, and believe that this discrepancy plays a similar role with measured data here. Furthermore, a hydrodynamic shell due to the surfactant or other interactions with surfactant molecules, which were not taken into account while calculating D_R, may slow down the rotation of the nanorods. However, due to the lack of

comparison measurements in water[6] of these nanorods, the accuracy of the results presented here could not be verified.

The second effect concerns the relative positions of the data points representing the three samples in the D_T-D_R plot shown in Figure 5.6 (a). They indeed occupy different regions in the plot, as expected, though the broad distribution of data points makes it difficult to identify the size and shape of particles based on this result. Sample "700" has the highest rotational and translational diffusion coefficients, as expected from its size; however, sample "600" was unexpectedly seen to have consistently smaller diffusion coefficients than sample "650". Currently, the cause of this discrepancy is unclear, but agglomeration or poor quality of the samples may be possible reasons.

The presence of contamination, agglomerations or other artefacts in the measured samples is also supported by the fact that several single-particle measurements had to be discarded because their autocorrelations did not show the characteristic decays expected and hence could not be fit to the ACF generated by our model. In many cases, autocorrelations resembling those in Chapter 4 were observed, which may be seen as evidence of the presence of spherical particles among the nanorods. These observations are supported by TEM images provided by the manufacturer, see Figure A.4 in Appendix A. In particular, the image of sample "700" shows a very heterogenous distribution of nanorods with aspect ratios ranging from ≈ 3 to ≈ 8, as well as several spherical nanoparticles, which were also seen in our measurements as mentioned above.

Finally, one should consider the proximity of the plasmon resonances of the nanorods, especially of the smallest ones (sample "700"), to the probe laser wavelength, since the plasmon-enhanced polarisability can enhance the detected signal strength but also may facilitate trapping-like effects, which distort the diffusional motion of the particles. In particular, the resonance wavelength of longer-than-specified nanorods seen in Figure A.4 (c) could actually coincide with the probe laser wavelength.

Further investigation is required to identify the origin of these results. While the measured effective hydrodynamic diameter already matches our expectations from theory to a large degree, the correct determination of D_R will enable us to fully and accurately characterise the diffusive behaviour and estimate both dimensions of rod-shaped nanoparticles.

[6] Whereas DLS provided a helpful comparison for the results in Chapter 4, it is not suited for the measurement of anisotropic particles.

5.3. Rotation Observation with a Stabilised, High-bandwidth Apparatus for Nanoparticle Investigation

So far, we have analysed the temporal behaviour of a single projection of the orientation of diffusing nanorods. But it would be indeed interesting to obtain full information about the orientation of an individual nanorod over the course of time. To realise this idea and reconstruct the two-dimensional nanorod orientation transverse to the cavity axis, the setup described in the previous chapters is extended to interrogate orthogonal polarisation modes of the cavity separately. The following section is dedicated to Rotation Observation with a Stabilised High-Bandwidth Apparatus for Nanoparticle Investigation (ROSHANI)[7]. We shall first look at the experimental realisation of this system, some polarisation-split measurements and the resulting angular trajectories, and then employ simulations to help interpret the results.

5.3.1. Experimental setup for ROSHANI

We recall from Section 2.1.3 that the ellipticity of cavity mirrors gives rise to two polarisation eigenmodes separated by a frequency $\Delta\nu_{\mathrm{pol}}$ given by Equation 2.16. For typical mirror pairs used in this work, the intrinsic polarisation splitting expected from the mirror geometry is $\Delta\nu_{\mathrm{pol}} \approx 700$ MHz; however, in practice, values near 2 GHz are observed due to fibre misalignments and tilt. Since a locked cavity can only be probed at a single resonance length, the two spectrally separated polarisation modes were simultaneously probed using the carrier and sidebands of frequency-modulated laser light. The sidebands were imposed with an EOM as described in Section 3.1.3, with the frequency set to $\nu_{\mathrm{EOM}} = \Delta\nu_{\mathrm{pol}}$. Light probing each polarisation eigenmode thereby has a sideband with its own polarisation which is resonant at the carrier resonance of the other polarisation (Figure 5.7 (b)).

In order to interrogate each polarisation mode separately, it is necessary to prepare the polarisation state of the light such that orthogonal polarisations can be properly separated for analysis. In contrast to the work presented so far, in which the polarisation controllers are used to align the incoming polarisation direction (from the laser / EOM) to one cavity eigenmode, they will now be used to rotate the polarisation to an incoming polarisation state $|E_{\mathrm{in}}\rangle$ having components along both cavity eigenmodes (see Figure 5.7 (a)). Light coupled out of the cavity then passes through a quarter-wave plate (QWP), a half-wave plate (HWP) and then a removable PBS. The QWP is used to make the polarisation, which may have been altered in the cavity fibres, linear once more, and the HWP rotates the polarisation direction such that the polarisation modes exiting the cavity coincide with the transmitted and reflected polarisations of the PBS axis. Each polarisation (arbitrarily called H and V) is then detected by a dedicated detector[8] ($\mathrm{APD_H}$, $\mathrm{APD_V}$) and oscilloscope channel.

Multimode fibres are incompatible with this setup due to cross-talk and mixing between modes. Indeed, this is the main motivation to build a cavity with two single-mode fibres in this work despite their more stringent alignment requirements. Single-mode fibres, when not actively perturbed, maintain separate polarisation modes, but are sensitive enough to torsional stresses to allow polarisation control via polarisation paddles.

[7] *Roshani* (रोशनी): Light, illumination.
[8] The additional detector was Thorlabs APD130A/M.

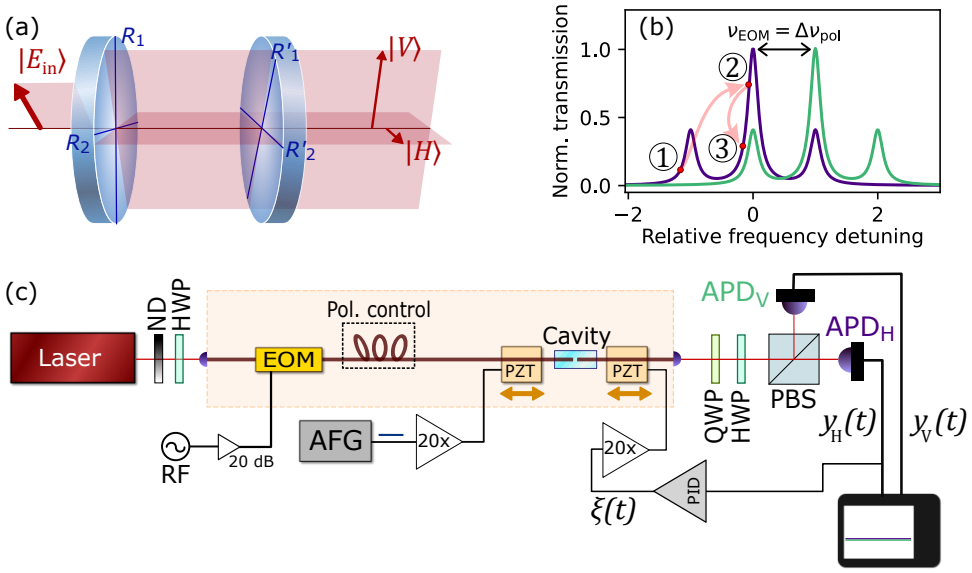

Figure 5.7: (a) Illustration of the generation of non-degenerate polarisation eigenmodes in a cavity with elliptical mirrors. The components of $|E_{in}\rangle$ along the cavity eigenaxes $|H\rangle$ and $|V\rangle$ are resonant at distinct frequencies separated by $\Delta\nu_{pol}$, corresponding to distinct cavity lengths for a fixed probe wavelength. (b) Schematic of sidebands set up at a frequency matching the polarisation splitting. The two polarisations are shown in purple and green, and circled numbers correspond to locking steps in Table 5.3. (c) The setup for ROSHANI features additional polarisation control after the cavity – a quarter-wave plate (QWP)), half-wave plate (HWP) and polarising beam-splitter (PBS) – and an additional photodetector.

Step no.	⓪	①	②	③
Set point	2.0	2.0	**0.5**	1.5
Gain	(1)	80	60	20
Function	Reset	Lock		

Table 5.3: Lock parameters for a polarisation-split measurement. Note the changed set point in Step ②, due to which the lock hops over the sideband and locks onto the flank of the carrier peak (see Figure 5.7 (b)).

Preparing for ROSHANI. The following procedure was developed and implemented to set and analyse the polarisation/frequency states of the input and output light:

1. With the PBS removed (no light to APD_V), the polarisation paddles are set so that both polarisation-split resonance peaks are visible in the $|H\rangle$ signal.
2. The PBS is added. The QWP and HWP are rotated so that each polarisation peak is recorded entirely and only by one oscilloscope channel (H or V).
3. The EOM is turned on and the RF frequency $\Delta\nu_{EOM}$ is set such that the sidebands coincide with the carrier peak of the other polarisation (see Figures 5.7 (b) and 5.8 (a)). An RF amplifier[9] was used to drive the EOM with the maximum permissible power.
4. Now, the polarisation paddles are adjusted so the amplitude of the sideband probing the $|H\rangle$ mode matches the amplitude of the carrier probing the $|V\rangle$ mode – see Figure 5.8 (a). The laser power can be increased so that this peak has the desired amplitude.

[9] Mini-Circuits ZX60-3018G-S+, 20 dB amplification at 2 GHz

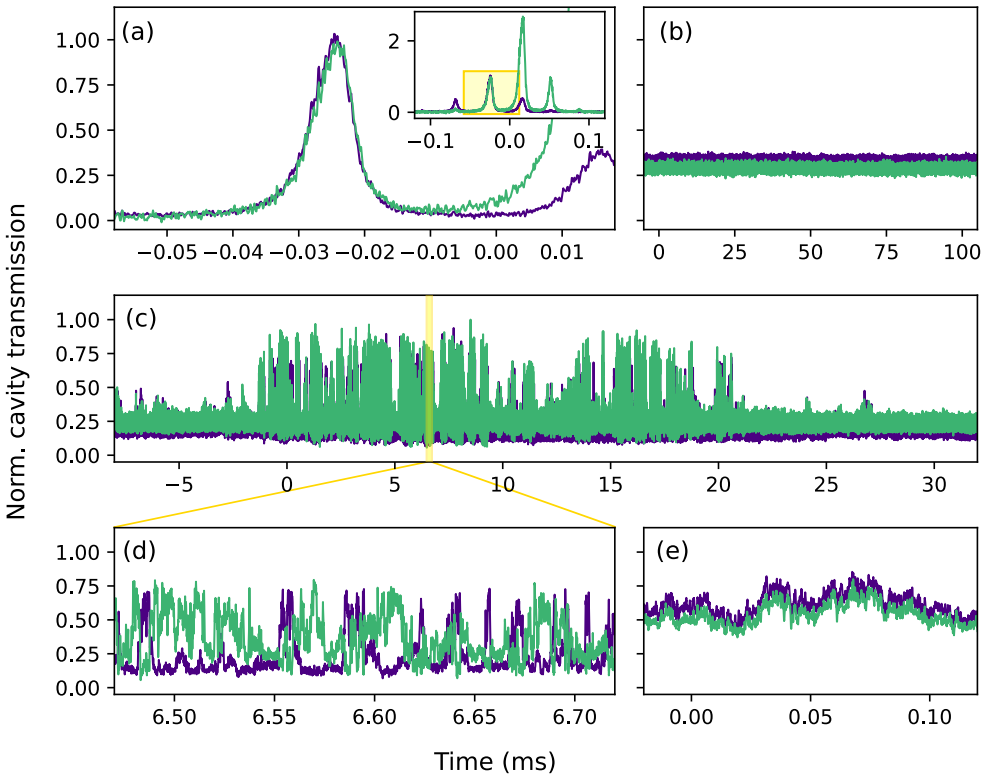

Figure 5.8: (a) Simultaneously probing orthogonal polarisation modes for locking and polarisation-split sensing. Inset: The complete polarisation-frequency structure on the same axes with the used peak highlighted (compare to Figure 5.7 (b)). Note that the horizontal axis corresponds to cavity length detuning of the scanned cavity. (b) $|H\rangle$ and $|V\rangle$ signals from the cavity when locked to the peak shown in (a). (c) Trace of a 25 nm × 10 nm nanorod. At longer time scales, both polarisation channels vary similarly. (d) Zoomed view of the trace in (c) showing the out-of-phase behaviour of $|H\rangle$ and $|V\rangle$ at the microsecond scale. (e) The transmission trace from a nanosphere event on the same scale as (d). Due to the isotropy of the particle, the two polarisation signals vary synchronously.

Since the cavity is probed at the flank of this peak, this step ensures that both polarisation components are probed with equal power. The amplitude V_{peak} of this peak is noted.

5. The EOM is turned off and the laser power turned down using the ND filter to set the amplitude of $|H\rangle$ to V_{peak}. The cavity lock input is calibrated using this peak. The lock sequence is set up with the parameters in Table 5.3.

6. The EOM is turned on again and the laser power returned to its previous level, so the *sideband* of $|H\rangle$ has amplitude V_{peak}. The lock sequence is then executed. The cavity is now locked to a single resonance length, but non-degenerate polarisation modes are read out simultaneously via the sideband structure described here.

Polarisation-split nanoparticle detection. Single nanoparticles were detected in a fashion similar to that in Chapter 4.1.2, with the difference that the measurement channels from both APDs must be recorded. At the time scale of 10 ms – 100 ms, both polarisation channels appear to behave similarly (Figure 5.8 (c)). However, zooming into a nanorod event on the scale of 10 µs – 100 µs (Figure 5.8 (d)) shows a marked difference: the two channels now vary out-of-phase with each other!

This behaviour is an indication of the rotational motion of the detected nanorod in the plane transverse to the cavity axis. We shall see in Section 5.3.2 that the amplitude of the nanorod signal in a particular polarisation channel is proportional to the projection of the nanorod's long axis on the corresponding polarisation direction. As a result, when the signal amplitude of one polarisation channel is maximum, the nanorod axis is most strongly projected onto that polarisation direction, and hence interacts most weakly with the orthogonal polarisation.

ROSHANI with nanospheres. As a control experiment, nanosphere events were also recorded with the polarisation-split setup. As can be seen in Figure 5.8 (e), both polarisation channels vary synchronously under the influence of a nanosphere, showing that their out-of-phase behaviour in the case of nanorods (Figure 5.8 (d)) was indeed due to the anisotropic shape of the particles. As a result, this system already enables us to immediately distinguish between nanoparticles of different shapes.

5.3.2. Tracking the rotation of nanorods

To track the rotational diffusion of a single nanorod, it is necessary to set up a model relating the nanoparticle orientation to each pair of $(|H\rangle, |V\rangle)$ values. Firstly, we shall consider the projection of the nanorod polarisability in the plane transverse to the cavity axis. If we consider a coordinate system with the z-axis parallel to the cavity, and the x- and y- axes along the H and V polarisation states respectively, then the angle which the nanorod, projected onto the xy-plane, subtends to the H-axis is ϕ.

The anisotropy of the polarisability of a nanorod means that the H- and V- polarisations will "see" different components of the nanoparticle polarisability. The H- and V-components of the nanorod polarisability are

$$\alpha_{\mathrm{H}} = \alpha_L \cos^2(\phi) \sin^2(\theta) \quad \text{and} \quad \alpha_{\mathrm{V}} = \alpha_L \sin^2(\phi) \sin^2(\theta). \tag{5.3}$$

The orientation-dependence of these quantities is shown in Figure 5.9 (a), where $|H\rangle \propto \alpha_{\mathrm{H}}$ and $|V\rangle \propto \alpha_{\mathrm{V}}$ are plotted as normalised values for 25 nm × 10 nm gold nanorods.

Since we assume the nanoparticle signal to be proportional to the frequency shift causing it, and that in turn is proportional to the particle's polarisability, we assume that the amplitude of the signal in the $|H\rangle$ or $|V\rangle$ channel is proportional to the component of the nanorod polarisability in the H or V direction respectively,

$$|H\rangle \propto \cos^2(\phi) \sin^2(\theta) \quad \text{and} \quad |V\rangle \propto \sin^2(\phi) \sin^2(\theta). \tag{5.4}$$

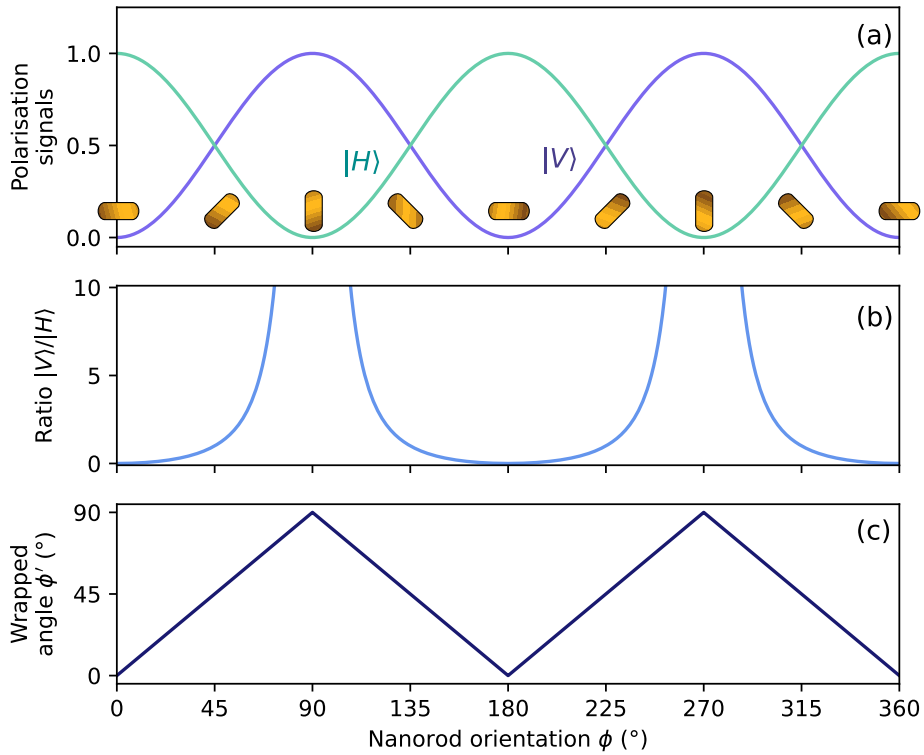

Figure 5.9: (a) The measured signals $|H\rangle$ and $|V\rangle$ are assumed to be proportional to the polarisability component of the nanorod in that direction. (b) Plots of $|H\rangle/|V\rangle$, which is equal to $\tan^2(\phi)$. (d) Due to the symmetry, the orientation which is calculated, ϕ', is wrapped to the interval $(0°, 90°)$.

The determination of ϕ from a $(|H\rangle, |V\rangle)$ pair follows from

$$\begin{aligned} \tan^2(\phi) &= \frac{|H\rangle}{|V\rangle} \\ \Rightarrow \quad \phi' &= \tan^{-1}\left(\sqrt{\left|\frac{|H\rangle}{|V\rangle}\right|}\right), \end{aligned} \tag{5.5}$$

which is shown in Figure 5.9 (c). Due to the fact that the tangent function is not injective, the value of ϕ' extracted is wrapped to $(0°, 90°)$. Physically, this arises from the fact that due to the symmetry of the polarisation modes, only the "wrapped" orientation of a nanorod within the domain of a quarter rotation, $\phi' \in (0°, 90°)$, can be determined.

5.3.3. Trajectories of rotating nanorods

Having established the experimental and theoretical background for rotation tracking, we shall now explore the rotational trajectories of nanorods, and additional statistical and dynamical information they can offer. We shall start with some experimental results, and then turn to simulations to confirm and interpret them.

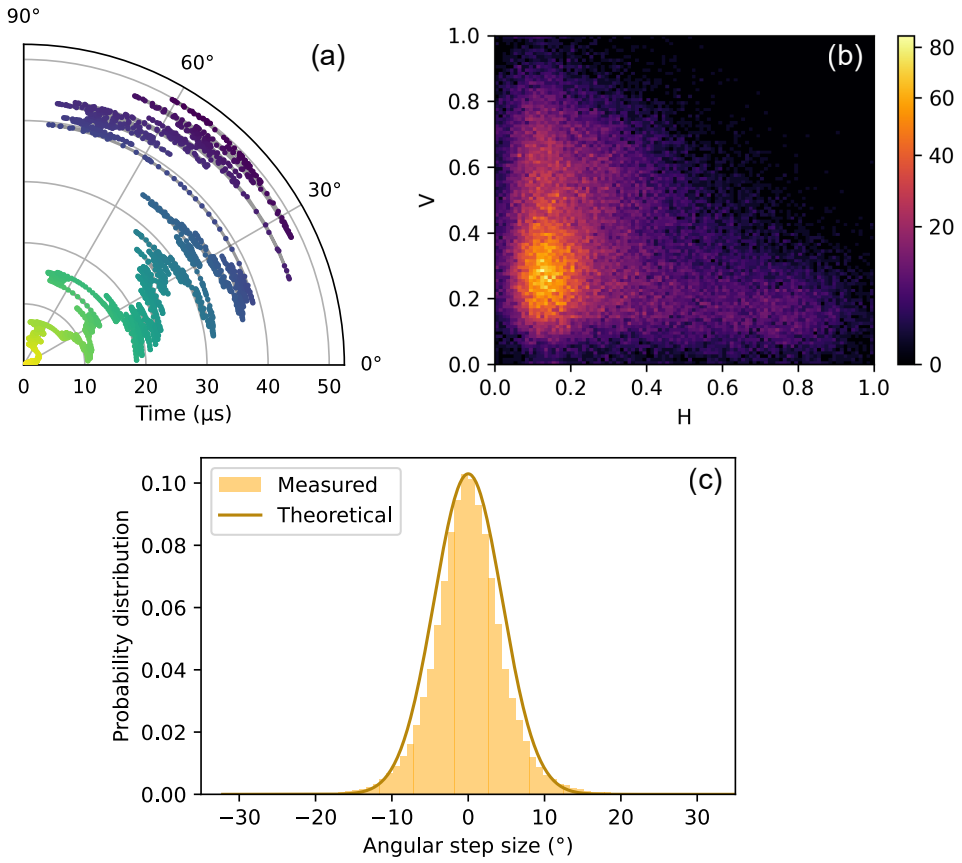

Figure 5.10: (a) Rotational trajectory of a single diffusing nanorod (sample "650"), measured with a temporal resolution of 20 ns. (b) Probability map of $(|H\rangle, |V\rangle)$ pairs in H-V space. Compare this to the simulation in Figure 5.11 (a). Note that the probability colour scale (in counts) is not linear for better viewing. (c) Distribution of step sizes from the trajectory shown in (a) for the determination of D_R.

Experimental rotation trajectories. Dual-polarisation nanoparticle traces such as that in Figure 5.8 (c) and (d) were recorded according to the previous section. In addition to the subtraction of a lower envelope as done for the analysis of nanoparticle events so far, in this case, an upper envelope over the nanoparticle event was also calculated and the signals hence normalised to the interval $[0, 1]$. Each $(|H\rangle, |V\rangle)$ pair thus obtained then corresponds to an $(|H\rangle, |V\rangle)$ pair in Figure 5.9 (a), and the time-resolved transverse orientation angle ϕ' of a diffusing nanorod was extracted. As mentioned before, the cavity-locked detection scheme enables data acquisition at very high speeds, so that even the rotational movement of nanorods (on the microsecond scale) can be temporally well resolved. An example of such a resulting rotation trajectory is shown in Figure 5.10 (a), with a time resolution of 20 ns (measurement bandwidth of 50 MHz).

Now that the temporal evolution of the angular orientation of a nanorod is known, we can use it to extract additional statistical information about the nanorod's rotational motion. Firstly, we analyse the step size distribution of orientation angles ϕ, as shown in Figure 5.10 (a), which is a Gaussian distribution with standard deviation $\sigma = \sqrt{2D_R\delta t}$, shown in Figure 5.10 (c). Hence, D_R was estimated to be 1.67 $\times 10^5$ rad^{2}s^{-1}, which is close to the theoretical value of 1.51 $\times 10^5$ rad^{2}s^{-1} for a 25 nm $\times$ 10 nm nanorod.

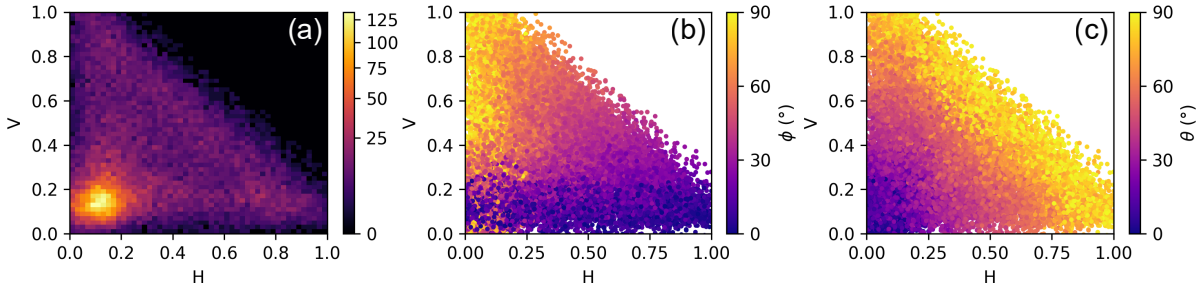

Figure 5.11: (a) Probability map of $(|H\rangle, |V\rangle)$ pairs in H-V space from simulations with $\sigma = 0.08$ pink noise added to mimic experimental data. Note that the probability colour scale (in counts) is not linear for better viewing. Each point in H-V space is mapped onto a particular azimuthal angle ϕ in (b) and polar angle θ in (c).

Additionally we can plot a probability map of $(|H\rangle, |V\rangle)$ pairs as shown in Figure 5.10 (b). This shows the relative occurrence of each possible $(|H\rangle, |V\rangle)$ combination in a nanoparticle event, and while this may not yet seem meaningful, we shall see in the next section that simulations of nanorod rotation can allow us to map each point in two-dimensional H-V space to a specific three-dimensional orientational state of the particle.

Simulated rotational trajectories. Extracting the orientation ϕ of the nanorod's projection transverse to the cavity axis from rotation simulations is now simpler than the process in Section 5.3.3: we may directly use the azimuthal angle wrapped to the interval $(0°,\ 90°)$,

$$\phi' = \begin{cases} \phi \bmod 180° & \text{if } 0 < \phi \bmod 180° < 90° \\ 180° - \phi \bmod 180° & \text{otherwise.} \end{cases} \tag{5.6}$$

In Section 5.3.3, we saw the measured probability distribution of $(|H\rangle, |V\rangle)$ pairs in two-dimensional H-V space. Now, using simulated rotation data, we can map each state in H-V space to a specific three-dimensional nanorod orientation. In Figure 5.11 (b) and (c), each point on in H-V space is mapped onto a particular azimuthal angle ϕ and polar angle θ respectively. In particular, panel (b) shows that data points near the H-axis correspond to nanorod orientations along the H-axis, and similarly for the V-axis, as expected. Interestingly, panel (c) yields information about the out-of-plane orientation of the nanorod: points further away from the origin correspond to a larger polar angle of the nanorod to the cavity axis, i.e. a larger transverse component of its orientation while points near the origin correspond to positions in which the nanorod lies more parallel to the cavity (z-axis).

Figure 5.12 (a) shows a resulting simulated rotational nanorod trajectory, which can be compared with Figure 5.10 (a). Note that, since the time scales of rotation (microseconds) are much smaller than that of translational diffusion (milliseconds), the "envelope" due to the latter was neglected while simulating pure rotation.

We used the statistics of the distribution of two-dimensional angular step sizes to estimate the rotational diffusion coefficient of measured nanorods in Section 5.3.3. Now, we repeat this exercise with simulated data to verify the validity of this method. In fact, we shall compare the results obtained from complete three-dimensional simulated data and the two-dimensional projection, as measured in ROSHANI experiments.

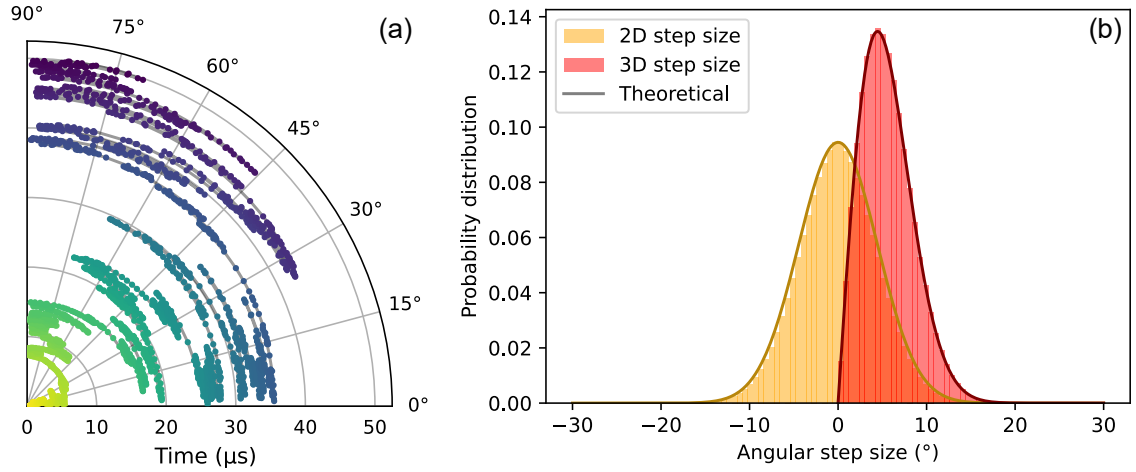

Figure 5.12: (a) Rotational trajectory of a single nanorod extracted from a simulation as shown in Figure 5.1 (a) with a temporal resolution of 20 ns. (b) Statistics of 2D and 3D angular step size for the determination of D_R.

We saw in Section 2.4.3 that the three-dimensional angular step size $\Delta\Phi$ follows a distribution where the mean is the MSAD given by $\langle\Delta\Phi^2\rangle = 4D_R\delta t$, where δt is the simulation time step. Hence the statistical mean of the distribution of 3D step size, $P(\Phi) \propto \Phi\exp(-\Phi^2/(4D_R\delta t))$, shown in Figure 5.12 (b) can be used to calculate D_R. In the 2D case, the distribution is a simple Gaussian, and the approach for the estimation of D_R is given in Section 5.3.3. Results from both pathways are presented in Table 5.4. Importantly, this verifies that the analysis of angles in the *two-dimensional rotation trajectory* enabled by the polarisation-split measurement scheme introduced here is a valid pathway for the statistical determination of the rotational diffusion coefficient of motion in *three dimensions*.

Method	D_R (10^5 rad^2 s^{-1})
3D distribution	1.52
2D distribution	1.46
Theory	1.52

Table 5.4: The rotational diffusion coefficient obtained from simulations by various statistical pathways and the Tirado-de la Torre diffusion theory.

5.3.4. Rotational and translational dynamics of nanorods

ROSHANI not only provides spatial rotational data, but also yields richer information about the rotational dynamics of nanorods than is available from a single polarisation channel. For example, sum and difference signals from dual-polarisation measurements present additional information in their respective autocorrelations, and cross-correlating $|H\rangle$ and $|V\rangle$ yields information about the different types of dynamics taking place.

Sum and difference signals. The normalised autocorrelations of $|H\rangle$, $(|H\rangle+|V\rangle)$ and $(|H\rangle-|V\rangle)$ are compared in Figure 5.13 (a), *without* any offset correction. The three signals represent three different aspects of nanorod diffusion:

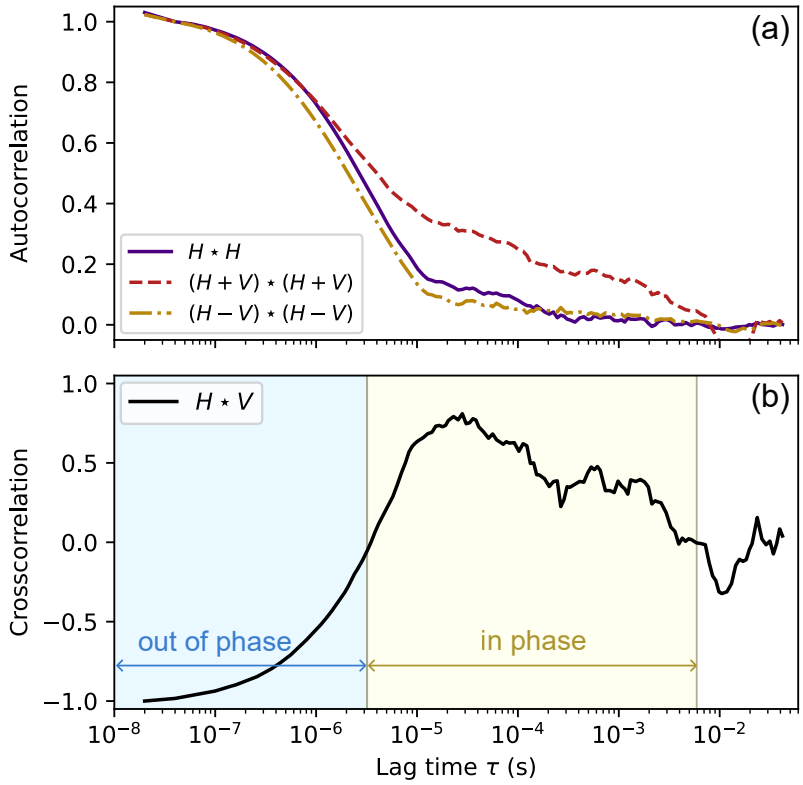

Figure 5.13: (a) Normalised autocorrelations of a single polarisation signal (H), and of the sum ($H+V$) and difference ($H-V$) of orthogonally polarised signals, respectively. (b) The cross-correlation of orthogonally polarised signals.

- The singly **polarised signal** $|H\rangle$ contains information about diffusion and rotation with respect to one polarisation direction.
- In the **sum signal**, $|H\rangle + |V\rangle$, information about the out-of-phase variation of the two polarisations is averaged out. As a result, this signal does not contain information about rotation in the transverse plane, and the contribution due to translational diffusion (seen as bumps at $\tau > 10^{-5}$ s) is more pronounced. The remaining decay around 1 µs is thought to arise due to rotation out of the transverse plane and towards the cavity axis. This component of rotation is seen by both polarisations equally, and therefore survives in the sum signal.
- The **difference signal**, $|H\rangle - |V\rangle$, is a measure of contrast between the two orthogonally polarised signals, and synchronous motions are cancelled out. As a result, the contribution of translational diffusion vanishes nearly completely compared to $|H\rangle$. The decay in the autocorrelation is now due to rotation in the transverse plane only.

Cross-correlation. As we saw in Figure 5.8 (c) and (d), $|H\rangle$ and $|V\rangle$ vary in phase with each other at "longer" times scales and out of phase at "shorter" time scales. The cross-correlation $|H\rangle \star |V\rangle$ offers a quantitative measure of this behaviour. As seen in Figure 5.13 (b), the cross-correlation is negative for lag times $\tau \lesssim 3.2$ µs, which corresponds to out-of-phase behaviour of the two signals. The cross-correlation is positive for $\tau \gtrsim 3.2$ µs (until $\tau \sim 10^{-2}$ s, where the correlation is lost or dominated by noise), corresponding to in-phase variation of the

signals. Physically, the former corresponds to transverse rotation, and the latter to translational diffusion, which is seen by both signals in equal measure. Hence, the cross-correlation allows us to quantitatively and temporally separate two types of dynamics in a nanorod event.

5.4. Optical trapping

So far, the optical microcavity has been used to sense and measure the dynamics of freely diffusing nanoparticles. The idea of using optical trapping to confine their motion expands the functionality of the microcavity by allowing us to control the nanoparticle dynamics as well, and provides an interesting use case to which the analysis methods of the previous sections can be applied. In the following, the trapping of single nanorods in five degrees of freedom will be demonstrated. It should be noted that this is not an exhaustive investigation into cavity-based optical trapping, but intends to introduce this topic and the possibilities it provides in the context of cavity-enhanced sensing.

5.4.1. The basics of optical trapping

In the context of optical trapping, two forces must be considered: the **gradient force**, proportional to the intensity gradient of the trapping beam, and the scattering force due to **radiation pressure**, acting in the direction of the beam propagation. In the Rayleigh regime, which is valid for all the nanoparticle species investigated here, the time averaged optical force is on a nanoparticle in an electromagnetic field is [111, 112]

$$\langle \mathbf{F} \rangle = \underbrace{\frac{\Re(\alpha)}{2} \nabla \langle |\mathbf{E}|^2 \rangle}_{\text{Gradient force}} + \underbrace{\frac{n_\mathrm{m}}{c_0} \sigma_\mathrm{ext} \langle \mathbf{E} \times \mathbf{B} \rangle}_{\text{Radiation force}} \tag{5.7}$$

Optical trapping at the field maximum is achieved when the gradient force dominates the radiation force. Optical trapping experiments typically use a tightly focussed beam to maximise the intensity gradient, and input powers of between several milliwatts and watts may be required to provide sufficient trapping force [113]. The Fabry-Perot cavity offers several advantages for trapping. Firstly, the **small mode volume** and standing-wave geometry of the optical field already provides a high intensity gradient, with an enhancement of about 15 times compared to a focal spot with the same power and beam diameter. Secondly, the **power enhancement** in the cavity means that a small fraction ($\sim 10^{-4}$) of laser power is required to achieve the same trapping power as a single laser focus. Finally, the standing wave field **transfers no momentum**, so the scattering force due to radiation pressure in Equation 5.4.1 vanishes.

Stable trapping is achieved when the trap energy (U) is significant compared to thermal energy ($k_B T$). Trichet *et al.* define the "trap strength" as the ratio of these energies, $f = \alpha I/(n_\mathrm{m} \varepsilon_0 c_0 k_B T)$, which, for a gold nanorod (25 nm × 10 nm) in a cavity at 300 K, is roughly $f \approx 2.5\ \mathrm{W}^{-1} \cdot P_\mathrm{cav}$ [43]. This means that an intracavity power on the order of 1 W would be needed for trapping, ignoring the increase in temperature due to photothermal heating – a simplification which should be treated with caution if a rigorous study of cavity-based trapping is desired!

5.4.2. Dynamics of a trapped nanorod

Trapping experiments were performed in which a power series was measured by varying the input optical power to the cavity. Nanorod (25 nm × 10 nm in CTAB) events were measured as before. The effect of the optical power in the cavity was investigated by comparing the autocorrelations of individual particle events. Since the aim of this analysis is not quantitative fitting but a comparative study, steps introduced in Chapter 4 such as offset correction were not performed.

We now wish to investigate how the motion of the nanorod changes when it enters cavity fields with increasing optical power. The rotational and translational diffusion dynamics are once again described by the autocorrelations of the particle events, which are shown in Figure 5.14 (a). Note that in this figure, the autocorrelation is normalised to the level between the rotation and diffusion decay, for a reason which will become clear momentarily. At the lowest circulating optical power used (40 mW, light blue) two decays are visible: one at 1 µs, due to rotation, and the other at 100 µs, due to diffusion. As the intracavity power increases, two changes occur in the autocorrelation: the rotation decay diminishes and finally disappears, and the diffusion decay is lengthened. These observations are consistent with similar studies in the literature [114].

Freezing of rotational motion. At high optical powers, the rotation decay around 1 µs vanishes. This suggests that the nanorods have oriented themselves along the polarisation direction of the optical field in the cavity and that their rotational motion has ceased [114].

Lengthening of residence time. As the optical power increases, there is a spatial confinement of the nanoparticle, limiting its diffusional motion. This is seen in the stretching of the diffusion autocorrelation to longer lag times. This behaviour is quantified by defining a "residence time" of the nanoparticle in the cavity as the time where the diffusion autocorrelation decays to (arbitrarily) 20% of its amplitude. The variation of the residence time as a function of intracavity power is shown in Figure 5.14 (b), and roughly follows an exponential dependence (violet curve) on P_{cav}, consistent with the Kramers escape rate, $\exp(U/k_BT)$. Additionally, a significant increase in residence time occurs when $P_{\mathrm{cav}} \gtrsim 2$ W, which is close to the stable trapping power estimated from the trapping strength f above. Finally, we notice that at the powers typically used in the sensing experiments described in this work, there is no trapping- or photothermally-induced slowing of diffusional motion, which would otherwise distort the particle dynamics measured.

5.4.3. The orientation of trapped nanorods

With the procedure developed in Section 5.3, we can now "look at" the orientation of a nanorod trapped in the cavity in addition to analysing its dynamics. By applying the technique for ROSHANI to measurements of trapped nanorods, we get the results shown in Figure 5.15, which were taken with a slower locking bandwidth of 10 Hz. In panel (a), we see that the microsecond-scale out-of-phase oscillations has been largely frozen out. Translating these

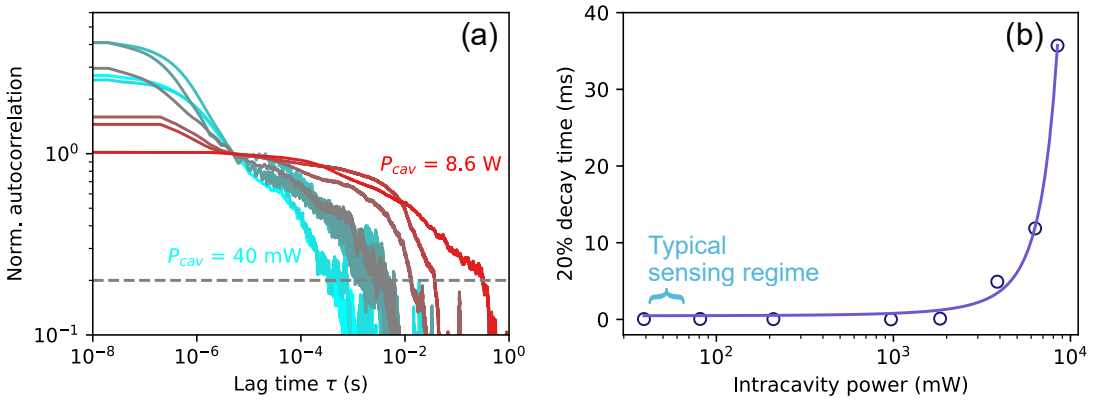

Figure 5.14: (a) Autocorrelations of single nanoparticle events as an optical power series normalised to the level between rotation and diffusion. The intracavity powers used were P_{cav} = 40 mW, 82 mW, 213 mW, 981 mW, 1.8 W, 3.9 W, 6.4 W and 8.6 W. The autocorrelations of the first six powers were done with 50-ms-long measurements taken at 50 MHz, and the last two with 500-ms-long measurements at 5 MHz. (b) The residence time, defined as the lag time at which the diffusion decay in the autocorrelation drops to 20% of its amplitude (dashed grey in (a)), as a function of intracavity power.

signals into an orientational trajectory[10] in panel (b), we see that the nanorod appears to indeed maintain its orientation along the H- and V- axes for extended periods of time (~ 1 ms), supporting the idea that the trapping cavity field confines the nanorod orientation to the polarisation directions. Finally, panel (c) shows that, in contrast to Figure 5.10 (b), the nanorod orientation probablity is concentrated in two spots roughly aligned to the H- and V- axes. The fact that the two nanorod alignments in Figure 5.10 (b) and (c) do not coincide exactly with the H and V axes is a result of normalising signals containing noise and occasional "spikes", which prevent the actual signal from reaching the extremes of the $[0, 1]$ interval – which would be mapped to $\phi' = 0°$ or $90°$.

Discussion of results. In the previous section, evidence of optical trapping was presented in the temporal and spatial domains. By looking at the dynamics of a trapped nanorod via their autocorrelation, we saw that at high trapping powers, rotational motion ceases, and diffusion slows down as the particle spends longer in the field antinode. Using the approach for ROSHANI, we could look at the trapped orientational states, which appear aligned to the cavity polarisation eigenmodes.

In order to quantitatively study or employ the trapping mechanism in a microcavity, some aspects should be considered which were not accounted for so far. Firstly, at the high intracavity powers demonstrated in trapping experiments, one expects significant heating of the cavity medium. This will give rise to thermal gradients and convection currents, which will also influence the motion of diffusing particles. Furthermore, photothermal effects distort the cavity's resonance spectrum [40, 99] so that the resonance lineshape differs from a Lorentzian, and the locking system's response to external disturbances and nanoparticles is no longer well defined. Finally, trapping longer than the millisecond scale can no longer be reliably measured by a locked cavity, because, unlike the case where only fast nanoparticle dynamics were considered, the lock would correct the effect of a trapped particle on long times scales. In summary, implementing high optical powers in the microcavity can enhance its functionality,

[10] The trace is scaled to fill the angular range between 0°and 90°.

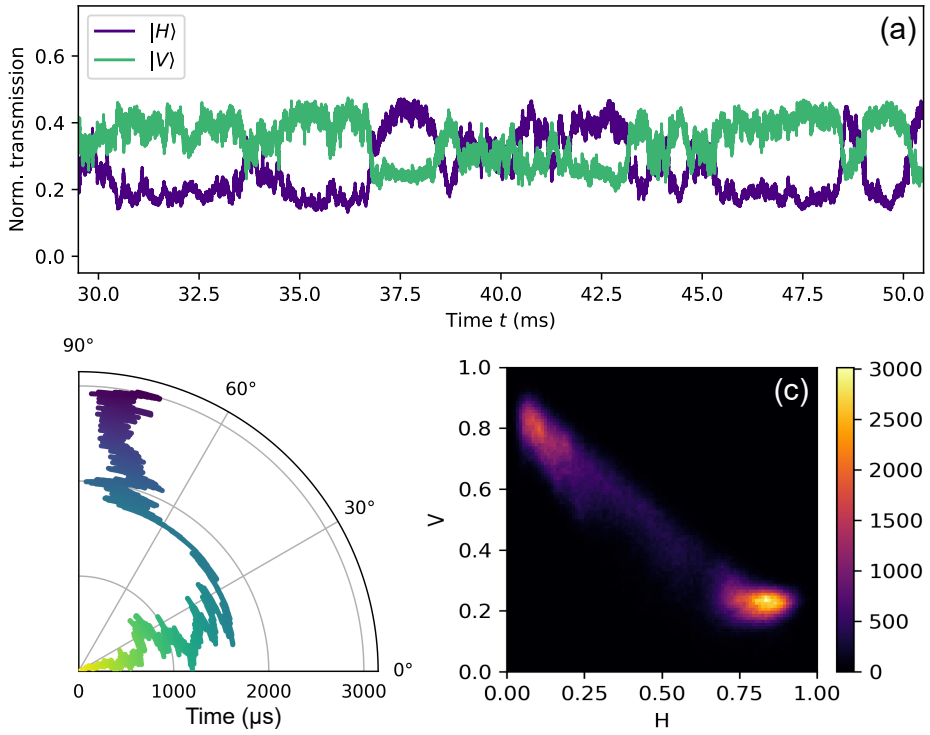

Figure 5.15: (a) Polarisation-split signals of a nanorod trapped with an estimated intracavity power of $P_{\mathrm{cav}} = 21$ W. While the out-of-phase behaviour from Figure 5.8 (d) is visible, rotational diffusion on the microsecond scale appears to be frozen out. (b) The orientational trajectory of the trapped nanorod shows long (~ 1 ms) regions in which the orientation is aligned to the H- or V- axis. When comparing to Figure 5.10 (a), do note the different time scales. (c) The H-V plot of orientation distributions of the trapped nanorod shows two distinct patches, corresponding to the H- and V- orientations.

but also opens the system up to complex interactions between optical forces, photothermal effects and the locking mechanism, which require in-depth studies beyond the scope of this work. In the future, these phenomena should be analysed to separate their influence on the measured nanoparticle motion.

5.4.4. An outlook of optical trapping

In the previous sections, preliminary experiments on optically trapping single nanoparticles were presented. So far, we have seen the capability to confine the motion of a nanorod in five degrees of freedom: the particle is held at the cavity field antinode in three dimensions, and two degrees of rotation are frozen out as the particle aligns itself to the polarisation axis of the optical field. In the context of cavity-enhanced sensing, optically trapping a nanoparticle could

- produce a stationary probe for plasmon-assisted detection of other particles,
- be used to study the interactions between nanoparticles, e.g. binding of biomolecules to a trapped host,
- allow multiple statistical measurements of a single particle by repeatedly drawing it back into the field maximum for repetitive sampling,

- further enable the characterisation of the interaction between the nanoparticle and its surrounding medium, e.g. its coefficient of friction [43].

In summary, further work towards optimising optical trapping in the context of microcavity-based sensing could expand the functionality of the microcavity and enable measurements schemes for the advanced characterisation of biochemical and optofluidic processes on the nanoscale.

Origami, the Japanese art of paper folding, has existed since the seventh century and has found applications in several fields of engineering, science and medicine today, from aerospace technology to biomedical engineering.

6. Biosensing

While nanoparticles and nanosystems of interest pervade many aspects of our lives, this work was particularly motivated by the aim of sensing and characterising biological nanoparticles. Theoretical and practical tools for the quantitative sensing of nanoparticles have been developed in the previous chapters, and they will now – finally – be applied to biological samples.

The aim in this chapter is to sense and characterise single biological nanostructures. This is achieved in Section 6.1 with DNA nanorods. We shall also explore measurements of proteins, albeit in ensembles of several molecules at a time, in Section 6.2. This chapter concludes by presenting future perspectives for biosensing with an optical microcavity.

6.1. Sensing of single DNA nanostructures

James Watson and Francis Crick could hardly have made a grosser understatement when they suggested that their proposed structure of DNA, which was published in 1953 and would win the Nobel Prize in 1962, would be of "considerable biological interest" [115]. Not only has their discovery been vital in progressing our understanding of genetics, but it also has opened up new fields of nano- and biotechnology based on the assembly of DNA nanostructures.

A branch of nanotechnology of growing interest is so-called "DNA origami", which involves the self-assembly of DNA into well-defined structures on the nanoscale [116], and has applications ranging from medicine [14] to plasmonic sensors [16, 17] and other optical nanostructures [15]. In this section, self-assembled DNA nanorods "24HB" synthesised in the research group of Prof. Tim Liedl at LMU, Munich, are introduced as a novel subject for single-particle biosensing with the optofluidic microcavity. According to scanning electron microscopy (SEM) images (Figure 3.11), these nanostructures are rod-like and have dimensions of roughly $L = 110$ nm and $d = 10$ nm, corresponding to $D_T = 10.8\ \mu m^2 s^{-1}$ and $D_R = 5.3 \times 10^3\ rad^2 s^{-1}$, allowing us to now apply the methods in Chapter 5 to a *biological* sample. The conformation of these structures is highly sensitive to their environmental conditions (salt concentration, pH, etc.), and they were maintained in a 1x Tris-acetate EDTA (TAE)[1] buffer solution to avoid unwanted (un)folding. Prior to introducing DNA into the microcavity, the microfluidic system was passivated with BSA, which also presented an opportunity for the detection of these proteins as described in Section 6.2.

An example of a single DNA event is shown in Figure 6.1 (a). An analysis of its dynamics via autocorrelation was performed once more, and the autocorrelations of multiple single DNA events are shown in Figure 6.1 (b), with their average plotted darker. Decays from $G_{SW}(\tau)$ as expected for a particle with the dimensions mentioned above (maroon dashed) are already

[1] Diluted from 10x concentrated Tris-acetate EDTA buffer from Sigma Aldrich: The 1x TAE solution contains 40 mM tris-acetate and 1 mM EDTA.

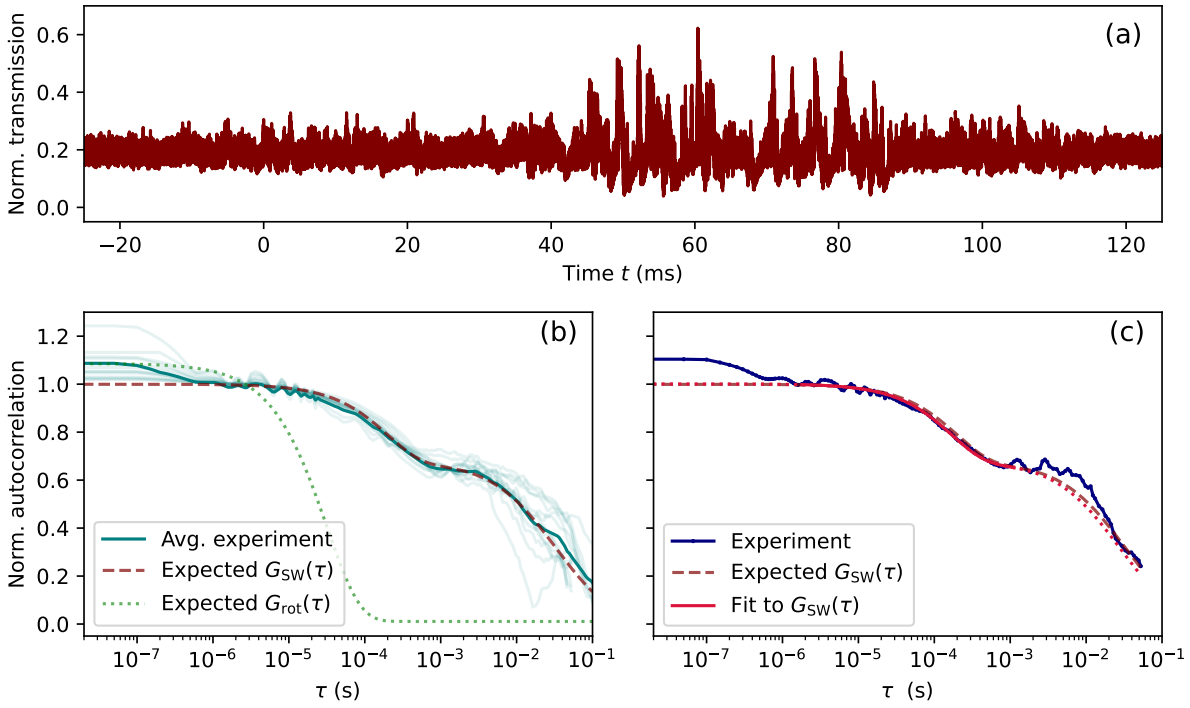

Figure 6.1: (a) Cavity transmission trace of a single DNA nanobundle transit. (b) The autocorrelations of several DNA events with their average shown dark. Theoretically expected ACFs for the rotation and diffusion of nanorods with $L = 110$ nm and $d = 10$ nm are shown dotted green and dashed maroon respectively. (c) Neglecting possible effects due to the rotation decay, the two longer decays were fit to $G_{SW}(\tau)$, shown in crimson, according to the procedure presented in Chapter 4, to yield an effective hydrodynamic diameter of the nanostructure.

visible. While another decay corresponding to the expected rotational ACF, $G_{rot}(\tau)$, is not apparent around 10^{-5} s – 10^{-4} s, a smaller decay emerges at sub-microsecond times. Two interpretations have been hypothesised to explain these observations. Both centre around the fact that, in comparison to the rigid nanorods studied in the previous chapters, we are now in the domain of "soft matter", where we are susceptible – and sensitive – to conformational changes of our samples.

First, the DNA structures, which appeared rod-like in SEM images, may have folded or curled into a more compact shape in dispersion. The consequence of this effect is the increase in the rotational diffusion coefficient and a decrease in the amplitude of the rotation decay, as the particle approaches a more spherical form. In this case, the fast decay would be the shifted rotation decay, corresponding to $D_R = (3.2 \pm 0.6) \times 10^5$ rad^2 s^{-1}. This is substantially higher than we would expect. Meanwhile, the two slower decays were fit to $G_{SW}(\tau)$, as illustrated in Figure 6.1 (c), to yield a mean effective hydrodynamic diameter of (41 ± 8) nm (equivalent to $D_T = (10.5 \pm 2.1)$ µm^{2}s^{-1}), which is in excellent agreement with the calculated hydrodynamic diameter of a 110 nm × 10 nm rod, which is 39 nm.

The second possibility, which offers an even more exciting outlook to microcavity-based sensing, is the observation of a dynamical process other than rotation and diffusion. Due to the geometry of the nanobundles, in particular their large aspect ratio, the expected rotation and diffusion decays lie temporally close together (Figure 6.1), making them difficult to distinguish. In this case, the rotation decay could be "masked" by the diffusion decay at 10^{-4} s, and the decay at 10^{-7} s could arise from a process not yet considered in this work. The fact that our sample is

now considerably longer and less rigid than gold nanorods suggests the formation, for example, of physical bending modes which cause fast fluctuations in the interaction with the probing cavity field. According to a rough estimate using macroscopic mechanics, the frequency of such bending would approach the gigahertz range[2] in vacuum; however, it is plausible that in a viscous medium like water, and at the nanoscale, the bending dynamics are considerably slower.

With its sensitivity to conformational variations of single nanoparticles, and the possibility to detect conformational changes such as folding, bending, etc. with a high bandwidth, the optofluidic microcavity shows great promise to enable the time-resolved investigation of a variety of physical and biochemical processes on the nanoscale.

6.2. Sensing of protein molecules

BSA is a protein molecule with a molecular weight of 66.5 kDa derived from the blood of cows, which is widely used in biotechnology, for example as a carrier protein or a standard for protein assays. Though the molecule has a complex, roughly triangular shape, it has been approximated to behave hydrodynamically like an ellipsoid with $L \approx 14$ nm and $d \approx 4$ nm [103]. The corresponding diffusion coefficients, $D_T = 52.7\ \mu\text{m}^2\text{s}^{-1}$ and $D_R = 1.19 \times 10^6\ \text{rad}^2\text{s}^{-1}$, shall be used as a reference in this section. Known for its "stickiness", it is often used for the passivation of surfaces, which is actually the reason it was introduced into the optofluidic microcavity in the first place. However, it offered the opportunity for the measurement in its own right, which is discussed in the following. The detection of single protein molecules was not yet achieved; however, measurements were performed for several concentrations from 1 µM to 1 nM.

With these concentrations, we have a steady-state system in which the cavity mode volume is always populated by BSA molecules. As a result, the identification of particle events is not necessary and also not possible, and the autocorrelation was performed using the entire signal. The results are shown in Figure 6.2. In the main panel, measurements were performed with concentrations down to 10 nM. The measurement in the inset was acquired in another measurement run and, unfortunately, oscillations from the background come through clearly in the autocorrelation. However, it still shows the successful detection of BSA proteins at a concentration of 1 nM, corresponding to about 10 molecules in the observation volume.

Due to the anisotropy of the molecule, we observe a decay at 10^{-7} s – 10^{-6} s, which arises from the rotational diffusion of the molecules. The expected rotational decay for a 14 nm × 4 nm nanorod is shown by dotted curves in Figure 6.2. The two diffusion decays expected from $G_{\text{SW}}(\tau)$ occur around 10^{-5} s and 10^{-3} s, shown by dashed maroon curves, and correspond to an effective hydrodynamic diameter of 8.1 nm calculated using the dimensions mentioned above. This calculated value is comparable to with hydrodynamic diameters reported in the literature, for example 6.96 nm by Axelsson [120]. We observe a clear and consistent dependence between the amplitude of the rotation decay and the BSA concentration: it gains in prominence when fewer molecules are examined. This is expected, because fluctuations due to the rotation of

[2] Natural bending frequency: $f_0 = \frac{\pi d}{8L^2}\sqrt{\frac{Y}{12\rho}}$, where Y is the Young's modulus of DNA and ρ is its density [117–119]. Of course, the values used are merely estimates of the structural properties of DNA!

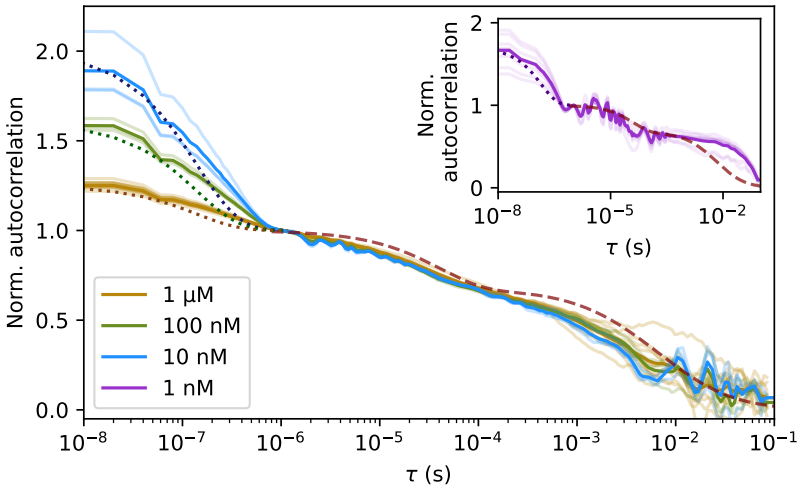

Figure 6.2: Autocorrelations of BSA measurements with 1 µM, 100 nM, 10 nM and (inset) 1 nM concentrations, normalised to the lag time separating rotation from translation (≈ 1 µs). The maroon dashed curve and the dotted curves show the theoretical ACFs $G_{\mathrm{SW}}(\tau)$ and $G_{\mathrm{rot}}(\tau)$ respectively, modelling the molecule as a 14 nm × 4 nm nanorod.

individual molecules gets "washed out" in measurements with a large number of molecules in the observation volume.

Rotational diffusion dynamics are often measured using fluorescent markers, which themselves can influence the motion of the sample. Using the method shown in Chapter 5, however, the diffusion coefficients of the (unlabelled) proteins were estimated from our measurements, and are displayed in Figure 6.3. The increase in the rotational diffusion coefficient with decreasing concentration agrees with observations in the literature: it is well-known that the diffusive behaviour of molecules like BSA is heavily dependent on factors such as their concentration, the presence and concentration of salts in the solution, pH and temperature [121–123]. The translational diffusion coefficient remained constant over the concentrations measured here, and was calculated from all the measured data to be $D_T = (67 \pm 9)$ µm^2 s^{-1}. This agrees very well with values reported in the literature, for example 63.2 µm^2 s^{-1} reported by Gaigalas *et al.* [123] and 61.7 µm^2 s^{-1} reported by Axelsson [120], and the value calculated for a nanorod as mentioned earlier ($D_T = 52.7$ µm^2 s^{-1}). Similarly, D_R from Figure 6.3 is comparable to, although somewhat higher than that ($D_R = 1.19 \times 10^6$ rad^2 s^{-1}) expected for a nanorod. This is not unexpected, since the protein takes a roughly triangular shape instead of a rod, which was assumed for this estimation of D_R.

6.3. Outlook

In this chapter, we explored the sensing of two species of biological nanoparticles: BSA protein molecules and DNA nanorods. While experiments with single protein molecules have not yet been performed, the rotation and diffusion dynamics of BSA could be identified in ensemble measurements with about 10 molecules being observed, and the diffusion coefficients of the proteins thus derived.

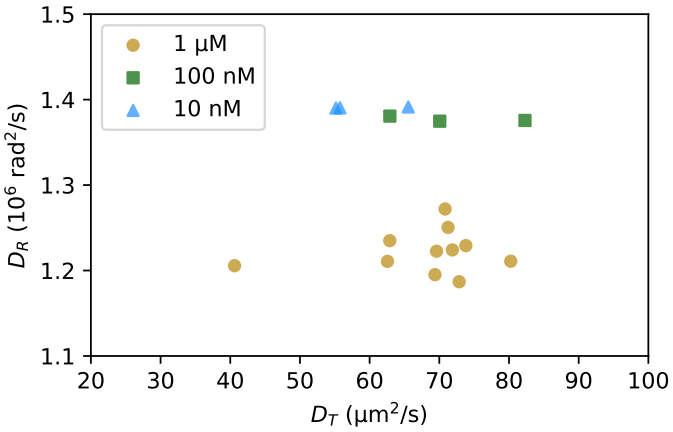

Figure 6.3: Diffusion coefficients (D_T) and rotational diffusion coefficients (D_R) estimated from BSA measurements shown in Figure 6.2. Each data point belongs to a measurement, which itself includes multiple individual molecules.

On the other hand, DNA nanorods were easily detected on the single particle level and once more, the dynamics could be resolved using the autocorrelation function with an excellent temporal resolution, providing an effective hydrodynamic diameter in agreement with our expectations. In addition, a fast decay occurring at sub-microsecond time scales was observed, which could be a sign of conformational dynamics such as bending of the nanorods. This idea opens up possibilities to measure dynamical processes of single nanoparticles, such as folding and bending, which can give an insight into interactions between a sample and its surroundings, and hence will enable us to explore physical processes and biochemical interactions even far beyond the diffusion dynamics investigated thus far.

Most biochemistry occurs in aqueous environments, and the capability to measure processes on the single-particle level opens a window into the world of physical, chemical and biological interactions on the nanoscale.

7. Conclusion and outlook

As the ability to investigate the behaviour of single particles at the nanoscale becomes increasingly relevant and essential in many fields of science, medicine and technology, this work presents developments towards an optofluidic sensor capable of characterising single unlabelled nanoparticles underwater. A fibre-based Fabry-Perot microcavity based on earlier work [47] operated in cavity-locked mode enables the dispersive sensing of a variety of nanoparticles with a measurement bandwidth orders of magnitudes faster than many other techniques available today, allowing the investigation of not only diffusional dynamics, but also faster rotational motion of anisotropic objects.

The locked microcavity. The Fabry-Perot microcavity is based on two mirror-coated fibres in a microfluidic channel, separated by a cavity length of $\ell < 5$ µm. This yields a mode volume of about 10 µm^3, which is fully accessible to nanoparticles diffusing through the sample. The **high finesse** ($\sim 5 \times 10^4$ in water) and **excellent cavity length stability** ($\sim$ 300 fm RMS) make the locked cavity sensitive to small dispersive shifts due to single nanoparticles.

Single nanosphere sizing. A central new capability demonstrated in this work is the **quantitative sizing** of single particles by direct analysis of their diffusion dynamics. To achieve this, a **new analytical ACF** was derived for diffusion in the microcavity field. This was necessary since most established autocorrelation-based measurement techniques such as FCS employ a laser focal spot as the observation volume, instead of a standing wave. In addition, measures were introduced to take into account the transient nature of single-particle events: also a necessary step, because the derivation of the conventional autocorrelation function for diffusion assumes a steady-state process.

Hence, autocorrelated experimental traces of single particle transits through the cavity could be directly fit to the analytical ACF, and the diffusion coefficient D_T of individual nanoparticles determined. Monte-Carlo simulations of diffusing nanoparticles confirmed the accuracy of this analysis method. Transits of several single citrate-stabilised gold nanospheres were thus recorded and evaluated, yielding size distributions which matched excellently with comparison measurements by DLS and TEM, while offering several practical advantages over these methods (e.g. smaller sample volumes required and measurement in an aqueous environment, respectively). Interestingly, we observed a deviation in particle size from the sizes specified by the manufacturer, a result confirmed by comparison measurements, which already demonstrated the ability of this nanosensor to detect small variations in nanoparticle size and an initial use case in quality control. The smallest nanospheres measured were nominally 3 nm in diameter, corresponding to 20 gold atoms across, or a molecular weight of about 160 kDa. This **approaches single-molecule sensitivity** reported, for example, by photothermally enhanced detection schemes [40], while offering a much higher detection bandwidth and the possibility of direct quantitative analysis. We note that the cavity is operated far away from the plasmon

resonance of gold nanospheres, so that the nanoparticles behave essentially like dielectrics: the 3 nm gold nanoparticles have polarisability $\Re(\alpha)$ equivalent to a 8 nm silica sphere.

Due to the low SNR in the cavity transmission signal produced by smaller nanoparticles ($d < 10$ nm), autocorrelation-based thresholding was employed to automatically identify nanoparticle events in measured traces. This was found to be a substantially more sensitive method to detect particles than a direct analysis of the signal. For example, the SNR between the autocorrelation amplitude of 3 nm nanoparticle events and the background correlation was around 2 even when the particle event was not directly visible within the background noise. The sensitivity of the sensor in its current form was estimated to be limited by the background noise correlation to particles about 2 nm in diameter.

The rotation of nanorods. Since nanoparticles of interest, especially biomolecules, are seldom spherical, the nanosensor was also used to detect gold nanorods and investigate their dynamics. In particular, the high-speed measurement capability of this nanosensor was exploited to record the **rotational motion** of single CTAB-stabilised nanorods with lengths between 15 nm and 25 nm with a temporal resolution of ~ 20 ns. Similarly to the approach for nanospheres outlined above, the autocorrelation of nanorod events was used to extract information about the diffusivity of the particle. In the case of an anisotropic nanoparticle, two quantities could be extracted: the diffusion coefficient D_T and the rotational diffusion coefficient D_R, which enable the determination of not only a single effective hydrodynamic dimension, but explicitly of the **length and the diameter** of the nanorod. In the current measurements of nanorods, a systematic error was observed in determination of the rotational diffusion coefficient, suggesting that the autocorrelation model employed here may need modification when applied to the cavity geometry.

Furthermore, a scheme for the simultaneous measurement of orthogonal polarisation modes in the cavity (ROSHANI) was developed, which enabled the **orientation of a single diffusing nanorod** to be tracked, also with a temporal resolution of ~ 20 ns. This approach and its high detection bandwidth could offer an insight not only into rotational dynamics, but also conformational changes such as folding of biomolecules.

In a slight excursion from traditional nanosensing, preliminary experiments were performed in which a nanorod was intentionally trapped in the cavity mode field. Due to the linearly polarised nature of the cavity mode, the rod could not only be spatially confined to a field maximum, but also orientationally aligned to the polarisation direction, enabling **trapping in five degrees of freedom**. Due to cavity amplification, relatively small laser powers were required to achieve trapping. While optical trapping was not studied in detail in this work, the capability to spatially (and orientationally) confine particles in the cavity could add functionality to the nanosensor, for instance, by allowing a host or probe particle to be immobilised in the cavity, and measuring the interaction of nanoparticles in a sample with it, or by repeatedly drawing a particle into the optical field for repeated measurement and improved statistics.

Biosensing. In a step towards applying the nanoparticle sensor described so far to biosensing, biological samples were investigated as well. **Single DNA "origami" nanobundles** were sensed, and a hydrodynamic radius was determined which matched well with theoretical expectations. Additionally, a decay in the signal autocorrelation at small (sub-microsecond) timescales suggested the presence of another dynamical process apart from rotation and diffusion, and demonstrates that the high-bandwidth sensing capability of this sensor could enable the investigation of various **dynamic processes at the nanoscale**.

Furthermore, ensembles of down to ~ 10 BSA **protein molecules** were sensed and measured, and their diffusion coefficients extracted and compared for different concentrations. The values thus obtained match with calculations and values reported in the literature.

Further possibilities. The work done here already enables us to get an insight into the world of single nanoparticles in a manner not possible using other state-of-the-art techniques available today. However, it is far from exhaustive, and several exciting possibilities for cavity-enhanced sensing remain to be discovered and investigated. An initial advancement of the current system could focus on improving the SNR of small nanoparticle events, to allow the detection of even single unlabelled molecules on the ~ 1 nm scale. Also, the automation of data acquisition and evaluation will allow the collection of larger amounts of data for richer statistics, and increase the efficiency of sensing experiments by reducing operator involvement [105]. In the longer term, as mentioned above, adding trapping capabilities to the sensor could allow interactions and processes to be studied which cannot be measured by "passive" sensing. Finally, the flexibility of the fibre-based Fabry-Perot cavity can be exploited to produce sensor cavity geometries specifically suited for certain applications, such as a surface-scanning cavity [42] or a microcavity within a single liquid droplet, capable of sensing with ultra-small sample volumes.

With the capabilities and developments presented in this thesis, as well as the possibility for further optimisation for specific applications, the optofluidic microcavity promises to offer deeper insights into the world of nanomaterials in a variety of fields of science and technology. As demonstrated by preliminary measurements of proteins and single DNA nanostructures, for example, it could be of considerable biological interest for the investigation of biochemical processes on the nanoscale.

Appendices

A. DLS and TEM measurements

This section discusses the nanoparticle measurements performed by DLS and TEM in some more depth.[1]

DLS measurements. A Malvern Instruments ZetaSizer Nano ZS equippped with a 633 nm laser was used to do DLS measurements of the gold nanospheres in backscattering mode at 173°. Measurements were done with approximately 1 mL of ultrasonicated stock solution (~ 0.06 mg/mL) with automatic attenuator settings.

The quantity directly measured by DLS is the intensity-weighted size distribution. Number- or volume-weighted distributions can be calculated from this via Mie theory. [21] Figure A.1 shows the size distribution curves of nanospheres from 3 nm to 20 nm in intensity- and number-normalised form. As mentioned in the main text, the intensity-weighted distribution (dashed curves) typically skews the distribution towards larger sizes, since scattered intensity is proportional to R^6. This is particularly significant for the smallest particles, for which additional peaks at ~ 100 nm (possibly due to agglomerations or dust particles) are comparable or even stronger than the actual particle size. Therefore, we used the number-weighted distributions (solid curves) for comparison with microcavity measurements.

TEM measurements. A very dilute suspension of nanospheres was drop-casted onto a carbon-coated 400 µm copper mesh for TEM analysis. Images were obtained with a FEI Osiris transmission electron microscope under accelerating voltage 200 kV. Sample TEM images are shown in Figure A.2 (a) and (c). A significant heterogeneity in particle size and shape can be seen in these images.

Size analysis was performed using the "Analyse particles" function in ImageJ, and the detected nanoparticles are shown in Figure A.2 (b) and (d). These measurements resulted in size distributions of (10 ± 2) nm and (15.9 ± 1.4) nm respectively. Outliers arising from clusters of single nanoparticles were manually excluded. Since TEM was performed with dried samples, we cannot draw conclusions about possible agglomeration of nanoparticles, which could form such clusters, in aqueous suspension.

[1] I am grateful to Christian Ritchel for the DLS measurements and to Christian Ritschel and Jens Treptow for the TEM measurements, both at the Institute of Inorganic Chemistry (AOC) at KIT.

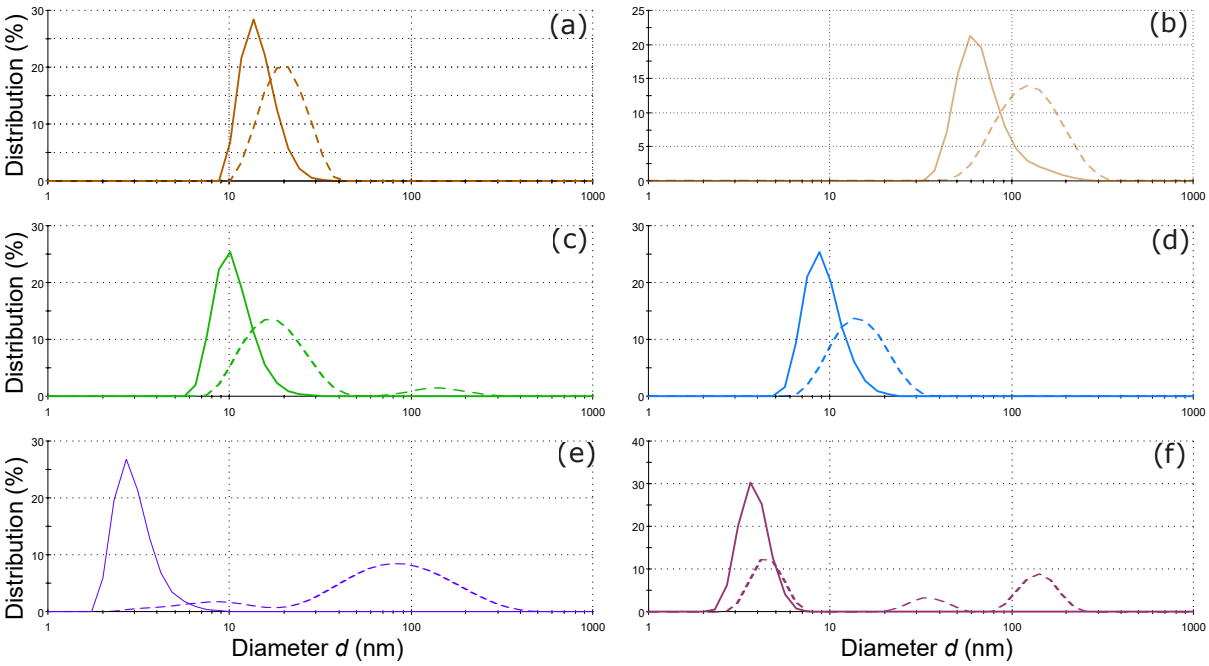

Figure A.1: Size distributions of nanospheres measred by DLS. Number-weighted distributions are shown with solid lines and intensity-weighted distributions dotted. The nominal sizes are (a), (b) 20 nm, (c) 15 nm, (d) 10 nm, (e) 5 nm and (f) 3 nm. All particles were stabilised in citrate except (b) which were in CTAB.

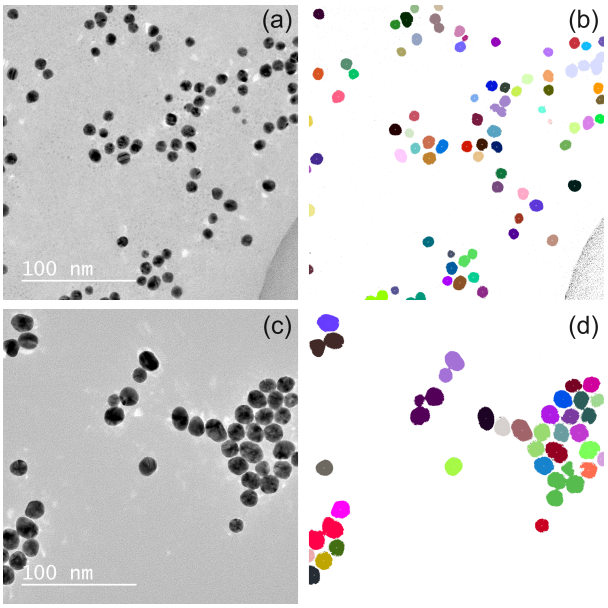

Figure A.2: (a), (b) Raw TEM images of gold nanospheres with nominal diameters of 10 nm and 20 nm resepctively. (c), (d) Detected particles from (a) and (b) for size analysis.

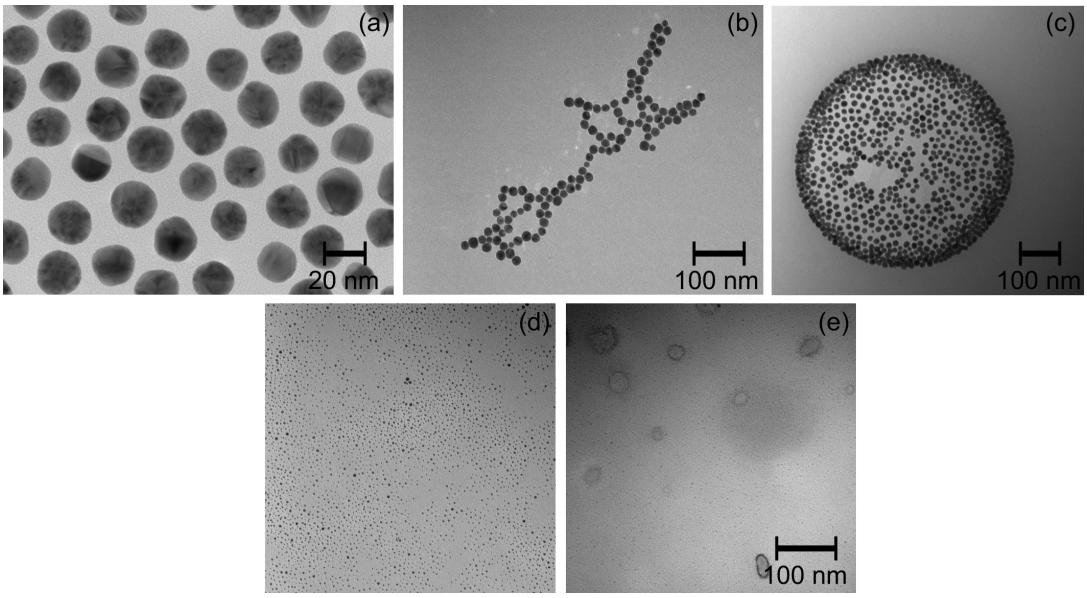

Figure A.3: TEM images of gold nanospheres with specified diameters (a) 20 nm, (b) 15 nm, (c) 10 nm, (d) 5 nm and (e) 3 nm provided by the manufacturer, Nanopartz Inc. [100]

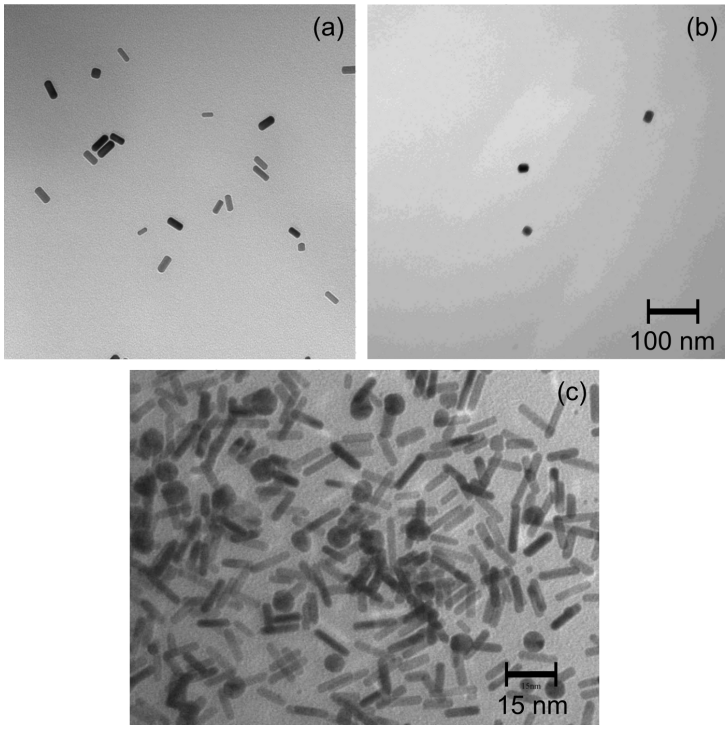

Figure A.4: TEM images of gold nanorods of samples (a) "650", (b) "600" and (c) "700" provided by the manufacturer, Nanopartz Inc. [124]

Images from the manufacturer. Figures A.4 and A.3 show TEM images of gold nanorods provided by the manufacturer. A significant heterogeneity in size and shape of the particles is visible, which may have played a large role in the unexpected results seen in Section 5.2.2. In particular, sample "700" shows nanorods with aspect ratios ranging from ≈ 3 to ≈ 8, as well as some spherical particles, which were also observed in our measurements.

B. Examples of single nanoparticle events

Figure B.1 presents some examples of individual nanoparticle events and their autocorrelations.

In particular, we observe the variation in particle traces due to individual nanoparticle transits in the cavity. While those shown in Figure B.1 (a) and (c) feature single transits lasting about 50 ms, the nanoparticles recorded in (e) and (g) re-enter the cavity field within the measurement time.

As mentioned in the main text, the autocorrelation of such events provides sufficient statistics for sizing at short lag times (the region used for fitting is shown with a solid crimson curve), and at longer lag times, the uniqueness of each particle event reduces the statistical statistical strength of the measurement. This is seen in Figures 4.6 and 4.8, where the autocorrelation curves diverge from each other after around $\tau \sim 10^{-4}$ s, and features in the individual autocorrelations at large τ yield insights into the nanoparticle behaviour via the autocorrelation itself. Some examples of nanoparticle traces and their autocorrelations are shown in Figure B.1. Here, the traces in (a) and (c) yield autocorrelations (b) and (d) closely resembling the analytical ACF even at longer lag times (crimson, dotted). The autocorrelations plotted in (f) and (h) of events with multiple transits through the cavity ((e) and (g) respectively) show additional bumps around 50 ms. These are indicative of repetition or periodicity in the signal, and occur on the time scale of the separation between single cavity interactions.

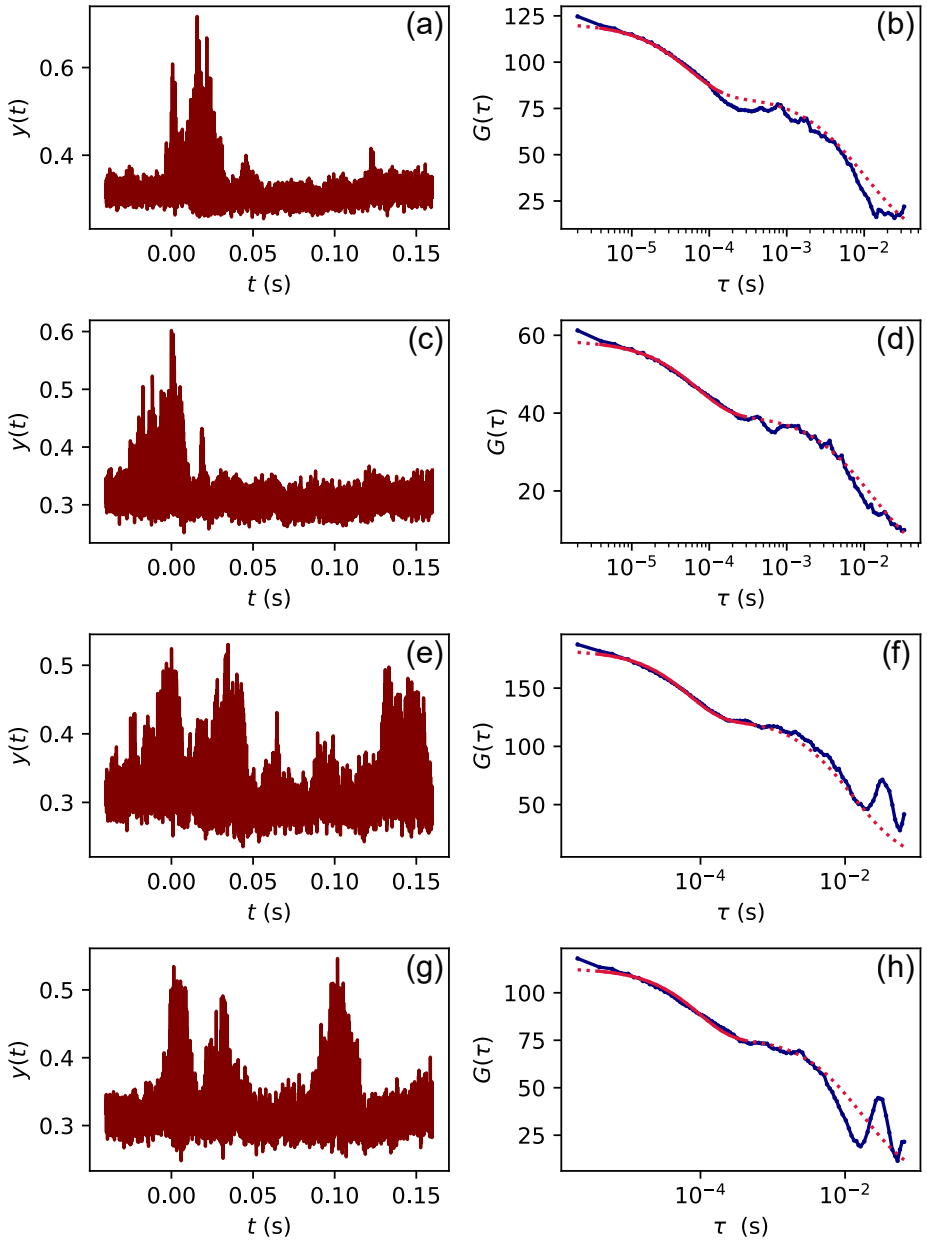

Figure B.1: Examples of single-nanoparticle events with 20 nm gold nanospheres. The normalised transmission traces are on the left and the corresponding autocorrelations (dark blue) with fits to $G_{\mathrm{SW}}(\tau)$ (crimson) on the right. Fitting is performed over the solid curve, and the extrapolation of $G_{\mathrm{SW}}(\tau)$ is shown dotted.

C. Practical notes for handling a fibre-fibre microcavity

C.1. Troubleshooting guide

No cavity transmission	• Check electrical connections, APD on length scan on. • Check fibre connectors for dirt, or whether the fibre has slipped back or broken in the connector (even if it looks fine in the fiberscope!). • After successful experiments: increase cavity length with micropositioner. The fibre may have moved beyond the shortest resonance. • Temporary connector ferrule polished down too far. Compare with a new one and change if necessary (Thorlabs B30126A9).
No signal in spectrometer	• Check connections and removable mirrors. • Check camera exposure time (> 20 ms). • Check area of interest (y-coordinate) in the spectrometer GUI.
Low signal in Red Pitaya	• Tighten electrical connections. A "derivative" shape indicates a capacitance between BNC connectors. • Reduce scan amplitude. The Red Pitaya doesn't like broad scans.

Low transmission, strong transverse modes, large polarisation splitting	• Try rotating the cavity fibre(s). • Severe misalignment: check the height of the clamps (both sides!), see Figure C.1. Add height (glue PEEK film, *not* sticky tape) or file down the clamp as needed.
Insufficient scan range (less than one FSR, or micropositioner needed to see resonances)	• Check that the PZTs work (capacitance = 1.7 nF, continuity to cable connectors). • Is a non-rigid layer being used for clamp height adjustment (e.g. sticky tape)? Remove it and glue a PEEK film instead. • Something sticky has gotten into the ferrule bore. Clean thoroughly.
Unusually bad cavity stability	• Air bubbles in the cavity? Flush with liquid. • Wiggle BNC connectors (up to 100 fm improvement!).
Fibre gets stuck while entering ferrule	• Metal coating remains: try stripping with $FeCl_3$, if it doesn't help use HCl to dissolve oxidised copper.

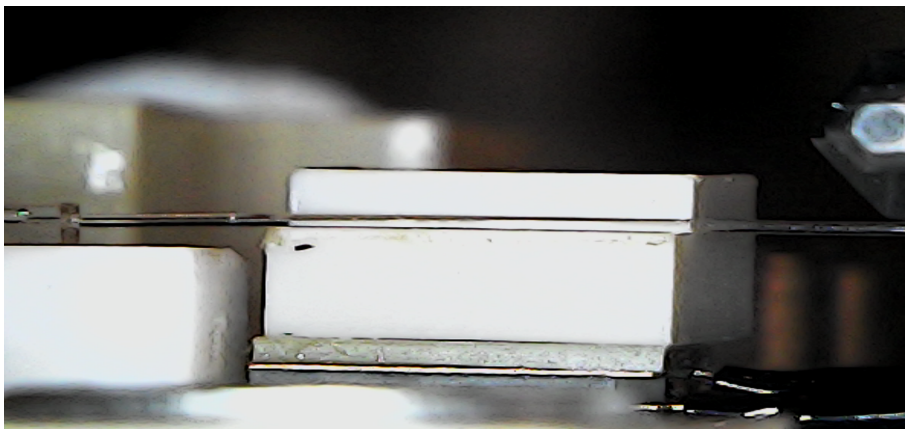

Figure C.1: A side view of the fibre clamp shows whether the height is correct.

C.2. Fibre cleaning procedures

Dirty cavity fibres are a steadfast companion of the operator of a fibre-based optofluidic microcavity. However, thanks to the fully disassembleable design of the setup, fibres can be removed, cleaned and brought back to a condition almost as good as new. Four cleaning procedures are outlined here, which have proven effective against various sources and types of contamination.

- **Ultrasonication.** Perhaps the simplest method to remove loose, coarse dirt from a fibre end-facet is ultrasonication, in which the fibre tip is immersed in a liquid in an ultrasound bath for a few minutes. In previous work, dilute hydrochloric acid was used to dislodge aggregations of silica nanoparticles [47]; however, this is not to be used with gold samples, since it causes the opposite effect: gold particles get firmly bound to the fibre surface. Gold residue must then be etched away with gold etchant, e.g. KI_3 solution. In this work, ethanol was used as the ultrasonication medium with satisfactory results.
- **Physical wiping.** While the practicality of physically wiping the end facet of an optic fibre clean is not necessarily intuitive, this was possibly the most effective cleaning method used in this work. The fibre was examined in the microscope or interferometer of the fibre shooting setup, and a wedge-shaped piece of lens-cleaning tissue moistened with ethanol was rubbed back and forth along the end-facet, perpendicular to the fibre. Obviously, care must be taken not to snap the protruding fibre, but in the author's experience, the fibres proved to be astonishingly robust, and no fibres were broken in this way (!). Initial wipes get rid of large bits of dirt, and persistent scrubbing in the same way can even dislodge the smallest offending matter on the fibre mirrors. A further advantage of this method is its rapidness and immediate results.
- **Cleaning polymer.** Optics cleaning polymers are designed to clean large optical surfaces like lenses; however, a micromirror can also benefit from them. A drop of cleaning polymer[1] was placed on a clean, vertically mounted glass slide, and the dirty fibre, mounted on a three-axis positioning stage, was slowly driven into the drop. Its position should be monitored with a microscope from above to avoid damaging the tip. Correct vertical alignment was obtained by observing the reflection of the fibre in the polymer drop (see Figure C.2). After a drying time of about 20 minutes, the cleaned fibre was retracted.
- **Piranha cleaning.** This is the least appealing and most aggressive method, but is suited for removing even traces of organic residues on the fibre tips. Piranha solution was prepared with $3:1$ $H_2SO_4 : H_2O_2$ [125] and a few millimetres of the fibre tip were immersed into the solution for a minute (or more). The acidic solution is capable of stripping metal coatings! Finally, the fibre should be rinsed with water. Obviously, every precaution must be taken to ensure the safety of this procedure and avoid an explosion due to unstable piranha solution!

To reduce the frequency of a cavity failing due to dirt, the operator is advised to thoroughly rinse the cavity with water and/or ethanol after experiments with nanoparticles. When the cavity is left underwater for extended periods, the water can dry up and leave residues on the

[1] First Contact cleaning polymer

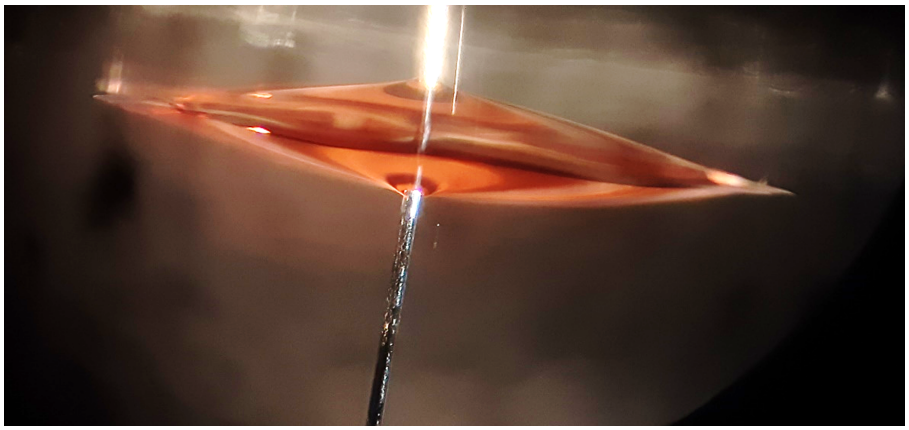

Figure C.2: Top view of a fibre tip being cleaned with a drop of First Contact cleaning polymer. The reflection of the fibre in the drop surface is used for alignment.

mirrors. Instead, it is advisable to flush out water with pure ethanol and then flash dry the channel and mirrors with clean pressurised air.

D. Optofluidic lasing

The nanoparticle sensor described in this work employs the reactive sensing principle (2.3) to detect "passive" particles, i.e. species which do not produce their own light. Within the scope of the Collaborative Research Centre (CRC) "4f for Future", work was undertaken by supervised Masters and Bachelors students towards the development of an **optofluidic microlaser** for sensitive biochemical sensing using europium-doped inorganic-organic hybrid (IOH) nanoparticles inside the cavity [126, 127]. This section shall provide a brief overview of the developments and results of this project in our group.

The motivation to use lanthanides comes from the optical properties offered by their 4f-4f transitions, such as narrow emission linewidths and long excited lifetimes and, in the context of the CRC project C4, the possibility to investigate lanthanide-dependant biochemical processes such as the metabolism of certain species of bacteria. Binding a lanthanide ion within an IOH nanoparticle enables energy transfer from the ligand to the ion [128], and additionally shields the ion from water-based quenching processes, hence allowing its emission to be investigated in an aqueous environment. Using such nanoparticles as the gain medium in an optofluidic laser could serve as a highly sensitive platform to monitor the concentration of lanthanides in the suspension via its effect on the lasing threshold and laser emission.

As a proof of concept, a microfluidic laser was built by Mustafa Gerdan in a supervised Masters thesis. It was based on the same optofluidic platform as that used for nanosensing, with rhodamine 6G dissolved in ethanol as the gain medium and green (532 nm) pump light [126]. Lasing was successfully demonstrated, and the dependence of the lasing threshold on gain medium concentration was investigated. Meanwhile, the physical and optical characteristics of various europium-based IOH nanoparticle species synthesised by the group of Prof. Claus Feldmann (AOC, KIT) were investigated by confocal microscopy and spectroscopy. A promising candidate is the 1-hydroypyridine-2-one (HOPO) ligand, which shows good colloidal stability, adequate emission and suitability for uptake by the methylotrophic bacteria cultured by the group of Prof. Lena Daumann (Heinrich Heine University, Dusseldorf).

Preliminary attempts to generate laser light with HOPO-based IOH nanoparticles have been made with ultraviolet excitation[1], designed to coincide with the absorption band of the organic ligands. Recently, Jannis Hessenauer detected intense red fluorescence from HOPO-based IOH complexes dissolved in methanol and excited by ultraviolet light (355 nm) with the same setup, shown in Figure D.2.

[1] Teem Photonics SNV-40P-100 emitting at 355 nm

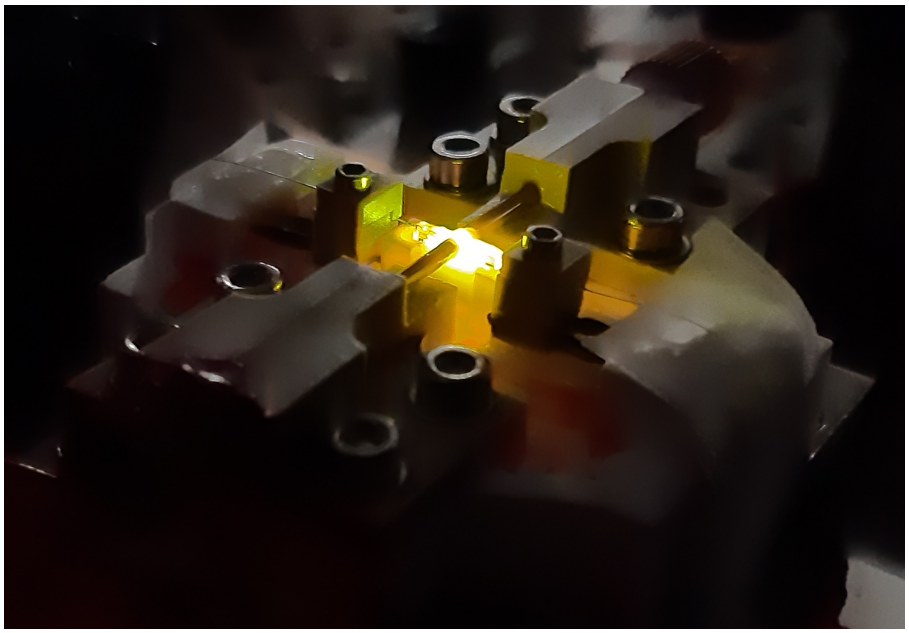

Figure D.1: An optofluidic microlaser in operation with rhodamine 6G as its gain medium. [126]

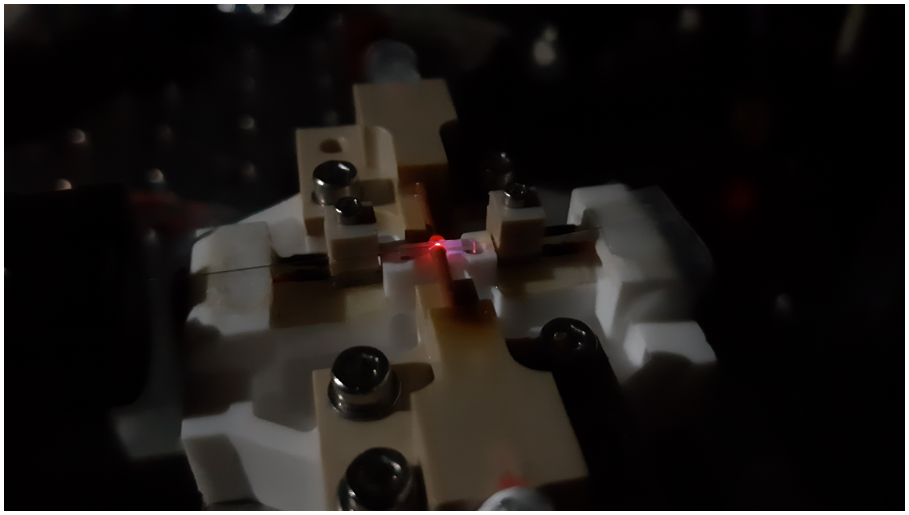

Figure D.2: Fluorescence of HOPO-based IOH-complexes in a microcavity with an ultraviolet pump.

E. List of acronyms

ACF	Autocorrelation function
AFG	Arbitrary function generator
APD	Avalanche photodiode
BSA	Bovine serum albumin
CIT	Citrate ($C_3H_5O(COO)_3^{3-}$)
CTAB	Cetyltrimethylammonium bromide ($(C_{16}H_{33})N(CH_3)_3Br$)
DBR	Distributed Bragg reflector
DLS	Dynamic light scattering
EOM	Electro-optic modulator
FCS	Fluorescence correlation spectroscopy
FPGA	Field programmable gate array
FSR	Free spectral range
FWHM	Full-width at half maximum
HB	Helix bundle
HOPO	1-Hydroypyridine-2-one
HWP	Half-wave plate
IOH	Inorganic-organic hybrid
iSCAT	Interference scattering microscopy
MSAD	Mean squared angular displacement
MSD	Mean squared displacement
ND	Neutral density
PBS	Polarising beam-splitter
PEEK	Polyether ether ketone
PID	Proportional-integration-derivative
PZT	Piezo-electric transducer
QWP	Quarter-wave plate
RF	Radio frequency
RMS	Root-mean-square
ROSHANI	Rotation Observation with a Stabilised High-Bandwidth Apparatus for Nanoparticle Investigation
SEM	Scanning electron microscopy
SLED	Superluminiscent light emitting diode
SNR	Signal-to-noise ratio
STED	Stimulated emission depletion
SW	Standing wave
TAE	Tris-acetate EDTA
TEM	Transmission electron microscopy
UGF	Unity-gain frequency
WGM	Whispering gallery mode

F. List of symbols

The following list summarises selected symbols used in this work.

$\mathcal{A}$	Absorption in cavity
α	Absorption coefficient (Section 2.1 only)
α	Polarisability of nanoparticle
$\mathbf{B}$	Magnetic field
C	Nanoparticle concentration
c_0	Speed of light in vacuum
d	Nanorod diameter
δ	Penetration depth
$\Delta(\theta)$	Geometric birefringence as a function of mirror rotation angle
$\delta\tau$	Smallest lag time, equal to measurement time resolution
D_R	Rotational diffusion coefficient
D_T	Diffusion coefficient
$\mathbf{E}$	Electric field
ε	Mode coupling efficiency (Section 2.1 only)
$\varepsilon(\omega)$	Relative permittivity
ε_0	Permittivity of free space
η	Viscosity of water
$\mathcal{F}$	Finesse
$\mathcal{G}_q(z)$	Series of q Gaussians
$G(\tau)$	Autocorrelation function
I	Optical intensity
k	Wavenumber, $2\pi/\lambda$
k_B	Boltzmann constant
ℓ	Cavity length (geometric)
$\mathcal{L}$	Losses
$\mathscr{L}$	Depolarisation factor
L	Nanorod length
$\lambda_0,\ \lambda_\mathrm{m}$	Wavelength of light in vacuum and in the cavity medium
n_m	Refractive index of the cavity medium
$\Delta\nu_\mathrm{pol}$	Polarisation mode spacing
$\Delta\nu_\mathrm{transverse}$	Transverse mode spacing
ν_q	Resonance frequency of the q^th fundamental mode
ν_{qlm}	Resonance frequency of the (l, m) transverse mode
P	Optical power

p	Aspect ratio of nanorod
$\Delta\Phi$	3D angular step
ϕ	Azimuthal angle
$\mathcal{R}$	Reflectivity of mirror
R	Nanoparticle radius
$R(z)$	Radius of curvature of Gaussian wavefronts
R_j	Radius of curvature of mirror j
$\mathcal{S}$	Scattering at mirror
$\Psi(\theta)$	Polarisation mode orientation as a function of mirror rotation angle
σ	Standard deviation / RMS amplitude
σ_{abs}	Absorption cross-section
σ_{ext}	Extinction cross-section
σ_{sca}	Scattering cross-section
$\mathcal{T}$	Transmittivity of mirror
T	Absolute temperature (in the context of diffusion coefficients)
T	Cavity transmission (in the context of cavity optics)
τ	Group delay (Section 2.2 only)
τ	Lag time for autocorrelation
τ_{res}	Photon lifetime in a resonator
θ	Polar angle (Chapter 5)
T_{seg}	Length of nanoparticle event segments
U	Optical trap strength
V_{m}	Mode volume of cavity
V_{NP}	Volume of nanoparticle
V_{peak}	Peak voltage at resonance
$W(x, y, z)$	Cavity mode intensity distributions (e.g. FCS or standing wave)
w_0	Beam waist
$\xi(t)$	Error signal from cavity lock
$\xi(z)$	Gouy phase
$y(t)$	Cavity transmission signal
z_0	Rayleigh length

List of Figures

List of Tables

Bibliography

[1] R. Hook, *Micrographia*. J. Martyn and J. Allestry, 1965.

[2] S. Anu Mary Ealia and M. P. Saravanakumar, "A review on the classification, characterisation, synthesis of nanoparticles and their application", *IOP Conference Series: Materials Science and Engineering*, vol. 263, no. 3, p. 032 019, Nov. 2017. DOI: 10.1088/1757-899X/263/3/032019.

[3] T. Eichhorn *et al.*, "Multimodal Purcell enhancement and optical coherence of Eu3+ ions in a single nanoparticle coupled to a microcavity", *Nanophotonics*, vol. 14, no. 11, pp. 1817–1826, 2025. DOI: 10.1515/nanoph-2024-0721.

[4] F. E. Wagner, S. Haslbeck, L. Stievano, S. Calogero, Q. A. Pankhurst, and K. P. Martinek, "Before striking gold in gold-ruby glass", *Nature*, vol. 407, no. 6805, pp. 691–692, Oct. 2000. DOI: 10.1038/35037661.

[5] M. Reibold, P. Paufler, A. Levin, W. Kochmann, N. Pätzke, and D. Meyer, "Carbon nanotubes in an ancient Damascus sabre", *Nature*, vol. 444, 286 2006. DOI: 10.1038/444286a.

[6] S. S. Raut, R. Singh, and U. M. Lekhak, "Naturally occurring nanoparticles (NONPs): A review", *Next Sustainability*, vol. 3, p. 100 037, 2024, ISSN: 2949-8236. DOI: 10.1016/j.nxsust.2024.100037.

[7] V. K. Sharma, J. Filip, R. Zboril, and R. S. Varma, "Natural inorganic nanoparticles – formation, fate, and toxicity in the environment", *Chem. Soc. Rev.*, vol. 44, pp. 8410–8423, 23 2015. DOI: 10.1039/C5CS00236B.

[8] H. P. Erickson, "Size and shape of protein molecules at the nanometer level determined by sedimentation, gel filtration, and electron microscopy", *Biological Procedures Online*, vol. 11, no. 1, pp. 32–51, May 2009. DOI: 10.1007/s12575-009-9008-x.

[9] J. W. Dear, J. M. Street, and M. A. Bailey, "Urinary exosomes: A reservoir for biomarker discovery and potential mediators of intrarenal signalling", *PROTEOMICS*, vol. 13, no. 10-11, pp. 1572–1580, 2013. DOI: 10.1002/pmic.201200285.

[10] B. Pérez-Cabezas *et al.*, "More than just exosomes: Distinct leishmania infantum extracellular products potentiate the establishment of infection", *Journal of Extracellular Vesicles*, vol. 7, no. 1, p. 1 541 708, 2018. DOI: 10.1080/20013078.2018.1541708.

[11] S. Moghassemi *et al.*, "Extracellular vesicles in nanomedicine and regenerative medicine: A review over the last decade", *Bioactive Materials*, vol. 36, pp. 126–156, 2024. DOI: 10.1016/j.bioactmat.2024.02.021.

[12] J. Louten, "Chapter 2 – Virus structure and classification", in *Essential Human Virology*, Boston: Academic Press, 2016, pp. 19–29, ISBN: 978-0-12-800947-5. DOI: 10.1016/B978-0-12-800947-5.00002-8.

[13] R. Pati, M. Shevtsov, and A. Sonawane, "Nanoparticle vaccines against infectious diseases", *Frontiers in Immunology*, vol. Volume 9 - 2018, 2018. DOI: 10.3389/fimmu.2018.02224.

[14] S. Sellner, S. Kocabey, K. Nekolla, F. Krombach, T. Liedl, and M. Rehberg, "DNA nanotubes as intracellular delivery vehicles in vivo", *Biomaterials*, vol. 53, pp. 453–463, 2015. DOI: 10.1016/j.biomaterials.2015.02.099.

[15] M. Pilo-Pais, G. P. Acuna, P. Tinnefeld, and T. Liedl, "Sculpting light by arranging optical components with DNA nanostructures", *MRS Bulletin*, vol. 42, no. 12, pp. 936–942, Dec. 2017, ISSN: 1938-1425. DOI: 10.1557/mrs.2017.278.

[16] N. Liu and T. Liedl, "DNA-assembled advanced plasmonic architectures", *Chemical Reviews*, vol. 118, no. 6, pp. 3032–3053, 2018. DOI: 10.1021/acs.chemrev.7b00225.

[17] M. Dass, F. N. Gür, K. Kołątaj, M. J. Urban, and T. Liedl, "DNA origami-enabled plasmonic sensing", *The Journal of Physical Chemistry C*, vol. 125, no. 11, pp. 5969–5981, 2021. DOI: 10.1021/acs.jpcc.0c11238.

[18] L. V. de Broglie, "On the theory of quanta", Translated by A.F. Kracklauer, 2004, Ph.D. dissertation, University of Paris, 1924.

[19] E. Ruska, "The emergence of the electron microscope: Connection between realization and first patent application, documents of an invention", *Journal of Ultrastructure and Molecular Structure Research*, vol. 95, no. 1, pp. 3–28, 1986, ISSN: 0889-1605. DOI: 10.1016/0889-1605(86)90025-X.

[20] M. Malatesta, "Transmission electron microscopy for nanomedicine: Novel applications for long-established techniques", *European Journal of Histochemistry*, vol. 60, no. 4, Dec. 2016. DOI: 10.4081/ejh.2016.2751.

[21] Z. Guo and X. Li, *A practical guide to nanoparticle characterisation by light scattering techniques*. Bettersize Instruments Ltd., 2023.

[22] S. W. Hell and J. Wichmann, "Breaking the diffraction resolution limit by stimulated emission: Stimulated-emission-depletion fluorescence microscopy", *Optics Letters*, vol. 19, no. 11, pp. 780–782, Jun. 1994. DOI: 10.1364/OL.19.000780.

[23] F. Balzarotti *et al.*, "Nanometer resolution imaging and tracking of fluorescent molecules with minimal photon fluxes", *Science*, vol. 355, no. 6325, pp. 606–612, Feb. 2017, ISSN: 1095-9203. DOI: 10.1126/science.aak9913.

[24] F. Vollmer and S. Arnold, "Whispering-gallery-mode biosensing: Label-free detection down to single molecules", *Nature Methods*, vol. 5, no. 7, pp. 591–596, Jun. 2008, ISSN: 1548-7105. DOI: 10.1038/nmeth.1221.

[25] B. J. Berne and R. Pecora, *Dynamic Light Scattering: With Applications to Chemistry, Biology, and Physics*. Courier Corporation, 2013.

[26] N. S. Ginsberg, C.-L. Hsieh, P. Kukura, M. Piliarik, and V. Sandoghdar, "Interferometric scattering microscopy", *Nature Reviews Methods Primers*, vol. 5, no. 1, pp. 1–21, Apr. 2025, Publisher: Nature Publishing Group. DOI: 10.1038/s43586-025-00391-1.

[27] M. Piliarik and V. Sandoghdar, "Direct optical sensing of single unlabelled proteins and super-resolution imaging of their binding sites", *Nature Communications*, vol. 5, no. 1, p. 4495, Jul. 2014, Publisher: Nature Publishing Group. DOI: 10.1038/ncomms5495.

[28] M. Dahmardeh, H. M. Dasterji, H. Mazal, H. Köstler, and V. Sandoghdar, "Self-supervised machine learning pushes the sensitivity limit in label-free detection of single proteins below 10 kda", *Nature Methods*, vol. 20, pp. 442–447, 2023. DOI: 10.1038/s41592-023-01778-2.

[29] K. Kasaian, M. Mazaheri, and V. Sandoghdar, "Long-range three-dimensional tracking of nanoparticles using interferometric scattering microscopy", *ACS Nano*, vol. 18, no. 44, pp. 30 463–30 472, 2024. DOI: 10.1021/acsnano.4c08435.

[30] A. D. Kashkanove, M. Blessing, A. Gemeinhardt, D. Soulat, and V. Sandoghdar, "Precision size and refractive index analysis of weakly scattering nanoparticles in polydispersions", *Nature Methods*, vol. 19, pp. 586–593, 2022. DOI: 10.1038/s41592-022-01460-z.

[31] M. D. Baaske, P. S. Neu, and M. Orrit, "Label-free plasmonic detection of untethered nanometer-sized brownian particles", *ACS Nano*, vol. 14, no. 10, pp. 14 212–14 218, 2020. DOI: 10.1021/acsnano.0c07335.

[32] N. Asgari, M. D. Baaske, J. Ton, and M. Orrit, "Exploring rotational diffusion with plasmonic coupling", *ACS Photonics*, vol. 11, no. 2, pp. 634–641, 2024. DOI: 10.1021/acsphotonics.3c01482.

[33] N. Asgari, M. D. Baaske, and M. Orrit, "Burst-by-burst measurement of rotational diffusion at nanosecond resolution reveals hot-Brownian motion and single-chain binding", *ACS Nano*, vol. 17, no. 13, pp. 12 684–12 692, 2023. DOI: 10.1021/acsnano.3c03392.

[34] J. W. S. Rayleigh, *The theory of sound*. Dover Publications, 1878, vol. 2.

[35] F. Vollmer and L. Yang, "Label-free detection with high-Q microcavities: A review of biosensing mechanisms for integrated devices", *Nanophotonics*, vol. 1, p. 267, 2012.

[36] F. Vollmer, S. Arnold, and D. Keng, "Single virus detection from the reactive shift of a whispering-gallery mode", *Proceedings of the National Academy of Sciences*, vol. 105, no. 52, pp. 20 701–20 704, 2008. DOI: 10.1073/pnas.0808988106.

[37] J. Zhu, S. K. Ozdemir, Y.-F. Xiao, L. Li, L. He, and L. Chen Da-Renand Yang, "On-chip single nanoparticle detection and sizing by mode splitting in an ultrahigh-Q microresonator", *Nature Photonics*, vol. 4, pp. 46–49, 2010. DOI: 10.1038/nphoton.2009.237.

[38] C. Fabry and A. Perot, "On a new form of interferometer", *The Astrophysical Journal*, vol. 13, p. 265, May 1901. DOI: 10.1086/140817.

[39] LIGO Caltech, *LIGO's interferometer*, https://www.ligo.caltech.edu/page/ligos-ifo.

[40] L.-M. Needham *et al.*, "Label-free detection and profiling of individual solution-phase molecules.", *Nature*, vol. 629, pp. 1062–1068, 8014 May 2024. DOI: 10.1038/s41586-024-07370-8.

[41] L. Kohler, M. Mader, C. Kern, M. Wegener, and D. Hunger, "Tracking Brownian motion in three dimensions and characterization of individual nanoparticles using a fiber-based high-finesse microcavity", *Nature Communications*, vol. 12, p. 6385, 1 Nov. 2021. DOI: 10.1038/s41467-021-26719-5.

[42] M. Mader, "A scanning cavity microscope", Ph.D. dissertation, Ludwigs Maximilian University, Aug. 2018.

[43] A. A. P. Trichet, P. R. Dolan, D. James, G. M. Hughes, C. Vallance, and J. M. Smith, "Nanoparticle trapping and characterization using open microcavities", *Nano Letters*, vol. 16, no. 10, pp. 6172–6177, 2016. DOI: 10.1021/acs.nanolett.6b02433.

[44] D. Hunger, T. Steinmetz, Y. Colombe, C. Deutsch, T. W. Hänsch, and J. Reichel, "A fiber fabry–perot cavity with high finesse", *New Journal of Physics*, vol. 12, p. 65 038, 6 Jun. 2010. DOI: 10.1088/1367-2630/12/6/065038.

[45] M. Mader, J. Reichel, T. W. Hänsch, and D. Hunger, "A scanning cavity microscope", *Nature Communications*, vol. 6, no. 1, Jun. 2015, ISSN: 2041-1723. DOI: 10.1038/ncomms8249.

[46] M. Mader, J. Benedikter, L. Husel, T. W. Hänsch, and D. Hunger, "Quantitative determination of the complex polarizability of individual nanoparticles by scanning cavity microscopy", *ACS Photonics*, vol. 9, pp. 466–473, 2 Feb. 2022. DOI: 10.1021/acsphotonics.1c01131.

[47] L. Kohler, "Characterization and tracking of the three-dimensional translation motion and rotation of single nanoparticles using a fiber-based microcavity with high finesse", Ph.D. dissertation, Karlsruhe Institute of Technology, Jul. 2021.

[48] C. A. Saavedra Salazar *et al.*, "The origin of single-molecule sensitivity in label-free solution-phase optical microcavity detection", *ACS Nano*, vol. 19, no. 6, pp. 6342–6356, 2025. DOI: 10.1021/acsnano.4c16276.

[49] B. E. A. Saleh and M. C. Teich, *Fundamentals of Photonics*. Wiley, Aug. 1991, ISBN: 9780471839651. DOI: 10.1002/0471213748.

[50] T. Hümmer, "Cavity-enhanced hyperspectral Raman and absorption microscopy", Ph.D. dissertation, Ludwig-Maximilians-University, May 2019.

[51] J. Benedikter, T. Moosmayer, M. Mader, T. Hümmer, and D. Hunger, "Transverse-mode coupling effects in scanning cavity microscopy", *New Journal of Physics*, vol. 21, p. 103 029, 10 Oct. 2019. DOI: 10.1088/1367-2630/ab49b4.

[52] A. E. Siegman, *Lasers*. University Science Books, 1986, pp. 745–748.

[53] M. K. Kreysing, T. Kießling, A. Fritsch, C. Dietrich, J. R. Guck, and J. A. Käs, "The optical cell rotator", *Optics Express*, vol. 16, p. 16 984, 21 Oct. 2008. DOI: 10.1364/OE.16.016984.

[54] W. B. Joyce and B. C. DeLoach, "Alignment of Gaussian beams", *Applied Optics*, vol. 23, p. 4187, 23 Dec. 1984. DOI: 10.1364/AO.23.004187.

[55] J. Hessenauer, "Ytterbium ions and color centers in silicon carbide as cavity-integrated quantum nodes with near-infrared optical transitions", Ph.D. dissertation, Karlsruhe Institute of Technology, 2025.

[56] M. Fox, *Quantum Optics*. Oxford University Press, 2014, pp. 194–195.

[57] T. Eichhorn, "Cavity-enhanced spectroscopy of individual europium-doped nanoparticles", Ph.D. dissertation, Karlsruhe Institute of Technology, 2024.

[58] S. Garcia, F. Ferri, K. Ott, J. Reichel, and R. Long, "Dual-wavelength fiber fabry-perot cavities with engineered birefringence", *Optics Express*, vol. 26, p. 22 249, 17 Aug. 2018. DOI: 10.1364/OE.26.022249.

[59] E. Hecht, *Optics*, 5th ed. Pearson Education Limited, 2017, ISBN: 1-292-09693-4.

[60] P. Yeh, *Optical Waves in Layered Media*. John Wiley & Sons, Inc., 1988, ISBN: 0-471-82866-1.

[61] C. Koks and M. P. van Exter, "Microcavity resonance condition, quality factor, and mode volume are determined by different penetration depths", *Optics Express*, vol. 29, p. 6879, 5 Mar. 2021. DOI: 10.1364/OE.412346.

[62] L. University, *How deep is a mirror?*, https://www.universiteitleiden.nl/en/news/2021/03/how-deep-is-a-mirror, 2021.

[63] A. D. Rakić, A. B. Djurišić, J. M. Elazar, and M. L. Majewski, "Optical properties of metallic films for vertical-cavity optoelectronic devices", *Applied Optics*, vol. 37, no. 22, pp. 5271–5283, Aug. 1998. DOI: 10.1364/AO.37.005271.

[64] C. G. Granqvist and O. Hunderi, "Optical properties of ultrafine gold particles", *Phys. Rev. B*, vol. 16, pp. 3513–3534, 8 Oct. 1977. DOI: 10.1103/PhysRevB.16.3513.

[65] U. Kreibig and M. Vollmer, *Optical properties of metal clusters*. Springer, 1995, ISBN: 3540578366.

[66] O. L. Muskens, P. Billaud, M. Broyer, N. Del Fatti, and F. Vallée, "Optical extinction spectrum of a single metal nanoparticle: Quantitative characterization of a particle and of its local environment", *Physical Review B*, vol. 78, p. 205 410, 20 Nov. 2008. DOI: 10.1103/PhysRevB.78.205410.

[67] J. Tyndall, "On the blue colour of the sky, the polarization of skylight, and on the polarization of light by cloudy matter generally", *The London, Edinburgh, and Dublin Philosophical Magazine and Journal of Science*, vol. 37, no. 250, pp. 384–394, 1869. DOI: 10.1080/14786446908640164.

[68] J. W. Strutt, "On the light from the sky, its polarization and colour", *The London, Edinburgh, and Dublin Philosophical Magazine and Journal of Science*, vol. 41, no. 271, pp. 107–120, 1871. DOI: 10.1080/14786447108640452.

[69] J. W. S. Rayleigh, "On the electromagnetic theory of light", *The London, Edinburgh, and Dublin Philosophical Magazine and Journal of Science*, vol. 12, no. 73, pp. 81–101, 1881. DOI: 10.1080/14786448108627074.

[70] M. Quentin, *Optical properties of nanoparticle systems*. John Wiley & Sons, Ltd, 2011, ch. 4, pp. 55–74, ISBN: 9783527633135. DOI: 10.1002/9783527633135.

[71] C. F. Bohren and D. R. Huffman, *Absorption and scattering of light by small particles*. John Wiley & Sons, Ltd, 1993, ISBN: 9783527618156. DOI: 10.1002/9783527618156.ch1.

[72] H. C. v. d. Hulst, *Light scattering by small particles*. Dover Publications, 1981, ISBN: 0486642283.

[73] V. Amendola, R. Pilot, M. Frasconi, O. M. Marago, and M. A. Lati, "Surface plasmon resonance in gold nanoparticles: A review", *Journal of Physics: Condensed Matter*, vol. 29, p. 203 002, 20 Apr. 2017. DOI: 10.1088/1361-648X/aa60f3.

[74] G. Mie, "Beiträge zur Optik trüber Medien, speziell kolloidaler Metallösungen", *Annalen der Physik*, vol. 330, no. 3, pp. 377–445, 1908. DOI: 10.1002/andp.19083300302.

[75] L. S. Slaughter *et al.*, "Single-particle spectroscopy of gold nanorods beyond the quasi-static limit: Varying the width at constant aspect ratio", *Journal of Physical Chemistry*, vol. 114, 11 2010. DOI: 10.1021/jp101272w.

[76] R. Brown, "A brief account of microscopical observations made in the months of June, July and August 1827, on the particles contained in the pollen of plants; and on the general existence of active molecules in organic and inorganic bodies", *The Philosophical Magazine*, vol. 4, pp. 161–173, 21 Sep. 1828. DOI: 10.1080/14786442808674769.

[77] A. Fick, "On liquid diffusion", *The London, Edinburgh, and Dublin Philosophical Magazine and Journal of Science*, vol. 10, pp. 30–39, 63 Jul. 1855. DOI: 10.1080/14786445508641925.

[78] L. Sjögren, "Brownian motion", in *Stochastic processes*. University of Gothenburg. [Online]. Available: https://gu-statphys.org/media/mydocs/LennartSjogren/kap6.pdf.

[79] H. C. Berg, *Random Walks in Biology*. Princeton University Press, Nov. 1993, ISBN: 9781400820023. DOI: 10.2307/j.ctv7r40w6.

[80] S. Broersma, "Rotational diffusion constant of a cylindrical particle", *The Journal of Chemical Physics*, vol. 32, no. 6, pp. 1626–1631, Jun. 1960. DOI: 10.1063/1.1730994.

[81] S. Broersma, "Viscous force constant for a closed cylinder", *The Journal of Chemical Physics*, vol. 32, no. 6, pp. 1632–1635, Jun. 1960. DOI: 10.1063/1.1730995.

[82] W. Eimer and R. Pecora, "Rotational and translational diffusion of short rodlike molecules in solution: Oligonucleotides", *The Journal of Chemical Physics*, vol. 94, no. 3, pp. 2324–2329, Feb. 1991. DOI: 10.1063/1.459904.

[83] M. M. Tirado and J. G. de la Torre, "Translational friction coefficients of rigid, symmetric top macromolecules. application to circular cylinders", *The Journal of Chemical Physics*, vol. 71, no. 6, pp. 2581–2587, Sep. 1979. DOI: 10.1063/1.438613.

[84] M. M. Tirado, C. L. Martínez, and J. G. de la Torre, "Comparison of theories for the translational and rotational diffusion coefficients of rod-like macromolecules. application to short DNA fragments", *The Journal of Chemical Physics*, vol. 81, no. 4, pp. 2047–2052, Aug. 1984. DOI: 10.1063/1.447827.

[85] T. Wohland, R. Machan, and S. Maiti, *An Introduction to Fluorescence Correlation Spectroscopy*. IOP Publishing, 2020.

[86] E. L. Elson, "Fluorescence correlation spectroscopy: Past, present, future.", *Biophysical journal*, vol. 101, pp. 2855–70, 12 Dec. 2011. DOI: 10.1016/j.bpj.2011.11.012.

[87] B. Chu, *Laser Light Scatttering: Basic Principles and Practice*, 2nd ed. Academic Press, 1974.

[88] T. Weidemann, M. Wachsmuth, M. Tewes, K. Rippe, and J. Langowski, "Analysis of ligand binding by two-colour fluorescence cross-correlation spectroscopy", *Single Molecules*, vol. 3, no. 1, pp. 49–61, 2002. DOI: 10.1002/1438-5171(200204)3:1<49::AID-SIMO49>3.0.CO;2-T.

[89] S. Palkhivala, L. Kohler, C. Ritschel, C. Feldmann, and D. Hunger, "Accurate single-nanoparticle sizing down to 3 nm with an optofluidic microcavity", *ACS Nano*, 2025. DOI: https://doi.org/10.1021/acsnano.5c13782.

[90] F. Perrin, "Polarisation de la lumière de fluorescence. vie moyenne des molécules dans l'etat excité", *J. Phys. Radium*, vol. 7, no. 12, pp. 390–401, 1926. DOI: 10.1051/jphysrad:01926007012039000.

[91] R. Jain and K. L. Sebastian, "Diffusing diffusivity: Rotational diffusion in two and three dimensions", *The Journal of Chemical Physics*, vol. 146, no. 21, p. 214 102, Jun. 2017. DOI: 10.1063/1.4984085.

[92] R. Jones, *Rotational Diffusion in Dispersive Media*. Centre of Excellence for Advanced Materials and Structures, 2003, ch. 4.

[93] P. Kask, P. Piksarv, M. Pooga, Ü. Mets, and E. Lippmaa, "Separation of the rotational contribution in fluorescence correlation experiments", *Biophysical Journal*, vol. 55, no. 2, pp. 213–220, 1989. DOI: 10.1016/S0006-3495(89)82796-1.

[94] S. R. Aragón and R. Pecora, "Fluorescence correlation spectroscopy and brownian rotational diffusion", *Biopolymers*, vol. 14, no. 1, pp. 119–137, 1975. DOI: 10.1002/bip.1975.360140110.

[95] A. Loman, I. Gregor, C. Stutz, M. Mund, and J. Enderlein, "Measuring rotational diffusion of macromolecules by fluorescence correlation spectroscopy", *Photochem. Photobiol. Sci.*, vol. 9, pp. 627–636, 5 2010. DOI: 10.1039/B9PP00029A.

[96] J. Häberle, "Cavity-enhanced homodyne detection for sensing of individual nanosystems", Bachelor's Thesis, Karlsruhe Institute of Technology, Jul. 2020.

[97] S. Palkhivala, "Active cavity stabilisation for nanosensing in a microfluidic environment", Master's Thesis, Karlsruhe Institute of Technology, Feb. 2021.

[98] L. Neuhaus *et al.*, "PyRPL (Python Red Pitaya Lockbox) — An open-source software package for FPGA-controlled quantum optics experiments", in *2017 Conference on Lasers and Electro-Optics Europe & European Quantum Electronics Conference (CLEO/Europe-EQEC)*, IEEE, Jun. 2017, pp. 1–1, ISBN: 978-1-5090-6736-7. DOI: 10.1109/CLEOE-EQEC.2017.8087380.

[99] J. F. S. Brachmann, H. Kaupp, T. W. Hänsch, and D. Hunger, "Photothermal effects in ultra-precisely stabilized tunable microcavities", *Optics Express*, vol. 24, no. 18, p. 21 205, Sep. 2016. DOI: 10.1364/oe.24.021205.

[100] Nanopartz Inc., *Spherical gold nanoparticles products and applications*, https://www.nanopartz.com/spherical_gold_nanoparticles.asp, 2024.

[101] S. Gómez-Graña *et al.*, "Surfactant (bi)layers on gold nanorods", *Langmuir*, vol. 28, no. 2, pp. 1453–1459, 2012. DOI: 10.1021/la203451p.

[102] nanoComposix, *Gold FAQ*, https://nanocomposix.com/pages/gold-frequently-asked-questions-faq, 2025.

[103] A. K. Wright and M. R. Thompson, "Hydrodynamic structure of bovine serum albumin determined by transient electric birefringence", *Biophysical Journal*, vol. 15, no. 2, pp. 137–141, Feb. 1975. DOI: 10.1016/s0006-3495(75)85797-3.

[104] Sigma Aldrich, *Albumin aus Rinderserum*, https://www.sigmaaldrich.com/DE/de/product/sigma/a8806, 2025.

[105] H. Kööp, "Fluctuation-autocorrelation analysis of nanoparticles in microcavities in real time", Bachelor's Thesis, Karlsruhe Institute of Technology, Apr. 2025.

[106] P. Müller, *Python multiple-tau algorithm*, https://pypi.python.org/pypi/multipletau/, 2012.

[107] Malvern Instruments, *ZetaSizer Nano ZS*, Brochure.

[108] nanoComposix, *Citrate surface*, https://nanocomposix.com/pages/citrate-surface, 2025.

[109] M. Mazaheri, J. Ehrig, A. Shkarin, V. Zaburdaev, and V. Sandoghdar, "Ultrahigh-speed imaging of rotational diffusion on a lipid bilayer", *Nano Letters*, vol. 20, no. 10, pp. 7213–7219, 2020. DOI: 10.1021/acs.nanolett.0c02516.

[110] B. Zhang, T. Lan, X. Huang, C. Dong, and J. Ren, "Sensitive single particle method for characterizing rapid rotational and translational diffusion and aspect ratio of anisotropic nanoparticles and its application in immunoassays", *Analytical Chemistry*, vol. 85, no. 20, pp. 9433–9438, 2013. DOI: 10.1021/ac4023956.

[111] K. C. Toussaint *et al.*, "Plasmon resonance-based optical trapping of single and multiple Au nanoparticles", *Optics Express*, vol. 15, no. 19, p. 12 017, Sep. 2007. DOI: 10.1364/oe.15.012017.

[112] K. Svoboda and S. M. Block, "Optical trapping of metallic Rayleigh particles", *Optics Letters*, vol. 19, no. 13, p. 930, Jul. 1994. DOI: 10.1364/ol.19.000930.

[113] K. C. Neuman and S. M. Block, "Optical trapping", *Review of Scientific Instruments*, vol. 75, no. 9, pp. 2787–2809, Sep. 2004. DOI: 10.1063/1.1785844.

[114] M. Pelton, M. Liu, H. Y. Kim, G. Smith, P. Guyot-Sionnest, and N. F. Scherer, "Optical trapping and alignment of single gold nanorods by using plasmon resonances", *Optics Letters*, vol. 31, no. 13, p. 2075, Jul. 2006. DOI: 10.1364/ol.31.002075.

[115] J. D. Watson and F. H. C. Crick, "Molecular structure of nucleic acids: A structure for deoxyribose nucleic acid", *Nature*, vol. 171, no. 4356, pp. 737–738, Apr. 1953. DOI: 10.1038/171737a0.

[116] S. Dey *et al.*, "DNA origami", *Nature Reviews Methods Primers*, vol. 1, no. 1, Jan. 2021. DOI: 10.1038/s43586-020-00009-8.

[117] D. Russell, *Flexural bending modes in a thin rectangular bar*, https://www.acs.psu.edu/drussell/Demos/Flexural-Bar/flexural.html, 2025.

[118] M. A. Śmiałek, N. C. Jones, S. V. Hoffmann, and N. J. Mason, "Measuring the density of DNA films using ultraviolet-visible interferometry", *Physical Review E*, vol. 87, no. 6, Jun. 2013. DOI: 10.1103/physreve.87.060701.

[119] K. S. Bloom, "Beyond the code: The mechanical properties of DNA as they relate to mitosis", *Chromosoma*, vol. 117, no. 2, pp. 103–110, Dec. 2007. DOI: 10.1007/s00412-007-0138-0.

[120] I. Axelsson, "Characterization of proteins and other macromolecules by agarose gel chromatography", *Journal of Chromatography A*, vol. 152, no. 1, pp. 21–32, 1978. DOI: 10.1016/S0021-9673(00)85330-3.

[121] I. M. Vlasova, A. A. Kuleshova, A. A. Vlasov, and A. M. Saletskii, "Polarized fluorescence in investigation of rotational diffusion of the fluorescein family markers in bovine serum albumin solutions", *Moscow University Physics Bulletin*, vol. 69, no. 5, pp. 401–405, Sep. 2014. DOI: 10.3103/s0027134914050099.

[122] N. Meechai, A. M. Jamieson, and J. Blackwell, "Translational diffusion coefficients of bovine serum albumin in aqueous solution at high ionic strength", *Journal of Colloid and Interface Science*, vol. 218, no. 1, pp. 167–175, Oct. 1999. DOI: 10.1006/jcis.1999.6401.

[123] A. K. Gaigalas, J. B. Hubbard, M. McCurley, and S. Woo, "Diffusion of bovine serum albumin in aqueous solutions", *The Journal of Physical Chemistry*, vol. 96, no. 5, pp. 2355–2359, Mar. 1992. DOI: 10.1021/j100184a063.

[124] Nanopartz Inc., *Nanopartz gold nanorods*, https://www.nanopartz.com/bare_gold_nanorods.asp, 2025.

[125] P. Stevic, *Piranha cleaning standard operating procedure*, Kavli Nanolab, Delft, 2018.

[126] M. Gerdan, "Optofluidic microlaser based on molecular complexes with the prospective of biochemical process examination", Master's Thesis, Karlsruhe Institute of Technology, Jun. 2024.

[127] L. Steib, "Optofluidic lasing based on europium complexes", Bachelor's Thesis, Karlsruhe Institute of Technology, Mar. 2025.

[128] L. J. Daumann, P. Werther, M. J. Ziegler, and K. N. Raymond, "Siderophore inspired tetra- and octadentate antenna ligands for luminescent Eu(III) and Tb(III) complexes", *Journal of Inorganic Biochemistry*, vol. 162, pp. 263–273, 2016. DOI: https://doi.org/10.1016/j.jinorgbio.2016.01.006.

Acknowledgements

No man is an island entire of itself;
every man is a piece of the continent, a part of the main…

— John Donne

Diese Dissertation ist ein Projekt, das ich alleine als „Insel“ nicht hätte fertigstellen können, und ich möchte mich nun bei den Menschen bedanken, die mich als „Festland“ auf meinem Weg während und auch vor der Promotion begleitet haben und mich dabei auf verschiedene Arten und Weisen unterstützt haben.

Mein erster und besonderer Dank gebührt natürlich David, der diese Promotion ermöglicht und betreut hat. Als mich mein Studium 2018 nach Karlsruhe geführt hat, begegnete ich ihm zum ersten Mal an einem (für einen frisch eingeflogenen Inder) kalten und dunklen Spätherbstmorgen bei meiner allerersten Vorlesung am KIT. Zwei Jahre später durfte ich meine Masterarbeit in seiner Arbeitsgruppe schreiben, was meine Begeisterung für dieses Thema geweckt hat, das ich dann während meiner Promotion erforschen würde.
Herzlichen Dank, David, sowohl für die perfekte Promotionsbetreuung, als auch für deine Begeisterung, für deine Ruhe und Geduld und für deine freundliche Art, worüber ich mich von den frühen Vorlesungen meines ersten Wintersemesters an bis jetzt freuen konnte und kann. Danke für dein Vertrauen und die Freiheit, meine Forschung selber zu gestalten und auch Nebenwege auszuprobieren, sowie für Ideen und Hinweise, die mich bei Stellen, an den ich manchmal hängenblieb, sanft und unauffällig vorwärts gestoßen haben. Und danke für die Aufmunterung und deinen stetigen Optimismus, die mich immer weiter motiviert haben und mich auf meine eigenen Ergebnisse stolz gemacht haben.
Dass mir die letzten fünf Jahre, die ich in deiner Arbeitsgruppe verbringen durfte, so viel Freude bereitet haben, hat auch viel mit der super angenehmen und respektvollen Arbeitsatmosphäre zu tun, die du in der Gruppe geschaffen hast. Deinen freundlichen, ehrlichen und positiven Umgang mit deinen Mitarbeitern und Studenten schätze ich sehr, und ich fand es immer schön, dass ich meine Kollegen niemals als Konkurrenten, sondern als enge Freunden und zweite Familie gesehen habe.

Diese zweite Familie – unsere fantastische Arbeitsgruppe – hat dafür gesorgt, dass ich mich jeden Morgen gefreut habe, ins Büro zu kommen, und ich möchte euch einen großen Dank aussprechen...

Larissa, für meine allererste Einführung in die spannende Welt der optofluidischen Sensorik und für alles, was du mir während meiner Masterarbeit und danach beigebracht hast, das mir auch während meiner Promotion gedient hat und noch länger dienen wird,

Jonas, mein langjähriger und langmütiger Büronachbar, für deine Hilfsbereitschaft und dein offenes Ohr, für die Ideen und die vielen spannenden Diskussionen, unter anderem über Fragen der elementaren Physik, die doch nicht so elementar waren wie gedacht,

Jannis, für deine vernünftige und gut gelaunte Weisheit, die unsere Bürodiskussionen über nicht-so-elementare Physik sowie ganz andere Themen bereichert hat,

Vishnu, my neighbour in more ways than one, for patiently putting up with me and tolerating my humour, and still being there to talk to about everything from food to physics, and for being a fantastic friend,

Timon, für deine Aufgeschlossenheit, dein Interesse an unterschiedlichen Perspektiven und Sichtweisen, und dass du dafür gesorgt hat, dass man sich in der Gruppe wohl und zu Hause gefühlt hat, auch wenn das tatsächliche Zuhause mehrere Tausend Kilometer entfernt liegen mag,

Evgenij, für unsere schönen gemeinsamen Mittagspausen und spannende gemeinsame Erfahrungen, auch über nächtliche Brachsenabholungen hinaus,

Nick, not only for the several thousand pots of tea we brewed and shared over the last few years, but also for your joviality, helpfulness and humour – muchas arigato!,

Kerim, für deine Herzlichkeit und (auch durch Bürowände) ansteckende Fröhlichkeit,

Jeremias, für deine Kollegialität, Hilfsbereitschaft und viele nette Gespräche mit dir, seien sie über die Kunst der Physik oder die Wissenschaft der Gastronomie,

Andras, für deine scheinbar mühelos rausgehauenen Sprüche, dank derer die humorvolle Stimmung in unserem Büro nie ausging,

Svenja, für deine sympathische Art und ausnahmelos gute Laune, die mir immer ein Lächeln ins Gesicht gebracht hat,

und jedem einzelnen weiteren Gruppenmitglied, für die netten Zeiten, die wir zusammen innerhalb und außerhalb des Instituts verbringen durften.

Wer nun glaubt, es ging in der Promotion meist um Teetrinken und Fische verteilen, den muss ich enttäuschen: es gehörte auch einiges an Laborarbeit dazu, und die Ergebnisse der letzten Kapitel dieses Texts stammen aus einem Labor in dem ich, dank einiger Menschen hier im Institut, die uns von hinter den Kulissen stark unterstützt haben, vor allem Spaß an der Physik haben konnte. Ich danke euch, Steffi und Claudia, dass ihr uns bei allen organisatorischen Sachen mit Rat und Tat zur Seite steht, seien es die Einkäufe, die unsere Experimente am Laufen halten, oder die Dienstreisen, die die Resultate aus dem Labor in die Welt hinaus tragen. Ich danke Herrn Meyer und seinem Team in der Mechanikwerkstatt für ihre Expertise, Geduld und Freundlichkeit auch bei unzähligen Aufträgen von Faserhaltern und anderen exotischen Teilen. Und ich danke Frau Hugle für ihre Unterstützung bei allen chemikalischen Dingen.
Ich möchte außerdem Christian Ritschel danken, nicht nur, weil ich euer DLS-Gerät mitbenutzen durfte, sondern für deine kontinuierliche Hilfsbereitschaft, wenn ich immer mal wieder ein paar neue Messungen machen und neue Proben oder Messbedingungen ausprobieren wollte.

Auch außerhalb des Labors und des Arbeitstages haben mich die Phänomene von Schwingungen und Wellen begleitet: da rede ich nun über mein Orchesterleben. Ich bin sehr dankbar für die vielen lieben Menschen, die ich auf musikalische Weise kennenlernen durfte, und mittlerweile zu meinen engsten Freunden zählen und die mein Leben bereichert und schön abgerundet haben. Ich schätze euch sehr, sowohl musikalisch als auch menschlich, und danke euch sehr für die gemeinsam verbrachte und erlebte Zeit, für die gemeinsamen Pizza-Abende, für die gemeinsamen Reisen, nah und fern, für eure stetige Unterstützung und Ermutigung und euer Interesse daran, was ich so außerhalb des Orchesters mache, obwohl die Stehwellen im Optiklabor ziemlich anders aussehen als die in unseren Instrumenten... und meine Nanostäbchen eher wie winzige Baguettes.

An important group of people whom I want to acknowledge for bringing me to the point where I could – and wanted to – write this doctoral thesis comprises my teachers, mentors and

professors, right from school through to my Bachelors and Masters degrees: you laid the basics, and the motivation, for what I achieved in this work.
And having written my doctoral thesis in an *optics* lab, I owe special thanks to Prof. Prabhu and his team for my very first introduction to experimental optics. I think I've come a long way from the undergraduate student with no experience I was when I started working with you, but so much of what I know and use today stems from my experiences at TIFR. Thank you for taking me into your group, for giving me my first research experience in the FOTON lab, and the support to work on state-of-the art optics first-hand.

I want to also give a special shout out to my friends whom I have had the pleasure to get to know over the last several years – for your support and encouragement, and for still putting up with me, even for over a decade!

We're now reaching the end, but I'd like to go back to the very beginning to where my journey started, because I have my family to thank for my being where I am today. Right from planting the curiosity about How Things Work and giving me plenty of Things to Make and Do, you raised an experimental physicist! *This* book would not exist without your support for me in every way, in all the things I'd do and The Places I'd Go.

Genau, als "Insel" hätte ich diese Arbeit nicht in ihrer jetzigen Form bringen können, und die Zeit die ich dabei verbracht habe hätte mir nicht so viel Spaß gemacht. Mein "Festland" besteht aus vielen Menschen von und auf mehreren Kontinenten, und ich sage euch allen: danke schön, thank you, धन्यवाद.

Fine